Improvements for Near-field Scanners Consisting of Planar Array of H-Field Probes

by

Ali Kiaee

A thesis submitted in partial fulfillment of the requirements for the degree of

Doctor of Philosophy

In

Electromagnetics & Microwaves

Department of Electrical and Computer Engineering
University of Alberta

Abstract

Modern wireless applications require flexible and adaptable multi-purpose wireless devices. These devices need to sense environmental conditions, adapt to user requirements, and decide how to communicate among themselves in a self-organized manner. Achieving such versatility and performance along with fast prototyping is extremely difficult, if not impossible utilizing current state-of-the-art measurement techniques. Designing state-of-the-art digital, RF (Radio Frequency) and antenna subsystems that use fast-prototyping with fast measurements is a significant challenge and a potential bottleneck of every modern-day industrial design process.

Probe-array based measurement devices have been shown to be novel measurement EMC (Electromagnetic Compatibility)/RF tools [1] which have significantly facilitated the near-field measurement and diagnosis of antennas and PCBs. Probe arrays make it possible to perform certain vital EMC/EMI tests, and antenna measurements, which can be performed inside the lab-environment, in real-time. Real-time methods introduce a huge added-value for industry to diagnose EMC/EMI problems associated with high-speed digital PCBs, which are time varying and can be difficult during long measurement times.

Despite all the features array-based measurement tools have to offer, they are new and require a considerable level of further research. In this thesis, it is aimed to help EMSCAN, a corporation that manufactures array-based scanners, enhance the quality and accuracy of their measurement systems, as well as enabling them to reach new markets by developing innovative applications.

From the technical point of view, the scanner problem's setup can be described as follows: There is a planar array of 1600 probes backed by a finite dielectric slab and a copper ground plane. The inputs of the problem are the probe voltages measuring magnetic very near-field of a device under test (i.e. PCB, antenna …). The general desirable outcomes for this thesis are 1) the far-field patterns of the device under test (DUT) for antenna applications and 2) the field reconstruction close to the ones radiated by the DUT for diagnosis, and EMC/EMI applications.

This thesis contains 3 main chapters. Chapter 2 deals with ground plane de-embedding in which a novel algorithm is proposed to correct for distortions introduced by the ground plane of

the scanner using 4 source reconstruction models (SRM). Chapter 3 assesses existing source reconstruction models that can be used for 6-sided measurements (stitching 6 individual FFs) in terms of their ability to be used for a magnetic scanner. It also proposes a novel algorithm to correct for the dominant source error introduced by this type of measurement system. Chapter 4 shows that dyadic Green's functions are accurate tools for analyzing planar absorber stacks. It also proposes a Novel technique for post absorber field estimation for EMC/EMI applications.

The novel algorithms developed through this thesis are: 1) Ground de-embedding algorithm described in the chapter 2, correction algorithm described in chapter 3 and field estimation algorithm described in chapter 4.

Also, this thesis showed that 1) Green's functions are accurate tools for analyzing planar stack of absorbers (Chapter 4) and 2) previous SRM studies does not necessarily hold for magnetic probe-array based measurements (Chapter 3).

Preface

This is an original work by Ali Kiaee. A short version of chapter 2 was published as Ali Kiaee; Rezvan Rafiee Alavi; Mohammad Mahdi Honari; Rashid Mirzavand; Pedram Mousavi, " Ground de-embedded source reconstruction using a planar array of H-field probes" at 2017 IEEE International Symposium on Antennas and Propagation & USNC/URSI National Radio Science Meeting and the long version was published as A. Kiaee, R. R. Alavi, R. Mirzavand, and P. Mousavi, "Numerical and experimental assessment of source reconstruction for very Near Field measurements with an array of H-field probes," IEEE Trans. Antennas Propag., pp. 1–1, 2017. Chapter 3 has been submitted to IEEE Transactions on antennas and propagation as Ali Kiaee, Ruska Patton, Rezvan Rafiee Alavi, Babak Alavikia, Rashid Mirzavand, Pedram Mousavi, "First Order Correction and Equivalent Source Reconstruction Assessment for Practical Multi-plane Magnetic Near-Field Measurements". Chapter 4 submitted to IEEE Transactions on Electromagnetic Compatibility as Ali Kiaee, Ruska Patton, Rezvan Rafiee Alavi, Babak Alavikia, Rashid Mirzavand, Pedram Mousavi, "Planar Green's Function based MoM Used in Absorber Effect Estimation for EMC/EMI Applications"

Dedication

This thesis is dedicated to my mother, Maryam, my father Saeed, my siblings Parisa and Majid who have always cared and sacrificed for my success and happiness. This work is also dedicated to Niloofar, my partner, who has always been inspiring me with her love and enthusiasm. I appreciate the support from my loved ones who have always been there for me.

Acknowledgments

I would like to thank my supervisor Dr. Pedram Mousavi for his great help and encouragement through the course of my Ph.D. I am also sincerely grateful to Mr. Ruska Patton, EMSCAN R&D manager, and Dr. Rashid Mirzavand, university of Alberta research associate, for their excellent support.

Contents

List of Figures

List of Symbols

E	Electric Field Intensity
H	Magnetic Field Intensity
J	Surface Electric current density
M	Surface Magnetic current density
MOM	Method of Moments
PWS	Plane wave spectrum
SRM	Source Reconstruction Model
L{}	Electromagnetic Operator L
K{}	Electromagnetic Operator K
g	Free space Green's function
$\bar{\bar{G}}$	Dyadic Green's function
k	Wave vector
AUT	Antenna Under Test
DUT	Device Under Test
r	Observation Vector
r'	Source Vector
θ	Far-field elevation angle
ϕ	Far-field azimuth angle
δ	Observation error
RWG	Basis function first proposed by Rao-Wilton-Glisson
PCB	Printed Circuit Board
SVD	Singular Value Decomposition
A	Electric current potential
F	Magnetic current potential

Chapter 1

Introduction

1.1. Introduction to Near-field to Far-field Transformation

There are generally two classes of near-field to far-field transformation methods. The first class tries to calculate the far-field data by applying operators to measured fields directly using modal expansions. The second class on the other hand tries to back project the measured fields to a fictitious surface, a surface containing sources representing antennae, and then calculates far-fields based on the reconstructed sources. The main reason for back projection is that only magnetic field (H) is known according to the equivalence theorem and PMC boundary condition needs to be assumed on the measurement surface [2].

The earliest works around the near-field to far-field transformation, and even field reconstruction, were based on the modal expansion methods known as the popular plane wave spectrum (PWS). In the modal expansion method, the fields radiated by the antenna under test (AUT) are expanded in terms of planar, cylindrical, or spherical wave functions. For the planar case the expansion is shown in Fig. 1.1 [3].

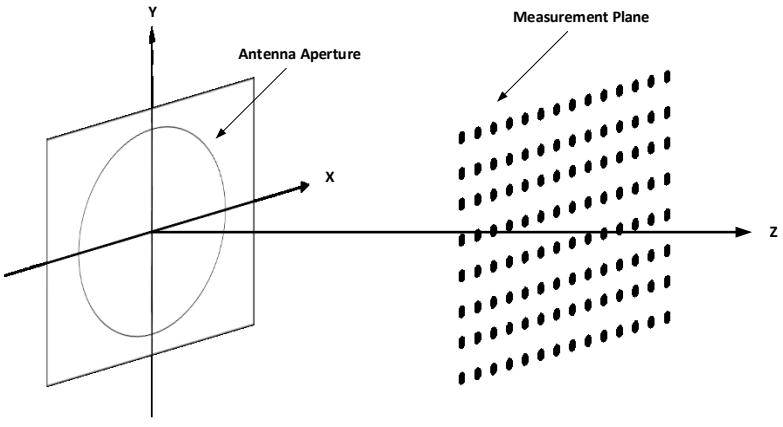

Fig. 1.1 Planar Near-field measurement setup

$$\boldsymbol{E}(\boldsymbol{r}) = \frac{1}{2\pi}\iint \boldsymbol{A}(k_x, k_y)e^{-j.\boldsymbol{k}.\boldsymbol{r}}dk_x dk_y \quad (1)$$

$$\boldsymbol{H}(r) = \frac{1}{2\pi}\iint \boldsymbol{k} \times \boldsymbol{A}(k_x, k_y)e^{-j.\boldsymbol{k}.\boldsymbol{r}}dk_x dk_y \quad (2)$$

$$\boldsymbol{k}.\boldsymbol{A} = 0 \quad (3)$$

Measured near fields on the measurement plane are used to calculate the unknown coefficients of this expansion(1,2). These modes are used to extract far-field data of the radiator [3]–[6]. In the case of sinusoidal orthogonal modes, the expansion coefficients can be easily obtained by applying classical Fourier transform to the measured fields [3]:

$$A_x(k_x, k_y) = \frac{1}{2\pi}\iint E_x(x, y, 0)e^{j.\boldsymbol{k}.\boldsymbol{r}}dxdy \quad (4)$$

$$A_y(k_x, k_y) = \frac{1}{2\pi}\iint E_y(x, y, 0)e^{j.\boldsymbol{k}.\boldsymbol{r}}dxdy \quad (5)$$

Two interesting factors to study are sampling distance and distortions due to evanescent fields. According to Nyquist theorem, the sampling distance for measurements on a planar surface should be less than half a wavelength [3]. Studies show that even a slight decrease from this rate may cause significant noise. A simple test which can show reconstruction accuracy is to compare interpolated fields and simulated fields in certain distances away from the measurement aperture.

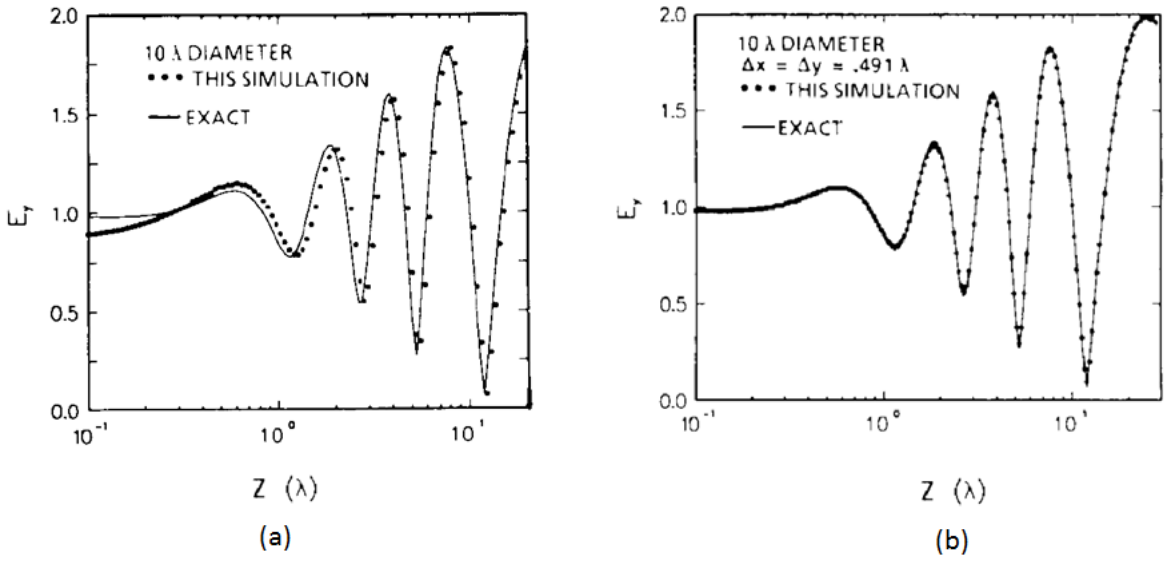

Fig. 1.2 Ey component at different distances away from measurement plane for uniformly distributed aperture of 10 λ with sampling distances of (a) half wavelength and (b) 0.491 λ [3]

Fig. 1.2 shows the comparison of simulated (original) fields versus reconstructed fields using PWS for a uniform circular array Ey=1 (uniform source), measured using 64x64 array. For meaningful comparison, the evanescent wave part of the fields has been filtered out with a filter FILTV [3] before calculating the results, as the fields only consist of traveling waves. It shows the sampling distance of less than half a wavelength is sufficient and can model propagating fields accurately. The discrepancy between the Fig. 1.2 (a) and (b) (results being sensitive to sampling distance) is significant due to current discontinuity on the aperture edge, which causes high spatial frequency components. If the abrupt change on the edge is replaced with a tapered edge, the difference starts to decrease to zero. To see this effect more clearly, Fig. 1.3. plots the Ey along the x axis in which x is between 0 and 10 λ away from antenna aperture for a tapered distributed antenna fields. As it is shown, the discrepancy in Fig. 1.2 cannot be observed because the current distribution on the aperture is parabolic and goes to zero on the edges.

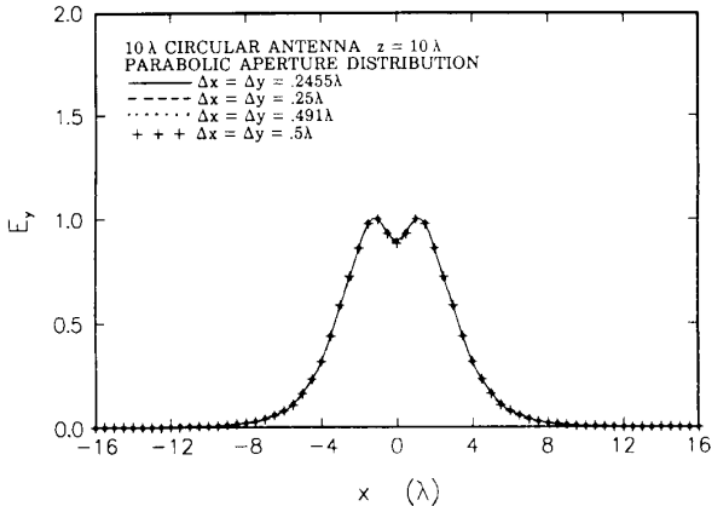

Fig. 1.3. Simulated Ey versus x when sampled at different spacings [3]

The other factor to study is distortions due to evanescent fields. Looking at (1) and (2), it is obvious we have inherently assumed that the fields on the measurement plane is only composed of propagating waves, in case of non-evanescent modes. The question to ask here is, what if that is not the case? Authors in [3] believe evanescent fields usually are of small magnitudes and they cannot contribute to near-field measurement, particularly if the measurement window is more than one lambda away from radiator. This assumption cannot be held in this thesis, because we will be dealing with very near-field measurements in which evanescent fields can play a major role.

For better comprehension, the uniform aperture experiment (uniformly distributed aperture of 10 λ) has been repeated including evanescent fields. As illustrated in Fig. 1.4, a certain discrepancy starts to emerge as we try to reconstruct fields under one wavelength away from the antenna aperture. Now a second case can be studied by replacing the uniform aperture with a tapered one. Essentially, if the aperture has hard boundaries, the high spatially frequency components contribute to discrepancies requiring more sampling. This is alleviated when looking at tapered apertures. We will be able to reconstruct near-fields of the antenna (Fig. 1.5).

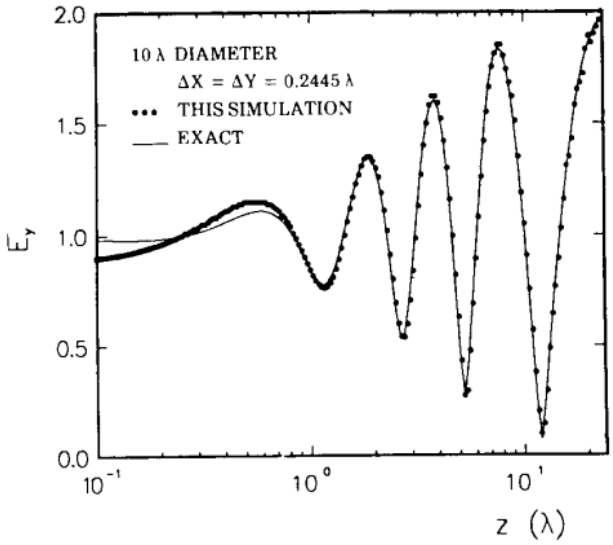

Fig. 1.4. Comparison of the exact and the simulated fields for a uniform aperture. [3]

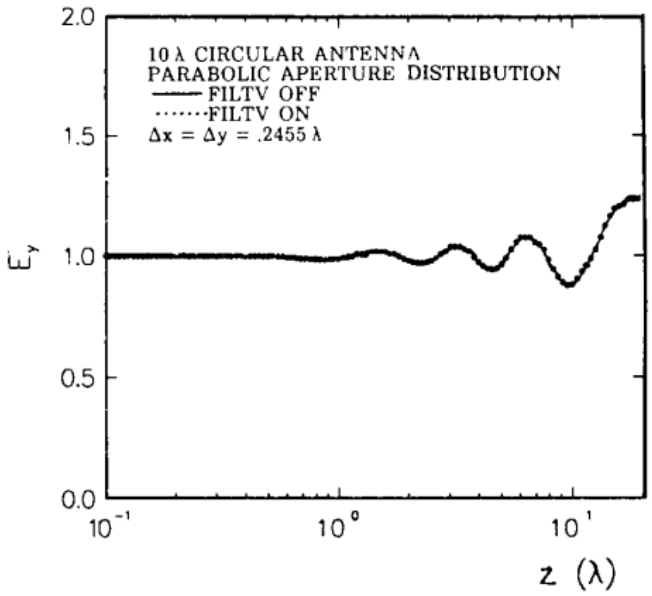

Fig. 1.5. Comparison of the exact and the simulated field uniform for tapered aperture. [3]

Despite the inability to model evanescent fields, especially in very near field measurements, the PWS method is of significant importance for being relatively fast. The modal expansion based methods can even benefit from hardware accelerated FFT calculators. This fact

makes modal expansions a good choice for EMC/EMI diagnosis, where a real-time response is essential. Regarding the EMC/EMI application, we would be interested in reconstruction of the fields both close to the radiator ($< 1\lambda$) and 3m away from it. There are a few drawbacks to this method: firstly, transformation accuracy degrades if there are evanescent fields of significant energy present on the measurement plane. This contradicts the basic underlying assumption of measurement fields consisting of propagating modes. Secondly, since the fields outside the measurement region are assumed to be zero, far-field solid angle accuracy range degrades due to the truncation effect on the edges. Finally, these truncation results introduce spurious side lobes in the far-field. The effect of these side-lobes can be alleviated by using spatial low-pass filters [5] which gradually force the fields to vanish as we move toward the measurement plane edges. According to [5] the filter should have three features:

1) The filter should have a sharp cut-off above which the attenuation should be significantly high in order of more than 40dB.
2) The impulse response of the filter should be separable in following sense $\mathrm{h}(\mathrm{x},\mathrm{y}) = \mathrm{h}(\mathrm{x}).\mathrm{h}(\mathrm{y})$
3) The impulse response of the filter should be spatially limited. As a result, the response should be identically zero for the range that is not in the measurement window.

Authors in [5] chose Blackman filter since it meets the requirements above. The process of filtering can be summarized in the following flow chart (Fig. 1.6).

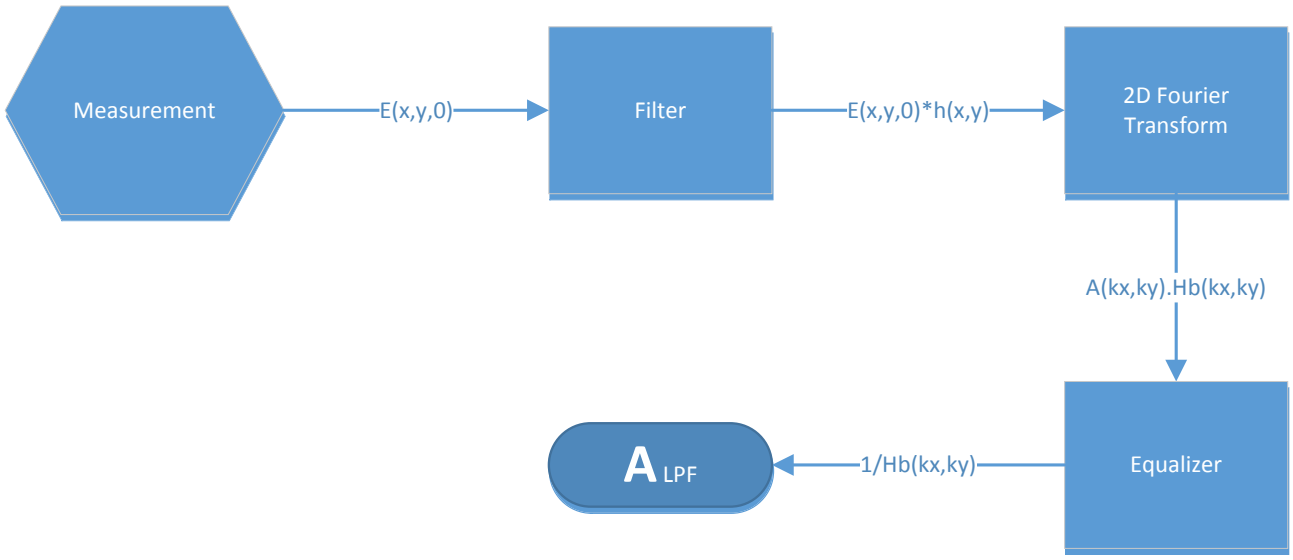

Fig. 1.6. Near-field Filtering flowchart (re-drawn based on [5])

In this process the response measured by the probes is convolved with the spatial impulse response of the filter and then passed to Fourier transform block. This way we ensure high spatial frequency components are filtered out. Afterwards, we can divide the response by the spatial response of the filter to remove the effect of the filter. We need to be cautious not to filter out the antenna response. In the case of large electrical structures there might be high frequency components present in the response which might be unintentionally filtered out. The electrical size of the radiator can give us an estimation of how sharp (containing high order spatial modes) the far-field (FF) response can be. It is important to consider the frequency response of the low pass filter when dividing the response of the Fourier transform to that of the filter. We might face some unwanted effects caused by the machine precision limitations. A simple solution to the problem is considering the response to be of zero magnitude after the cut-off wavenumber of the filter being used.

In the second class of methods, measurement fields are first back-projected to a fictitious source surface and then transformed to far-field data. In [2], a planar array of infinitesimal magnetic dipoles is used as a fictitious layer which is assumed to be laid on an infinite perfectly

electric conductor (PEC) plane. Then, antenna far-fields are calculated through array far-field rules based on the complex dipoles amplitudes. [7]

$$\boldsymbol{E}(\boldsymbol{r}) = -\iint [\boldsymbol{M}(\boldsymbol{r}') \times \nabla g(\boldsymbol{r}, \boldsymbol{r}')] ds' \tag{6}$$

$$g(\boldsymbol{r}, \boldsymbol{r}') = \frac{e^{-jk_0|\boldsymbol{r}-\boldsymbol{r}'|}}{4\pi\,|\boldsymbol{r}-\boldsymbol{r}'|} \tag{7}$$

For the planar case, by using equation (6), we can construct an integral equation relating magnetic currents on the fictitious layer to the measured fields. Later we can try to solve the equation and find the current on the fictitious layer, which radiates the same field as the measured ones. As it can be seen in Fig. 1.7, the space is divided into two sub-regions with the measurement plane being placed on the interface. We assume the measurement area is an aperture in an infinite PEC plane. According to equivalence theorem, fields on a closed surface can be replaced with proper electric and magnetic currents. Once replacing the fields with equivalent currents, we have tangential electric field zero all along the PEC infinite plane. Now, according to image theorem, all electric currents will be eliminated and only magnetic currents will remain. Again according to the equivalence theorem, we can replace tangential magnetic current on PEC infinite plane with two times of the same current in free space. By assuming PEC boundary on XY plane, it is assumed there is no tangential far-field component on that plane either, and hence this method will not be accurate. We know electric fields due to magnetic sources in free space are related as shown in (8). For a planar setup (Fig. 1.7), considering fictitious and measurement planes, the equations simplify to (9) [7].

$$\boldsymbol{E}(\boldsymbol{r}) = \int \quad \boldsymbol{M}(\boldsymbol{r}') \times \nabla g(\boldsymbol{r}, \boldsymbol{r}') ds \tag{8}$$

$$\begin{bmatrix} E_{measured\,x}(\boldsymbol{r}) \\ E_{measured\,y}(\boldsymbol{r}) \end{bmatrix} = -\iint \begin{bmatrix} 0 & \frac{\partial g(\boldsymbol{r},\boldsymbol{r}')}{\partial z'} \\ -\frac{\partial g(\boldsymbol{r},\boldsymbol{r}')}{\partial z'} & 0 \end{bmatrix} \begin{bmatrix} M_x(\boldsymbol{r}') \\ M_y(\boldsymbol{r}') \end{bmatrix} ds' \tag{9}$$

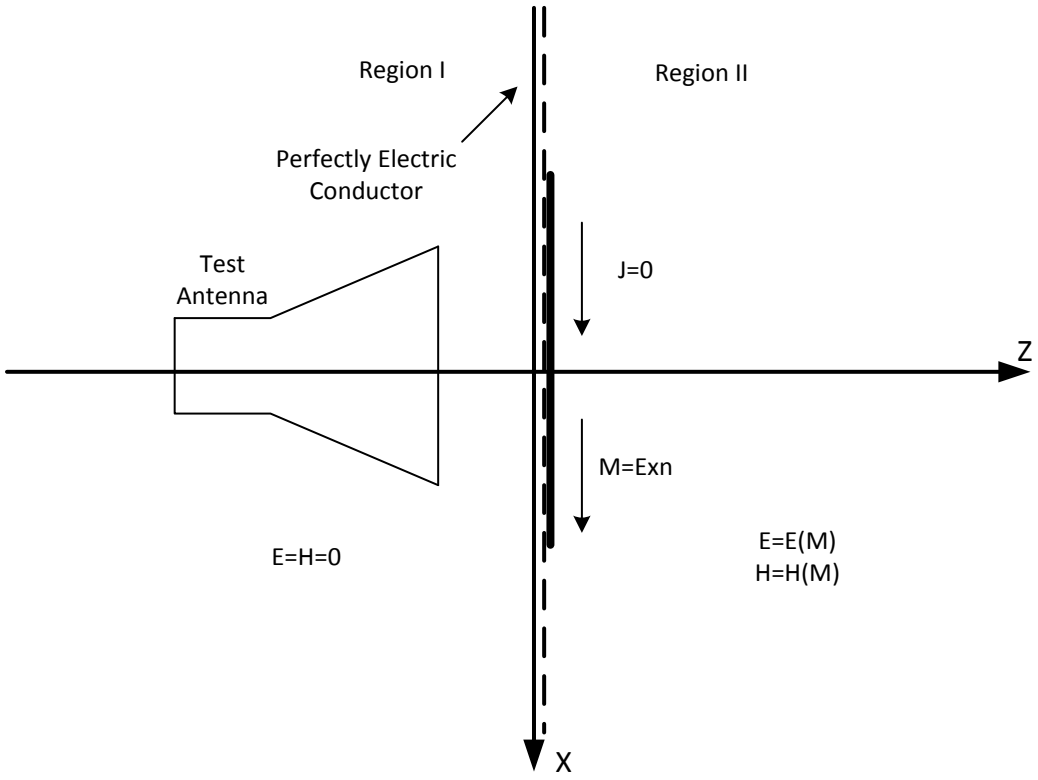

Fig. 1.7 Planar source reconstruction using magnetic currents [7]

It is shown that the system of equations (9) is completely decoupled, hence sometimes magnetic currents are preferred for source reconstruction. Fig. 1.8 shows results of the comparison of the algorithm being compared with PWS using an array of patch antennas. However, as illustrated, the presumption holds and there are no fields in $\theta = 90$ plane.

Source reconstruction of fields can also be accomplished using an equivalent closed surface embracing all the volume [8] which is different from the free space [9]. In comparison with the previous class of methods, especially those dealing with open measurement surfaces, there are no far-field distortions, since it does not suffer from the truncation effect. As a disadvantage, the process time is more than that of the modal expansion based techniques. Attempts have been made to enhance the accuracy of the reconstructed currents and far-field patterns, including the one proposed by Quijano et al [9] [10].

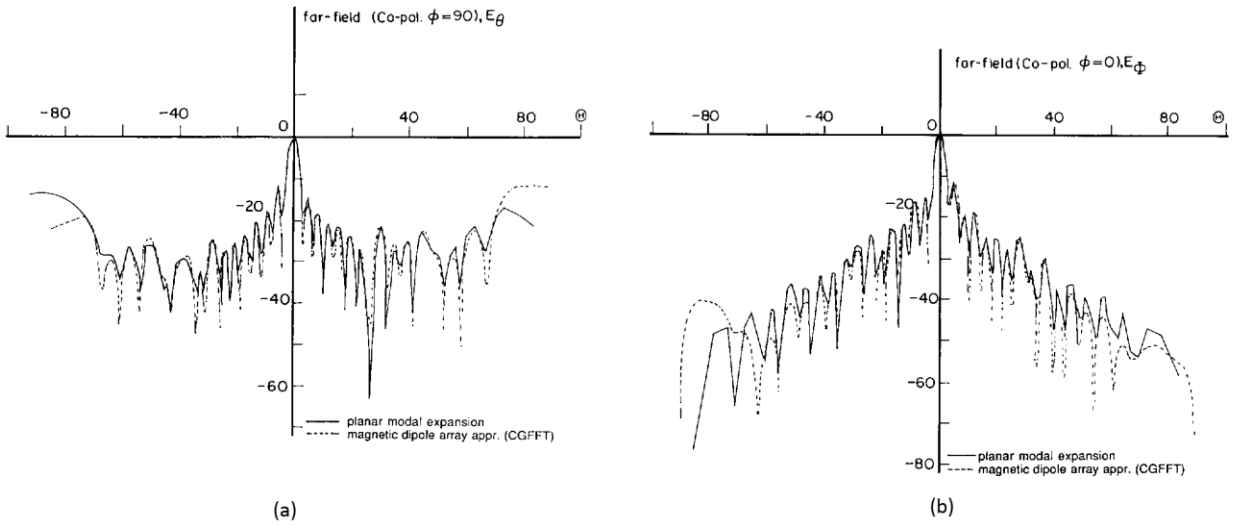

Fig. 1.8. Copolarization pattern of a 32x32 patch microstrip array using PWS and Equivalent magnetic dipoles for a) $\phi = 0$ and b) $\phi = 90$ cuts [7]

In the method [9], AUT is modeled by a closed arbitrary fictitious surface which contains all materials that differ from free space. Both electric and magnetic currents exist on this surface. The authors used Love's equivalence principle to enforce tangential E/H fields to vanish on an inner surface which is inside the fictitious one [9].

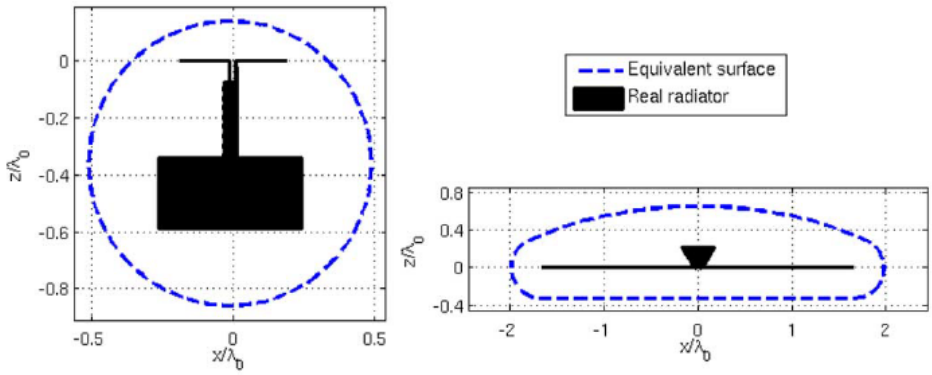

Fig. 1.9. Test structures: (left) strip dipole on a rectangular box, (right) monocone on a circular ground plane. Encompassed by closed fictitious surfaces [9]

Fig. 1.9 shows two typical examples of how an antenna can be encompassed in fictitious layers. It is interesting to compare current reconstructions for these typical antennas between single source methods and those using double sources simultaneously. As it can be seen in Fig. 1.10, using electric and magnetic currents at the same time significantly improves the reconstruction quality. It is verified by the fact that fields for dual equation are very close to the reference ones.

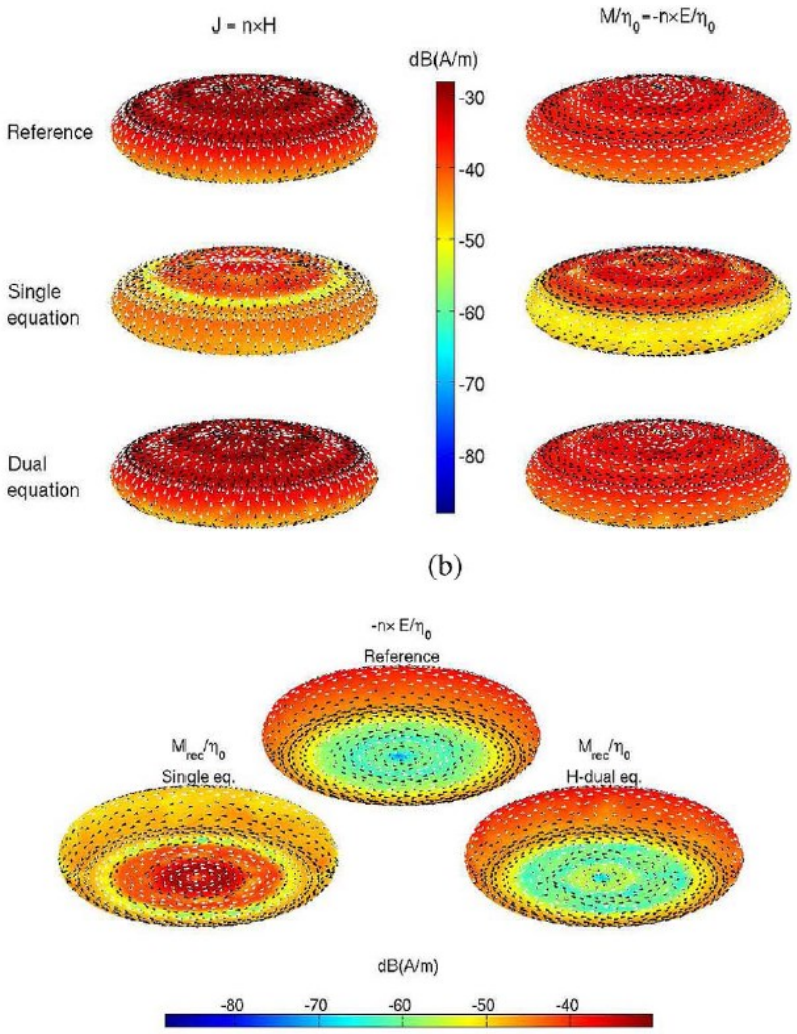

Fig. 1.10. Reconstructed currents for the test cases for top and bottom view of reconstructed currents for the mono-cone. [9]

Recent works are more inclined towards PCB applications for EMC/EMI purposes. Similarly, in [11] authors have used Genetics Algorithm (GA) optimization method to back project measured near-fields to currents on PCB tracks. Some other authors tried to find equivalent sources composed of electric and/or magnetic dipoles through the least square method or other iterative minimization techniques [11], [12].

Moreover, authors in [13] and [14] used piecewise sinusoidal basis functions to discretize electric and magnetic currents on rectangular grids. In the equation system the discretized currents' radiated voltage is used to form a system of linear equations. The system of equations was solved using the Tikhonov regularization technique to provide a stable solution. Later in [15] authors show how Tikhonov regularization technique can be used for the inverse problem and how this method can use prior information about the DUT. The same authors showed application of the proper regularization techniques in tomography [16], [17].

It is important to consider that all probes are actually antennas which have different radiation patterns. Therefore, probes receive near-fields according to their FF radiation pattern. In order to perform more accurate measurements, all the effects caused by the probes need to be de-embedded. In the case of single probe planar setup, probe correction can be relatively simple, provided that the PWS method is used. By the definition of the approach, measured fields are expanded in terms of far-field orthogonal functions. Fourier expansion of measured field can be shown to be the product of spectral expansions of AUT and probe being used [5].

$$A_{mx}(k_x, k_y) = \boldsymbol{A}(k_x, k_y).\boldsymbol{A}_p(k_x, k_y) \quad (10)$$

$$A_{my}(k_x, k_y) = \boldsymbol{A}(k_x, k_y).\boldsymbol{A}_{p'}(k_x, k_y) \quad (11)$$

Where $A_{mx,y}$ are the Fourier transform of the measured field, $\mathbf{A}$ is the Fourier expansion of the radiation pattern of the antenna under test and finally $\mathbf{A}_p$and $\mathbf{A}_{p'}$ are the Fourier expansion of the radiation pattern of the probe in two orientations (for measuring x and y component of the fields). Using (4) one can de-embed the probes radiation pattern and calculate measurement pattern of the AUT accurately [5].

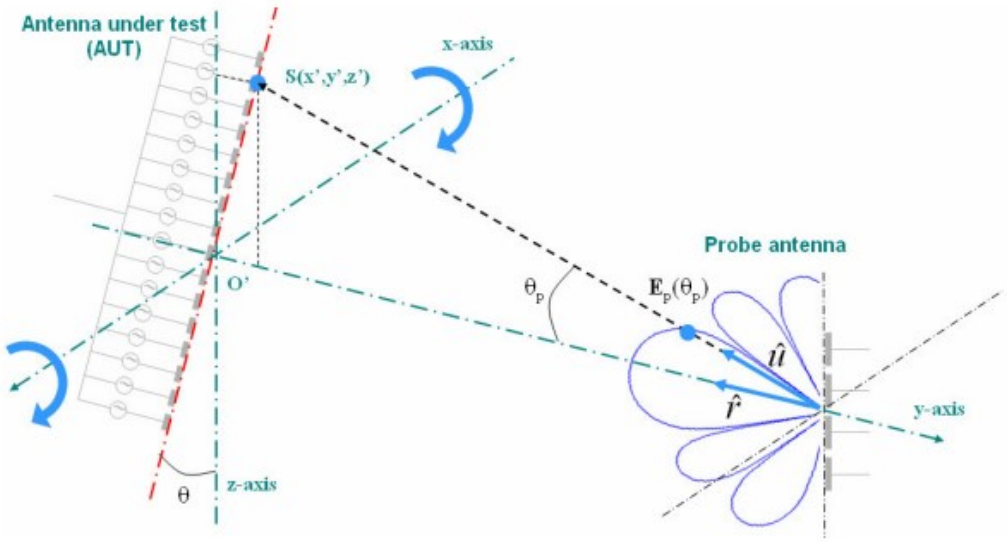

Fig. 1.11. A typical antenna measured by a directional probe [18]

Probe correction methods with MOM are somehow different from those being used in plane wave spectrum. In this case, probe correction needs to be brought into account when the method of moment's main interaction matrix is being built. Probe effects can be brought into account by multiplying the matrix elements ($Z_{i,j}$) by a correction factor. This factor should be dependent on the source-observation angle (between the ith source and jth measurement point) as well as the orientation of the currents on the basis function [18]. It is shown in Fig. 1.11 that radiation pattern of the probe can affect the final far-field results. The same conclusion does not hold for extreme near-fields as the antenna and the probe are no longer in one another far-field region.

Probe correction for the scenario in Fig. 1.11 can be divided into following steps:

- The effective angle at which sources see the probe should be calculated.
- The effective polarization that the probe experiences should be detected.
- Probe pattern at the associated angle and polarization should be used as a weight value for the Green's function.
- Probe's loading effects should also be considered.

The effective angle can be defined as the angle between the line which connects two sources and observation points versus the main beam of the probe. However, detecting the effective polarization is dependent on the basis function being used.

It is worth mentioning that the design and optimization of near-field probes have been subject of many studies for 4 primary goals: firstly, maximising probe factor (ratio of probe voltage over the field it senses),secondly, minimizing probe-field interference to achieve a non-intrusive scan, and finally increasing the bandwidth of the probe and maximising probe linearity [19]–[24].

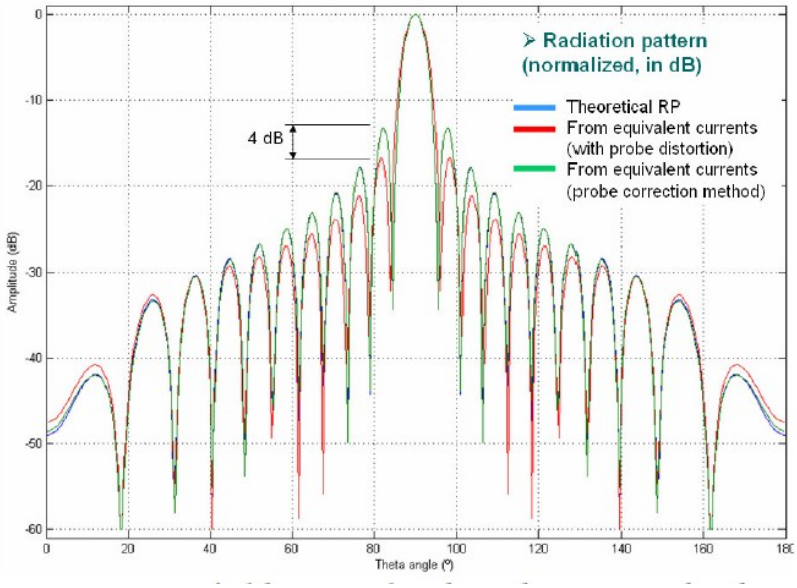

Fig. 1.12. A typical radiation pattern of an antenna with and without Probe correction [18]

1.2. Introduction to Electromagnetic Operators

Maxwell's equations in homogenous linear medium assuming $e^{j\omega t}$ time dependence can be stated as:

$$\nabla \times \boldsymbol{E} = -j\omega\mu\boldsymbol{H} - \boldsymbol{M} \tag{12}$$

$$\nabla \times \boldsymbol{H} = j\omega\epsilon\boldsymbol{E} + \boldsymbol{J} \tag{13}$$

$$\nabla . \boldsymbol{E} = \frac{1}{\epsilon}\rho_e \tag{14}$$

$$\nabla . \boldsymbol{H} = \frac{1}{\mu}\rho_m \tag{15}$$

Electromagnetic fields can be calculated based on vector potentials [25]

$$\boldsymbol{H} = \frac{1}{\mu}\boldsymbol{\nabla} \times \boldsymbol{A} \tag{16}$$

$$\boldsymbol{E} = \frac{1}{\epsilon}\boldsymbol{\nabla} \times \boldsymbol{F} \tag{17}$$

It can be further shown that the vector potentials follow Helmholtz's integral equation [26]

$$\nabla^2 \boldsymbol{A} + k^2 \boldsymbol{A} = -\mu \boldsymbol{J} \tag{18}$$

$$\nabla^2 \boldsymbol{F} + k^2 \boldsymbol{F} = -\epsilon \boldsymbol{M} \tag{19}$$

A and F can then be calculated using Helmholtz integral equation's Green's function:

$$\boldsymbol{A} = \mu \int \boldsymbol{J}(r') \frac{e^{-jk|r-r'|}}{4\pi|r-r'|} dr' \tag{20}$$

$$\boldsymbol{F} = \epsilon \int \boldsymbol{M}(r') \frac{e^{-jk|r-r'|}}{4\pi|r-r'|} dr' \tag{21}$$

In a source free region, using (20-21), (16-17) and curl's identity (22), it can be shown that:

$$\nabla \times (\alpha \boldsymbol{A}) = \alpha(\nabla \times \boldsymbol{A}) + (\nabla \alpha) \times \boldsymbol{A} \tag{22}$$

$$\boldsymbol{H_J} = -\int \boldsymbol{J}(r') \times \nabla g(r, r')\, dr' \tag{23}$$

$$\boldsymbol{E_M} = \int \boldsymbol{M}(r') \times \nabla g(r, r')\, dr' \tag{24}$$

The equations above can be stated using a linear operator considering the following part as an operator:

$$\boldsymbol{H_J} = -K\{\boldsymbol{J}\} \tag{25}$$

$$\boldsymbol{E_M} = K\{\boldsymbol{M}\} \tag{26}$$

$$\boldsymbol{K}\{\boldsymbol{X}\} = -\int \boldsymbol{X} \times \nabla g(r, r')\, dr' \tag{27}$$

Again, using Maxwell's equations, it can be shown

$$\boldsymbol{H_M} = \frac{1}{j\omega\mu\epsilon} \nabla \times \nabla \times \boldsymbol{F} \tag{28}$$

$$\boldsymbol{E_J} = \frac{1}{j\omega\mu\epsilon} \nabla \times \nabla \times \boldsymbol{A} \tag{29}$$

Using vector identities and the Helmholtz integral equation (18-19), it can be shown:

$$\boldsymbol{E_J} = -\eta_0 \times jk \int (\boldsymbol{J}(r') + \frac{1}{k^2} \nabla\nabla' . \mathbf{J}(\mathrm{r}')) \frac{e^{-jk|r-r'|}}{4\pi|r-r'|}\, dr' \tag{30}$$

$$\boldsymbol{H_M} = -\eta_0 \times jk \int (\boldsymbol{M}(r') + \frac{1}{k^2} \nabla\nabla' . \mathbf{M}(\mathrm{r}')) \frac{e^{-jk|r-r'|}}{4\pi|r-r'|}\, dr' \tag{31}$$

The equation above can be stated by linear operators:

$$\boldsymbol{E_J}(r) = -\eta\, L\{\boldsymbol{J}\}(r) \tag{32}$$

$$\boldsymbol{H_M}(r) = -\frac{1}{\eta}\, L\{\boldsymbol{M}\}(r) \tag{33}$$

$$L\{\boldsymbol{X}\} = jk \int \left(\bar{\bar{I}} + \frac{1}{k^2} \nabla\nabla' .\right) \boldsymbol{X} g(r, r')\, dr' \tag{34}$$

It can it be shown that the second term in (34) can also be expressed in following forms [26]:

$$\boldsymbol{I}(r) = \nabla\nabla\int \mathrm{g(r,r')}\mathbf{X}(\mathrm{r'})\mathrm{dr'} = \nabla\int g(r,r')\nabla'.\boldsymbol{X}(r')dr' = \int g(r,r')\nabla'\nabla'.\mathbf{X}(\mathrm{r'})\mathrm{dr'} \quad (35)$$

The above identity is very useful in MOM discretization. Using RWG basis functions, the second form in (35) is more convenient as $\nabla'.\boldsymbol{X_{RWG}}(r')$ is constant over a triangular subdomain.

In more a conceptual way, L and K operators transform J and M from current space to E and H field space. It is essential to remember L and K operators are both singular and very importantly compact. Since L and K are linear operators they can expanded in terms of their basis dimensions.

$$L\{\boldsymbol{X}\} = (\boldsymbol{U_1^*}.\boldsymbol{X})\sigma_1\boldsymbol{V_1} + (\boldsymbol{U_2^*}.\boldsymbol{X})\sigma_2\boldsymbol{V_2} + \cdots \quad (36)$$

Where U_i and V_i are vectors of unit norm that span source and destination space. In the case of L operators U_i and V_i are modes of current and field space. L and K are compact in the sense that σ_i goes to zero as i increases. Consequently, according to SNR of the problem, L and K operators can have finite dimensional estimations. From the physical perspective, as currents radiate in space, they become smooth and one cannot reconstruct current perfectly by information from the measured fields. In antenna theory we know that there is an upper limit for the gain of an antenna given a finite aperture, that is a consequence of compactness of electromagnetic operators.

Inverting a problem that relies on discretizing compact operators is called ill-posed. In this case the discretization should be followed by a regularization step [27]. In this work, SVD is used to estimate U and V modes and therefor directly regularizing the problem.

Chapter 2

Numerical and experimental assessment of source reconstruction for very Near Field measurements with an array of H-field probes

This chapter presents a novel formulation of the source reconstruction problem that aims at increasing the accuracy of near-field (NF) to far-field (FF) transformations in a particular measurement arrangement where the NF data are rapidly acquired by a planar array of H-field probes located close to a ground plane. A source reconstruction algorithm is proposed for obtaining the near electric and magnetic fields as well as the FF radiation pattern of the antenna under test (AUT) after filtering the effects of the currents induced on the ground plane backing the probe array. This algorithm exploits a system of integral equations that, after discretization according the Method of Moments (MOM), enables back-projecting the measured fields on equivalent sources distributed over an arbitrary three-dimensional (3-D) surface. Different integral equations are considered for that purpose. The accuracy provided by four different integral formulations is investigated from measured and synthetic experimental data and compared to the standard plane wave spectrum (PWS) reconstruction technique, making it possible to arrive at a conclusion as to which one to use in order to make the final analysis.

2.1. Introduction

Near-field measurements have become widely used in antenna tests and diagnoses. This is due to the fact that they can be used to perform antenna far-field measurements inside rather smaller anechoic chambers in relatively cost-effective way. In some cases, it is not practical, if not

impossible, to measure antenna fields in the normal far-field range. In this type of situation, the distance from the probes to the radiating elements may be too long that moving the antenna from its operating environment to the measuring range becomes impractical, or measuring the desired pattern data may require too much time in the far-field range. Therefore, it is quite useful to be able to determine antenna far-field patterns from measurements done in near-field regions. Moreover, near-field measurements allow field reconstructions on other surfaces which can be useful for diagnosis purposes. Due to the compact nature of the electromagnetic fields, near-field measurements basically contain more data about the radiator compared to the ones performed in the far-field range.

Recently, some new near-field measurement tools have emerged for measuring the magnetic fields [1], [28], [29]. For instance, RFxpert is the only real-time, compact bench-top antenna measurement tool, available at the moment. It is a magnetic, very near-field device which does not require a shielded room to run the system and enables designers to measure antenna patterns in less than a second. It saves time and cost by reducing reliance upon time consuming and costly anechoic chambers. These tools usually use a finite ground plane separating the probe array from the RF and digital circuitry. Therefore, this ground plane needs characterization for its effect on the measurement process. If the device under test is a microwave or high-speed digital circuit, the current and field perturbation due to the ground plane can be tolerated to some extent. If the device under test is an antenna, the perturbation can be significant, requiring additional attention when completing a near-field to far-field transformation. In this chapter, a new algorithm has been proposed, which is suitable for measurement tools with a ground plane next to their probe array. The earliest works on near-field to far-field transformation and even field-reconstruction

were based on the modal expansion method, including the popular plane wave spectrum (PWS). In the modal expansion methods, fields radiated by antenna under test (AUT) are expanded in terms of planar, cylindrical, or spherical wave functions. As such, the measured near fields are used to calculate the unknown expansion coefficients. Then, the expanded modes are used for far-field transformations [4]–[6], [30], [31]. In the case of the sinusoidal orthogonal modes, the expansion coefficients can be easily obtained by applying the classic Fourier transform to the measured fields. The modal expansion based methods can even benefit from hardware-accelerated FFT calculators. This fact makes modal expansions a good choice for EMC/EMI diagnoses, where a real-time response is usually quite essential.

In the second class of methods, measured fields are first back-projected to a fictitious source surface and then a far-field transformation takes place based on the reconstructed currents. In [9], a planar array of infinitesimal magnetic dipoles is used as the fictitious surface, which itself is assumed to be laid on an infinite perfect electric conductor (PEC) plane. Then, antenna far-fields are calculated through the array far-field relations and the complex dipoles amplitudes. Source reconstruction of fields can also be accomplished using an equivalent closed surface enclosing all the volume (non-free space) [32], [9]. Compared to the previous class of methods, back-projection based methods are less sensitive to noise and distortions in measurement because of having an extra degree of freedom which is the fictitious surface describing parameters. In the case of the modal expansion method, one may require explicit use of low-pass filters to reject unwanted noise [5]. On the other hand, the process time of the back-projection based method is more than that of the modal expansion techniques and the method is subject to inherent truncation due to normalization techniques. Several attempts have been made to enhance the accuracy of the

reconstructed currents and the far-field patterns, including the one proposed by Quijano *et al.* [9]. In their proposed algorithm, the AUT is modeled by a closed, arbitrary fictitious surface containing all the materials which differ from free space. The reason is this way all electromagnetic sources will contained in this surface. It also uses both electric and magnetic currents on this surface. Then Love's equivalence principle is applied by enforcing the tangential E and H fields to vanish immediately inside the fictitious surface [9]. Other studies tried to find equivalent sources composed of electric and/or magnetic dipoles through the least squares method or other iterative minimization techniques [12], [33]. There also have been a few ground plane filtering algorithms introduced in the literature where either Fresnel's reflection coefficients [34] or the Source Reconstruction Method (SRM) [35] are used for filtering purposes. Still, in all these studies the ground plane and the probe(s) are assumed to be both well separated and not coupled.

The remainder of this chapter is structured as follows. In Section II, the main problem and its equivalent model are described, the principles of the proposed algorithm are explained, four different models are introduced for ground filtering, and finally, discretization method and relations are presented. In Section III, four numerical examples are used to investigate the performance of the algorithm followed by a discussion about parameter selection. Then, the results of the proposed algorithm are compared to those of a full-wave 3D simulator (Ansoft HFSS) and a PWS method. The conclusions are presented in Section IV.

2.2. Theory

2.2.1. Problem Description

As can be seen in Fig. 2.1(a), the problem can be described as a radiator (AUT) placed on top of an array of H-field probes. The H-field probe array is placed on top of a finite PEC ground plane. In a typical measurement scenario, a single tone frequency synthesizer powers the AUT, which illuminates the probe array. It is assumed the power incident on the probe array is strong enough to be detected (the coupling between the ground plane and the AUT is not strong enough to change the radiator's input impedance). The complex voltages read out of the probes are assumed to represent the magnetic field intensity at the centers of the probes. In this study, it is also assumed the interaction between the probe array and the DUT is negligible. This assumption could be verified in the results section (test cases 2 and 3) where a comparison of FF patterns obtained from experimental results (with interactions) and from HFSS simulations (without interactions) is presented.

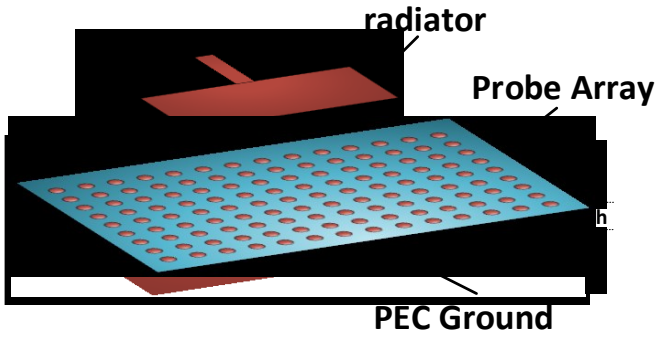

(a)

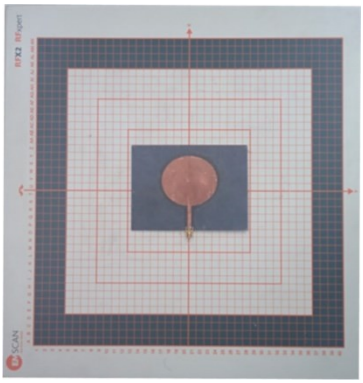

(b)

Fig. 2.1. A typical near-field measurement scenario in the presence of a ground: (a) Schematic view (b) EM-Scan RFxpert measurement device.

2.2.2. Equivalent Problem

To alleviate the effects introduced by the ground plane, especially those affecting far-field patterns, one can use SRM. In the normal SRM approach, one tries to back-project the measured electromagnetic fields to a fictitious surface that reconstructs the measured fields [11], [16]. However, in our method, we need to bring into account the effect of the ground plane by back-projecting the measured fields back to two surfaces simultaneously, which are the fictitious surface

(representing the radiator) and the rectangular ground plane. If the ground plane was electrically large enough comparing to the size of the AUT, image theory would be a simple replacement for this problem. But for a wideband scanner (600MHz and 6 GHz) this assumption does not always hold and scattering from the finite ground edges start to play a major role in the radiations.

We presume the size and position of the radiator are the only information we are given. As such, we do not have any information about either the shape or the materials of the radiator. Retrospectively, various kinds of test models have been used to approximate the radiator including the ones using electric [32] or magnetic [7] current sheets and closed surfaces of both electric and magnetic currents [9]. In the case of a closed surface, we can optionally apply the boundary conditions of zero tangential E and H inside the fictitious surface (inside) [9] to increase the accuracy. In this chapter, all approaches are investigated and the best one is selected based on the

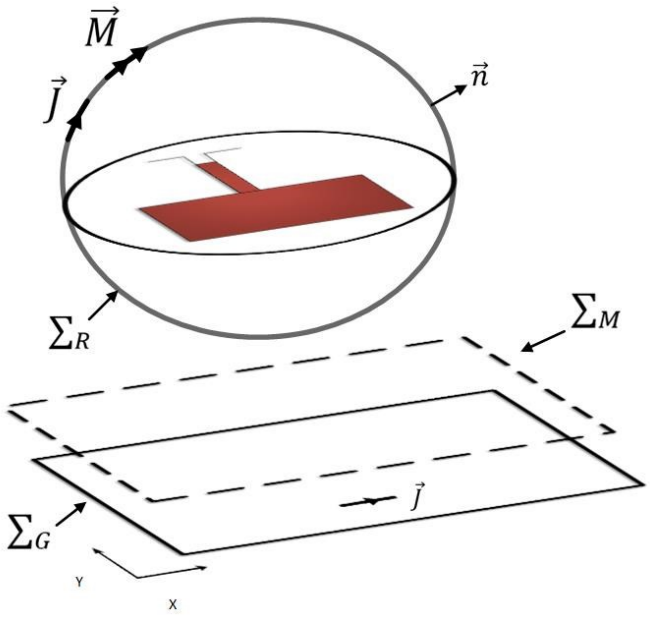

Fig. 2.2. Depiction of a source reconstruction problem in which H-field probes are immediately next to a rectangular metallic ground plane.

far-field and near-field accuracies. Fig. 2.2 depicts a reference figure for the ground filtered source reconstruction problem discussed in this study. The input information for the problem is the complex values of the tangential magnetic field on the planar measurement surface denoted by Σ_M along with the position and the size of the radiator.

In this work we assume the measurement setup is planar but the idea can easily be generalized to cylindrical and spherical measurement setups as well. The desired outcomes of the algorithm are 1) the tangential electromagnetic fields (E or H) over the fictitious surface (denoted by Σ_R) and 2) the far-field radiation pattern of the radiator (in free space). Therefore, the algorithm should filter out the effect of the finite ground plane denoted by Σ_G. We should remember that in case a closed surface is used as the fictitious surface, it should enclose the volume containing all materials that differ from free space.

2.2.3. Integral Equation

The integral equations can be constructed by relating the sources, measured fields and boundary conditions present in the original problem [26]. For the problem described in the previous section, integral equations, which link the source currents and electric/magnetic fields in free space, can be formed as follows (assuming $e^{j\omega t}$ time dependence) [26],

$$\boldsymbol{E}(\boldsymbol{r}) = -\eta_0 \mathbf{L}(\boldsymbol{J};\boldsymbol{r}) + \mathbf{K}(\boldsymbol{M};\boldsymbol{r}) \tag{37}$$

$$\boldsymbol{H}(\boldsymbol{r}) = -\frac{1}{\eta_0}\mathbf{L}(\boldsymbol{M};\boldsymbol{r}) - \mathbf{K}(\boldsymbol{J};\boldsymbol{r}) \tag{38}$$

where

$$\mathbf{L}(\boldsymbol{J};\boldsymbol{r}) = jk_0 \int_{\Sigma_R+\Sigma_G} \left[\boldsymbol{J}(\boldsymbol{r}') + \frac{1}{k_0^2}\nabla\nabla'_s.\boldsymbol{J}(\boldsymbol{r}')\right] g(\boldsymbol{r},\boldsymbol{r}')ds' \tag{39}$$

$$\mathbf{K}(\boldsymbol{M};\boldsymbol{r}) = \int_{\Sigma_R+\Sigma_G} \boldsymbol{M}(\boldsymbol{r}') \times \nabla g(\boldsymbol{r},\boldsymbol{r}')ds' \tag{40}$$

$$g(r,r') = \frac{e^{-jk_0|\boldsymbol{r}-\boldsymbol{r}'|}}{4\pi|\boldsymbol{r}-\boldsymbol{r}'|} \tag{41}$$

where $\eta_0 = \sqrt{\frac{\mu_0}{\epsilon_0}}$, $k_0 = \omega\sqrt{\mu_0\epsilon_0}$ and ∇_s' is the source surface divergence factor.

So far we have related fields in free space to an arbitrary distribution of sources, without forcing any relation between sources present in the space or applying any boundary conditions due to the presence of the ground. Fig. 2.3 shows two typical setups used to constitute the integral equations. The first and second setups represent scenarios with closed and open fictitious surfaces, respectively. Following, four different scenarios are defined here and investigated in the later sections.

2.2.3.1. Pure Electric Currents

In this scenario, a fictitious layer only contains electric currents (*J*) and therefore it is applicable to both setups depicted in Fig. 2.3. There are a few issues in this type of scenario. First, it does not result in a relatively accurate source reconstruction, especially compared to those with both electric and magnetic currents [9]. Second, looking to far-field results, the source setup will not be complete if the fictitious layer is a rectangular plane. As such, far-field accuracy degrades moving toward the $\theta = 90^0$ plane. The system of equations for this setup can be summarized as,

$$\boldsymbol{n} \times \left[-\mathbf{K}\left(\boldsymbol{J_R}; \boldsymbol{r}_{\sum_M}\right) - \mathbf{K}\left(\boldsymbol{J_G}; \boldsymbol{r}_{\sum_M}\right)\right] = \boldsymbol{n} \times \boldsymbol{H_M}\left(\boldsymbol{r}_{\sum_M}\right) \tag{42}$$

$$\boldsymbol{n} \times \left[-\eta_0(\mathbf{L}\left(\boldsymbol{J_R}; \boldsymbol{r}_{\sum_G}\right) - \eta_0\mathbf{L}\left(\boldsymbol{J_G}; \boldsymbol{r}_{\sum_G}\right)\right] = \mathbf{0} \tag{43}$$

where $\boldsymbol{H_M}\left(\boldsymbol{r}_{\sum_M}\right)$ represents the measured magnetic field (only the tangential magnetic components are measured).

2.2.3.2. Electric and Magnetic Currents with no Inner Boundary Conditions

In this scenario, both electric and magnetic currents (J_S, M_S) are present on the fictitious surface. Compared to the pure electric currents setup, they can better approximate the original fields and can also extrapolate far-fields toward the $\theta = 90^0$ plane, even if the fictitious plane is planar. Since Love's equivalence boundary condition is not applied here, back-projection accuracy might get reduced. On the other hand, the method is applicable to both open and closed (Fig. 2.3) setups. Compared to the pure *J* scenario, the final matrix has twice as many sources, which makes the method over-complete. This fact will not be an issue when it comes to solving the problem, since the effect of having an under determined matrix will be taken care of using the T-SVD regularization technique. The system of equations for this setup can be formed as,

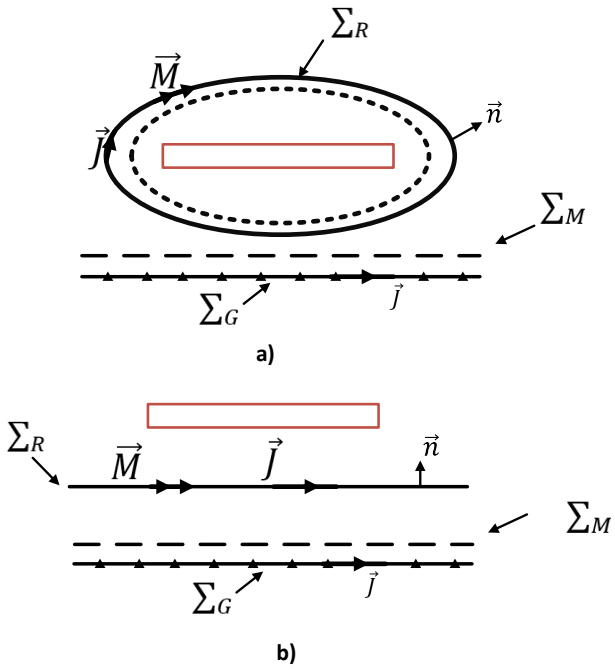

Fig. 2.3 The depiction of the equivalent problem for source reconstruction, a) Closed fictitious surface and b) open fictitious surface. Dashed line represents the surface on which zero field boundary condition can be applied

$$\boldsymbol{n}\times\left(-\frac{1}{\eta_0}\mathbf{L}(\boldsymbol{M_R};\boldsymbol{r}_{\sum_M})-\mathbf{K}(\boldsymbol{J_R};\boldsymbol{r}_{\sum_M})-\mathbf{K}(\boldsymbol{J_G};\boldsymbol{r}_{\sum_M})\right)=\boldsymbol{n}\times\boldsymbol{H_M}(\boldsymbol{r}_{\sum_M}) \tag{44}$$

$$\boldsymbol{n}\times\left(-\eta_0(\mathbf{L}(\boldsymbol{J_R};\boldsymbol{r}_{\Sigma_G})-\eta_0\mathbf{L}(\boldsymbol{J_G};\boldsymbol{r}_{\Sigma_G})+\mathbf{K}(\boldsymbol{M}_R;\boldsymbol{r}_{\Sigma_G})\right)=\mathbf{0} \tag{45}$$

2.2.3.3.Electric and Magnetic Currents with Love's Equivalence Boundary Condition

In this scenario, there are both electric and magnetic currents present on the fictitious layer. Also, a boundary condition of zero tangential E and H is applied to enforce Love's equivalence theorem [9]. This boundary condition implicitly relates the electric and magnetic currents on the fictitious layer. Using electromagnetic quantities [11], [18], [19], the equivalent boundary condition can be derived as [9],

$$-\eta_0\mathbf{L}(\boldsymbol{J_R};\boldsymbol{r}_{\sum_R})+\mathbf{K}(\boldsymbol{M_R};\boldsymbol{r}_{\sum_R})-\eta_0\mathbf{L}(\boldsymbol{J_G};\boldsymbol{r}_{\sum_R})=-\frac{\mathbf{1}}{\mathbf{2}}\boldsymbol{M}(\boldsymbol{r}_{\sum_R}) \tag{46}$$

The classical jump condition can be used to escape having to deal with the inaccuracy introduced by an integral equation of the second kind even though it is associated to well conditioning [11], [19]. Hence, the integral equation in (46) can be rewritten by a limit of a first kind integral equation and the system of equations becomes as follows,

$$\boldsymbol{n}\times\left(-\frac{1}{\eta_0}\mathbf{L}(\boldsymbol{M_R};\boldsymbol{r}_{\sum_M})-\mathbf{K}(\boldsymbol{J_R};\boldsymbol{r}_{\sum_M})-\mathbf{K}(\boldsymbol{J_G};\boldsymbol{r}_{\sum_M})\right)=\boldsymbol{n}\times\boldsymbol{H_M}(\boldsymbol{r}_{\sum_M}) \tag{47}$$

$$\lim_{\boldsymbol{r}\to\sum_{\boldsymbol{R}}^{-}}\boldsymbol{n}\times\left(-\eta_0\mathbf{L}(\boldsymbol{J_R};\boldsymbol{r})+\mathbf{K}(\boldsymbol{M_R};\boldsymbol{r})-\eta_0\mathbf{L}(\boldsymbol{J_G};\boldsymbol{r})\right)=\mathbf{0} \tag{48}$$

$$\boldsymbol{n}\times\left(-\eta_0(\mathbf{L}(\boldsymbol{J_R};\boldsymbol{r}_{\sum_G})-\eta_0\mathbf{L}(\boldsymbol{J_G};\boldsymbol{r}_{\sum_G})+\boldsymbol{K}(\boldsymbol{M}_R;\boldsymbol{r}_{\sum_G})\right)=\mathbf{0} \tag{49}$$

The tangential electric field should go to zero as we move towards the interior of the space enclosed by the fictitious surface. Imposing this condition is equivalent to holding the field equivalence problem [11], [20], i.e. $\boldsymbol{M} = -\boldsymbol{n} \times \boldsymbol{E},\ \boldsymbol{J} = \boldsymbol{n} \times \boldsymbol{H}$. This approach has been shown to be the most accurate in terms of reconstructed fields [11], [16] but is only applicable to the closed fictitious surfaces.

2.2.3.4.Pure Electric Currents with a PMC Boundary Condition

In this scenario, the fictitious layer only contains electric currents and is only applicable to the closed fictitious surface due to the PMC boundary enforced on the fictitious surface. Therefore, tangential magnetic fields on the fictitious layer are forced to be zero. Since there are no magnetic currents on the fictitious surface, the right-hand side of (46) goes to zero. As a direct consequence, it does not end up in an integral equation of the second kind and using the jump condition is not necessary. The system of equations for this scenario can be written as follows,

$$\boldsymbol{n} \times \left(\mathbf{K}(\boldsymbol{J_R}; \boldsymbol{r}_{\sum_M}) - \mathbf{K}(\boldsymbol{J_G}; \boldsymbol{r}_{\sum_M})\right) = \boldsymbol{n} \times \boldsymbol{H_M}(\boldsymbol{r}_{\sum_M}) \tag{50}$$

$$\boldsymbol{n} \times \left(\mathbf{K}(\boldsymbol{J_R}; \boldsymbol{r}_{\sum_R}) - \mathbf{K}(\boldsymbol{J_G}; \boldsymbol{r}_{\sum_R})\right) = \mathbf{0} \tag{51}$$

$$\boldsymbol{n} \times \left(-\eta_0(\mathbf{L}(\boldsymbol{J_R}; \boldsymbol{r}_{\sum_G}) - \eta_0 \mathbf{L}(\boldsymbol{J_G}; \boldsymbol{r}_{\sum_G})\right) = \mathbf{0} \tag{52}$$

2.2.4. MOM Discretization

So far, the total setup is illustrated and the integral equations of the problem are defined. In this section, the discretization process is presented. All regions in Fig. 2.3, excluding the measurement surface (ΣM), should be discretized using triangular meshes. RWG basis functions [39] are utilized to expand the vector source currents on the source surfaces for both electric and

magnetic currents. An RWG basis function's normal(to edge) component is continuous on the shared edge on which it is defined. Hence, the line charges on the edges of the triangles can be neglected [17], [21]. They also represent a complete basis for expanding both currents and charges [40]. It also has been shown to be very efficient to model electromagnetic structures, even those with shape edges like a cube's [39],

$$\boldsymbol{J}_{\sum_X}(\boldsymbol{r}') = \sum_{tri(i)\in\sum_X} C_i \boldsymbol{f}_i(\boldsymbol{r}')\,,\ \boldsymbol{M}_{\sum_X}(\boldsymbol{r}') = \eta_0 \sum_{tri(i)\in\sum_X} C_i \boldsymbol{f}_i(\boldsymbol{r}') \tag{53}$$

where η_0 is used as a factor for normalization purposes without which the final interaction matrix would be unbalanced in terms of amplitudes of different source cells. It would both affect the accuracy and well-posedness of the final matrix. The form of the interaction matrix differs depending on the type of scenario used. However, instead of describing the discretization process for all scenarios, the third scenario is selected as the most general one, which contains both electric and magnetic currents on the fictitious surface besides a boundary condition. Thus, it is a general scenario, effectively, and the approach can easily be generalized to account for the other integral equations as well. The first equation in the system of equations (47) forces all sources in the system to radiate the same fields as the measured ones on the measurement surface. The MOM discretization for this part is relatively straightforward since there is no need for test functions. However, for the other two equations, test functions must be used to increase the accuracy. Therefore, both point-matched and RWG tested fields for measured and boundary conditioned values are required, respectively. As such, two discretization techniques for the operators are required. Using the RWG basis functions, one can utilize the feature of continuity of normal

component on the shared edge and define the L operators for testing and point-matching as [17], [23],

$$\mathbf{L}^1_{m,n} := jk_0 \int_{S_m} d\boldsymbol{r} \boldsymbol{f}_m(\boldsymbol{r}) . \int_{S_n} d\boldsymbol{r}' g(\boldsymbol{r},\boldsymbol{r}') \boldsymbol{f}_n(\boldsymbol{r}') - \frac{j}{k_0} \int_{S_m} d\boldsymbol{r} \nabla . \boldsymbol{f}_m(\boldsymbol{r}) . \int_{S_n} d\boldsymbol{r}' g(\boldsymbol{r},\boldsymbol{r}') \boldsymbol{\nabla}' . \boldsymbol{f}_n(\boldsymbol{r}') \quad (54)$$

$$\mathbf{L}^2_{m,n} := \left[jk_0 \int_{S_n} \left[\boldsymbol{J}(\boldsymbol{r}') \frac{1}{k_0^2} \nabla \nabla'_s . \boldsymbol{J}(\boldsymbol{r}') \right] g(\boldsymbol{r},\boldsymbol{r}') \, ds \right]_{(\boldsymbol{r} \to \boldsymbol{r_m})} . \hat{a}_m \quad (55)$$

where S_m and S_n are source and test triangles, r_m is the coordinate of the corresponding observation point on the measurement plane and $\hat{a}_m$ is the unit tangential vector at r_m, which, in the planar case, is either $\hat{a}_x$ or $\hat{a}_y$. Finally, m and n represent the mth row and nth column in the interaction matrix, respectively. The K operator can also be discretized as follows,

$$\mathbf{K}^1_{n,m} := jk_0 \int_{S_m} d\boldsymbol{r} \boldsymbol{f}_m(\boldsymbol{r}) . \int_{S_n} d\boldsymbol{r}' [\boldsymbol{f}_n(\boldsymbol{r}') \times \nabla' g(\boldsymbol{r},\boldsymbol{r}')] \quad (56)$$

$$\mathbf{K}^2_{n,m} := jk_0 \left[\int_{S_n} d\boldsymbol{r}' [\boldsymbol{f}_n(\boldsymbol{r}') \times \nabla' g(\boldsymbol{r},\boldsymbol{r}')] \right]_{(\boldsymbol{r} \to \boldsymbol{r_m})} . \hat{a}_m \quad (57)$$

In the above equation, the cross product can be extracted out of the inner integral, which would make the integration process easier [41]. As the source and observation triangles overlap or share an edge, both inner and outer integrals become singular. Therefore, the calculation of (54-57) needs special attention, as follows [26], [37], [42]–[44]. The singular parts of the inner integrals are extracted and integrated using analytical methods and the non-singular part is solved by an adaptive quadrature method [25]. If the inner and outer integrals share an edge, then the inner integral becomes singular on that edge. For the L operator, this singularity is already taken care of by extracting the gradient operator out of the inner integral [23]. However, this singularity is still there for the K operator. Despite the singular behavior of the integrand on the whole edge, we can

evaluate the integral quite easily using an adaptive numerical quadrature method as the singularity is a mild logarithmic one [23], [26]. In this chapter, a triangular adaptive integral is used in which we keep dividing the triangles into three smaller ones until a specific convergence criterion is met [25].

Since (18) is a limit of a boundary condition, it requires more attention when it comes to the discretization step. As suggested in [9], we can move toward the center of ΣR and build an inward-offset of it and then apply a zero boundary condition on it. At the end, the total system of equations can be summarized as,

$$\eta_0 \begin{bmatrix} -\frac{1}{\eta_0}\mathbf{K}^2_{M,R} & -\frac{1}{\eta_0}\mathbf{L}^2_{M,R} & -\frac{1}{\eta_0}\mathbf{K}^2_{M,G} \\ -\mathbf{L}^1_{R^-,R} & \mathbf{K}^1_{R^-,R} & -\mathbf{L}^1_{R^-,G} \\ -\mathbf{L}^1_{G,R} & \mathbf{K}^1_{M,G} & \mathbf{L}^1_{M,G} \end{bmatrix} \begin{bmatrix} C_{js} \\ C_{ms} \\ C_{jg} \end{bmatrix} = \begin{bmatrix} H_M \\ 0 \\ 0 \end{bmatrix} \tag{58}$$

where $X_{a,b}$ for the operator X is an interaction block between sources to observation points on surface a and surface b, respectively. Generally, the system of equations is an over-determined rectangular matrix, so we are dealing with a least squares problem.

2.2.5. Regularization

To solve (58), we can use a direct method based on singular value decomposition (SVD), especially because we have a non-square noisy matrix to deal with. Looking at (58), the first equation is point matched whereas the other two are RWG tested. Considering this fact, one might wonder whether further equalization (multiplying the first equation by an equalizing factor) is necessary before the normalization step. However, after taking a closer look and by considering the norms of different blocks of the matrix, we can conclude that the form of the matrix as in (58)

leads to a relatively well-conditioned matrix whose blocks have similar norms. In another perspective, since the result of the RWG tested fields show the magnitude of the field normal to the element center, we are basically comparing consistent values along different equations. Afterwards, we proceed to apply SVD to the matrix and use the truncated SVD (T-SVD) technique [27] to regularize the problem. To determine the cutting threshold, the well-known L-curve is used [27].

2.3. Results and Discussion

2.3.1. Overview

To verify the accuracy of the MOM code, integral equations and the models introduced in the previous section, four test scenarios (using J&PMC, Pure J, J&M&PEC, and J&M) are discussed. For verification purposes, for three of the scenarios, the outcomes of the proposed algorithms are compared with those of 3D full wave simulations (Ansoft HFSS) and a PWS method. Whereas in the first scenario the accuracy of the underlying home-developed MOM code is verified. Since before testing the proposed algorithm, it must be made sure the underlying MOM code is accurate and reliable. In the second and the third test scenarios, the proposed algorithms are discussed. Basically, a typical AUT (slot and monopole) is chosen. The AUT is powered by a signal generator and placed on top of the NF measurement probe array as shown in Fig. 2.1(a). Then, from the measured data, the AUT FF pattern is calculated using different integral formulations and compared with that of the simulation (using HFSS with no ground plane present). For a better comparison of FF patterns 1) both FF components are normalized (single reference for both) and 2) the 1 dB accuracy of each algorithm is calculated accordingly. The 1 dB accuracy is the minimum angle through which the total field pattern deviates 1 dB from the reference free-

space pattern (HFSS). In the fourth scenario, we seek a quantitative comparison of the reconstructed currents and the real ones with data stemming from a 3D full-wave simulator (HFSS).

2.3.2. Plane Wave Scattering

Before testing the proposed method on different scenarios, the accuracy of the underlying MOM code must be verified. Therefore, the MOM code is used to analyze a known scattering problem and its results are compared to those of a reliable 3D full-wave simulator (Ansoft HFSS). The scattering of a finite plane is selected as a secure check because it is similar to the conducting plane backing the probe array. In Fig. 2.4, a PEC rectangle with dimensions $\frac{\lambda}{2} \times \frac{\lambda}{2}$ is illuminated by a plane wave at a normal incident angle and $(a_x + a_y)$ polarization. The scattering problem is solved both by HFSS and the home implemented MOM code in Matlab using different mesh sizes. In HFSS, the solver is forced to perform 10 and 13 iterations. The ground plane is discretized using uniform meshes of sizes 1 cm and 0.5 cm, or 0.0033λ and 0.0017λ, respectively, at the operating frequency. It can be seen in Fig. 2.4 that for both cases, as the meshing gets finer, the current density increases in amplitude and concentrates toward the edges of the plane (Fig. 2.4(a), (b) vs Fig. 2.4(c), (d)). In all the cases, the back-scattering results are very stable. In Fig. 2.5, the back-scattering results are presented. Since the plane wave is both x and y polarized, both patterns look similar in the 0° and 90°cuts.

1

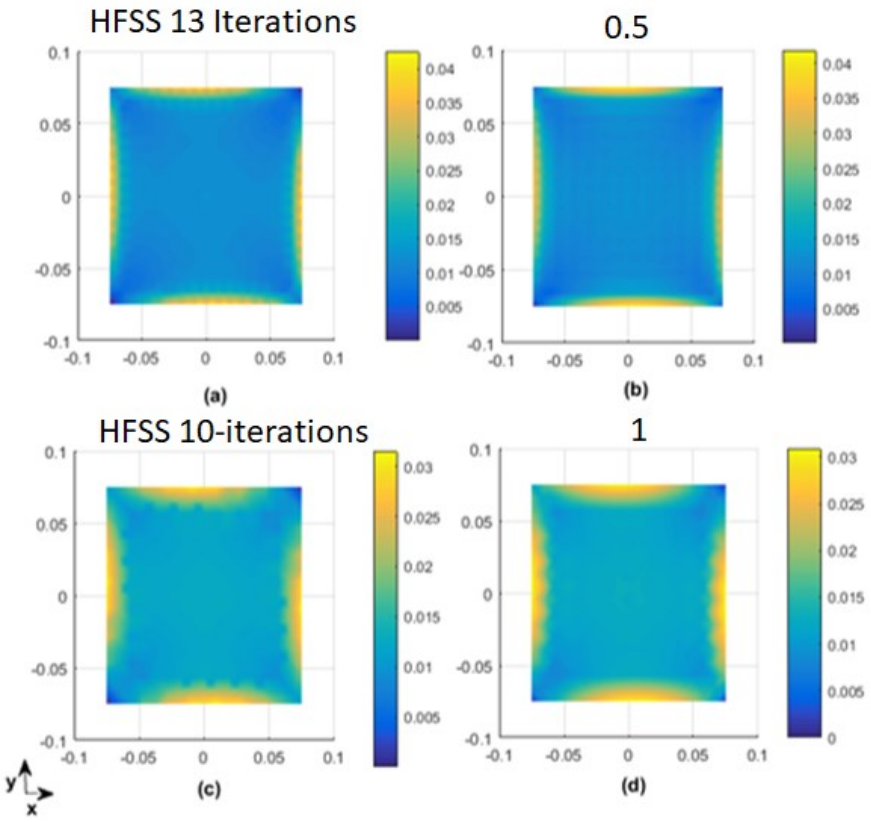

Fig. 2.4. Current density complex magnitude calculated using (a) HFSS with 13 iterations, (b) Matlab code with 13 iterations and a 0.5 cm size mesh, (c) HFSS with 10 iterations, and (d) Matlab code with 10 iterations and a 1 cm size mesh.

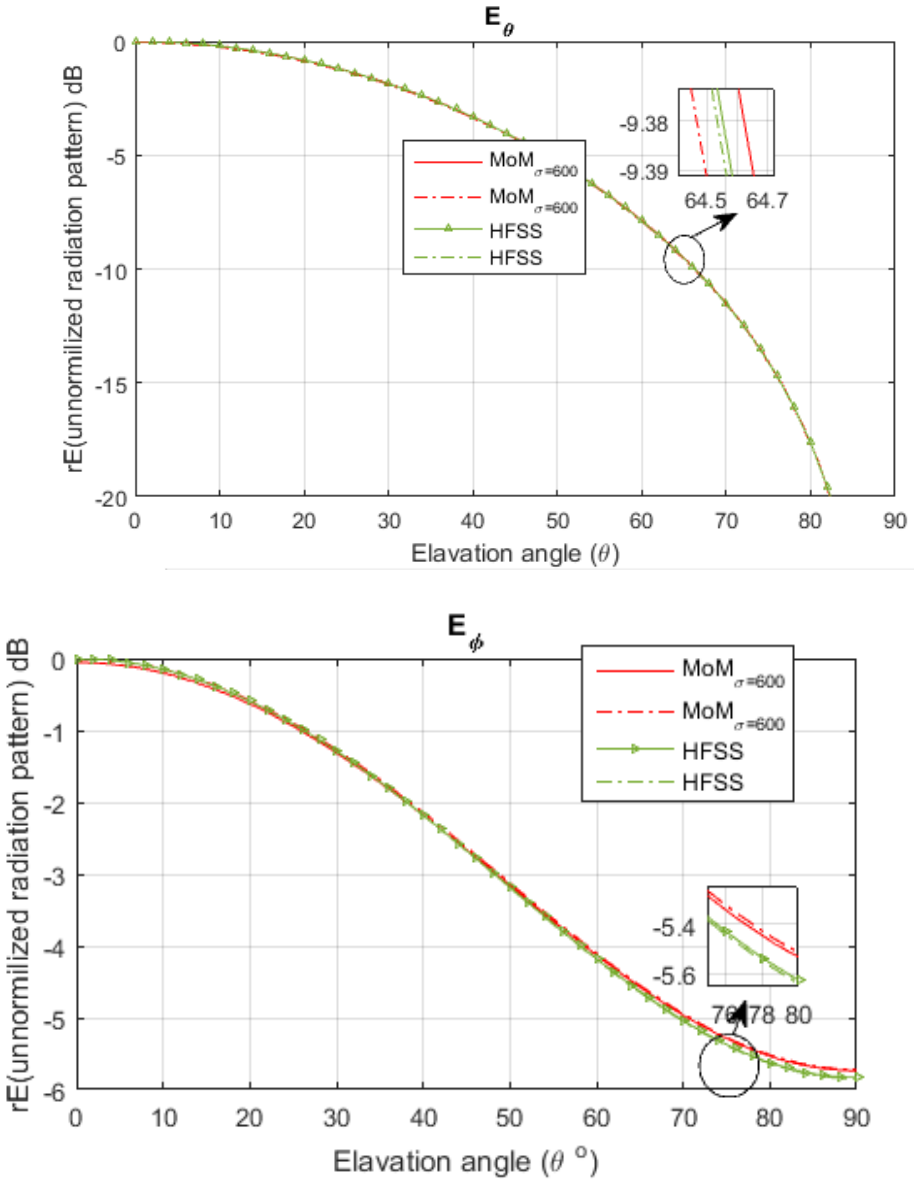

Fig. 2.5. Normalized Far-field magnitudes (a) E_θ and (b) E_ϕ.

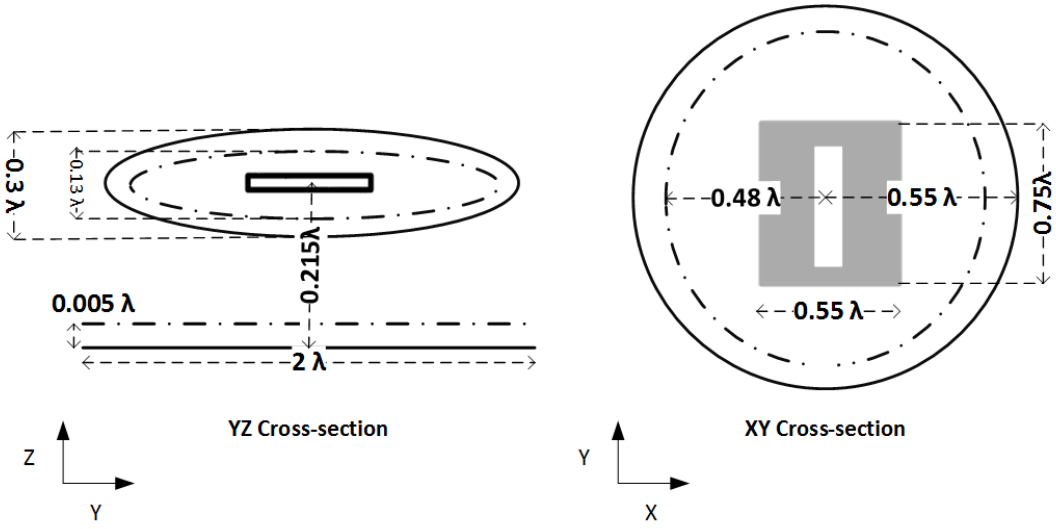

(a)

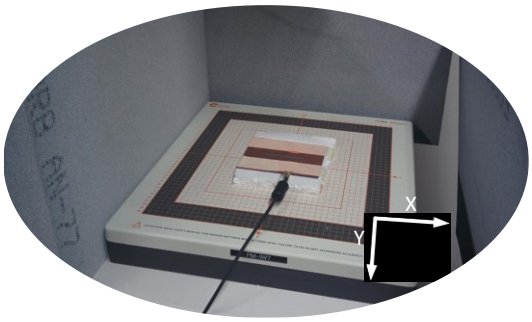

(b)

Fig. 2.6. (a) Schematic of the slot antenna and the fictitious surfaces, (b) Measurement configuration.

2.3.3. Slot Antenna at 2 GHz (Measured Data)

As a second example, a slot antenna is selected as shown in Fig. 2.6(a), with dimensions 0.75 λ × 0.55 λ for the PCB and a 0.38 λ × 0.019 λ slot on it. The aperture is excited by a transmission line on the other side with dimensions 0.43 λ × 0.024 λ. The ellipsoid used for the

back-projection has three radii of sizes 0.73 λ, 0.73 λ and 0.2 λ using a meshing element length of 0.093 λ. The dashed ellipsoid (used for Love's boundary condition) has three radii of sizes 0.64 λ, 0.64 λ and 0.174 λ with a meshing element length of 0.081 λ. The center of the ellipsoid is 4.2 cm away from the fictitious surface, which is backed by a PEC 1 mm away from it. The data for this scenario are measured using a near-field scanner consisting of a 40×40 near-field H-probe array where the probe spacing is 1 cm in both directions. The absorber panels are placed to reduce the effects of multiple reflections.

Fig. 2.7 depicts the comparison of E_θ and $E_\phi$and the detailed accuracy range with 1dB threshold can be found in Table I. On average, the method including J and a PMC produces more accurate results up to 64 and 31 degrees compared with 17 and 27 degrees for the conventional PWS method for E_θ and E_ϕ, respectively.

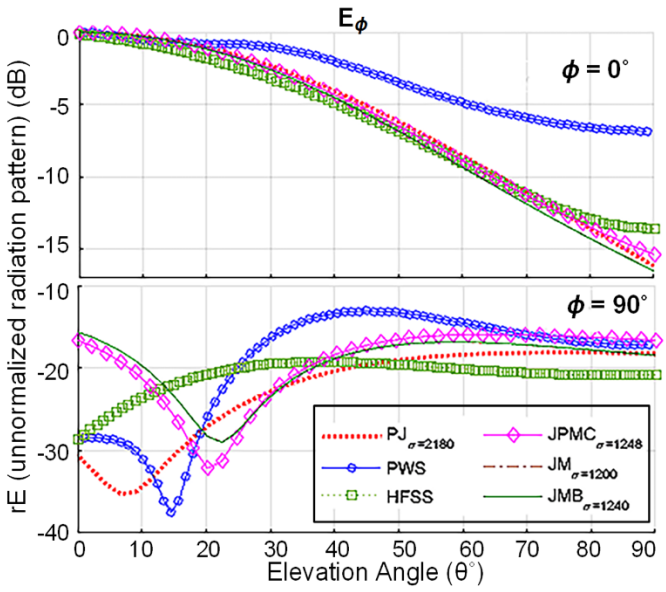

(a)

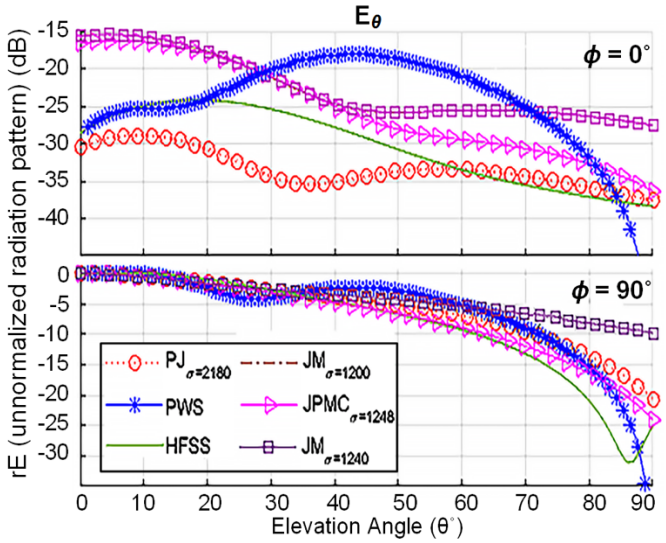

(b)

Fig. 2.7. Comparison between different solvers for (a) E_ϕ and (b) E_θ for the slot antenna.

TABLE I

ANGULAR THRESHOLD OF ACCURACY IN THE PROPOSED METHOD COMPARED WITH THE HFSS RESULTS FOR THE SLOT ANTENNA

	J and PMC	**Pure J**	**J and M, PEC**	**J and M**	**PWS**
$\boldsymbol{E_\theta}$	64-degree	40-degree	34-degree	34-degree	17-degree
$\boldsymbol{E_\phi}$	31-degree	83-degree	39-degree	39-degree	27-degree

2.3.4. Monopole Antenna at 1.5 GHz (Measured Data)

As another example, a monopole antenna is considered with a circular patch, 4 cm in diameter, on a substrate without a ground plane at the back, as shown in Fig. 2.8(a). We choose to model the radiator using an ellipsoid with three radii of sizes 0.6 λ, 0.6 λ and 0.15 λ, which completely encloses the antenna.

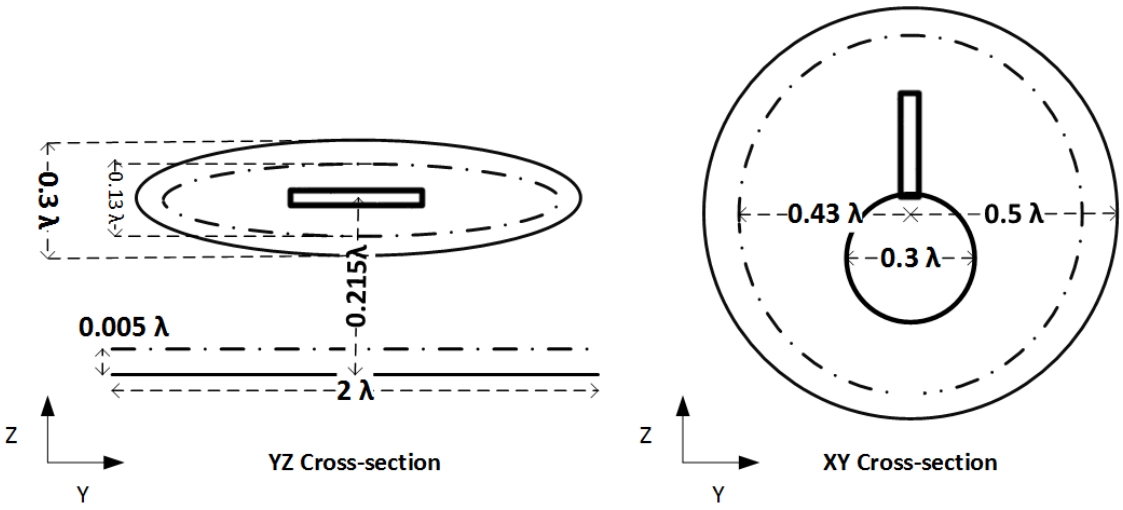
0.3 λ
0.13 λ
0.215λ
0.005 λ
2 λ
Z
Y
YZ Cross-section
0.43 λ
0.5 λ
0.3 λ
Z
Y
XY Cross-section

(a)

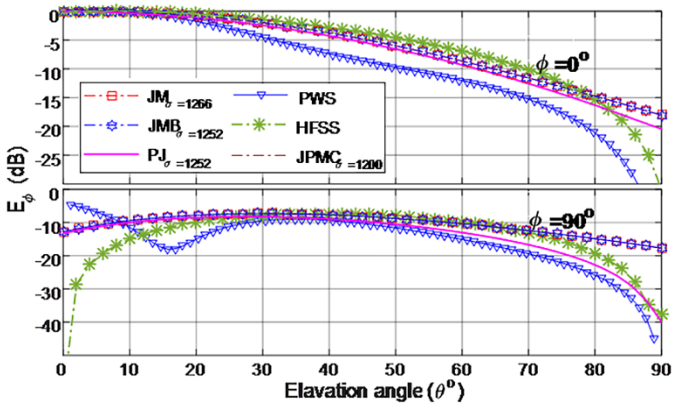
JM_σ =1266
JMB_σ =1252
PJ_σ =1252
PWS
HFSS
JPMC_σ =1200
ϕ =0°
ϕ =90°
E_ϕ (dB)
Elevation angle (θ°)

(b)

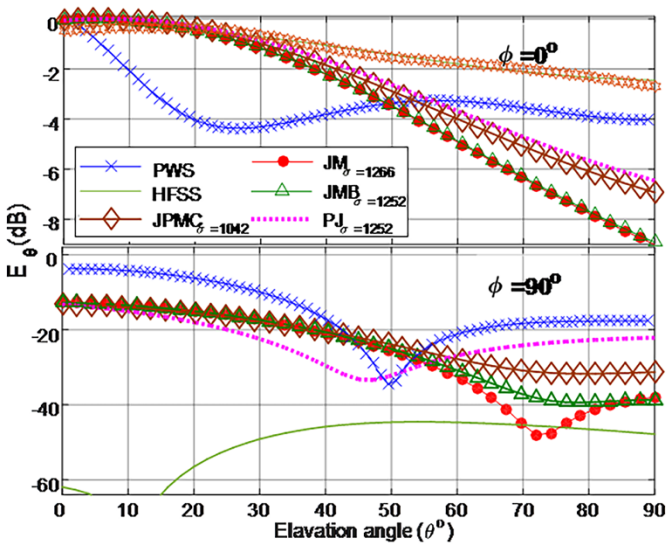

(c)

Fig. 2.8. (a) Depiction of a monopole antenna. Comparison between different solvers for (b) E_{ϕ} and (c) E_{θ} in the monopole antenna.

TABLE II

ANGULAR THRESHOLD OF ACCURACY IN THE PROPOSED METHOD COMPARED WITH THE HFSS RESULTS FOR THE MONOPOLE ANTENNA

	J and PMC	**Pure J**	**J and M, PEC**	**J and M**	**PWS**
$\boldsymbol{E_{\theta}}$	40-deg	34-deg	27-deg	34-deg	7-deg
$\boldsymbol{E_{\phi}}$	54-deg	47-deg	38-deg	54-deg	18-deg

We also choose a smaller ellipsoid with three radii of sizes 0.48 λ, 0.48 λ and 0.12λ for applying Love's boundary condition. The center of the ellipsoids is 4.2 cm above the center of the

fictitious surface, which is backed by a PEC plane 1 mm away from it. The data for this scenario are again measured using a near-field scanner consisting of a 40×40 near-field H-probe array where the probe spacing is 1 cm in both directions. Fig. 2.8(b) shows the comparison between the proposed scenarios and the simulation results (Ansoft HFSS) in terms of 2D far-field radiation pattern cuts. Moreover, Fig. 2.9 compares the 3D radiation pattern of the Pure J (PJ) method with that of the simulation and the PWS. The detailed information about the threshold of accuracy in angles is given in Table II, where J and PMC boundary conditions give the most accurate results up to 40 and 54 degrees compared to the conventional PWS method, which accurate up to 7 and 18 degrees for E_θ and E_ϕ, respectively.

2.3.5. Monopole Antenna at 1.5 GHz (Simulated Data)

Although the far-fields are more interesting, the back-projected fields can give us some idea of how accurate different proposed scenarios can be. Moreover, back projected currents can be used for diagnosis purposes. To have a quantitative comparison of back-projected fields, the monopole setup is repeated in HFSS and the near H-fields are extracted and fed into the algorithm. This way, the exact back-projected currents are known enabling a quantitative comparison. The result of this comparison is presented in Fig. 2.10 and Table III.

As expected, the most accurate results for both J and M currents is for the scenario with J, M and Love's boundary condition (JMB). For a definition of error, we use similar formulas used in [9].

$$\epsilon_J = \frac{||H_{reconstructed} - H_{HFSS}||}{||H_{HFSS}||} \tag{59}$$

$$\epsilon_M = \frac{||E_{reconstructed} - E_{HFSS}||}{||E_{HFSS}||} \tag{60}$$

TABLE III

RECONSTRUCTION ACCURACY OF THE FOUR PROPOSED METHODS COMPARED TO THE HFSS AND SIMPLE MOM RESULTS

	J and PMC	**Pure J**	**J and M, PEC**	**J and M**
ϵ_J	0.30	0.54	0.31	0.7
ϵ_M	NA	NA	0.45	0.94

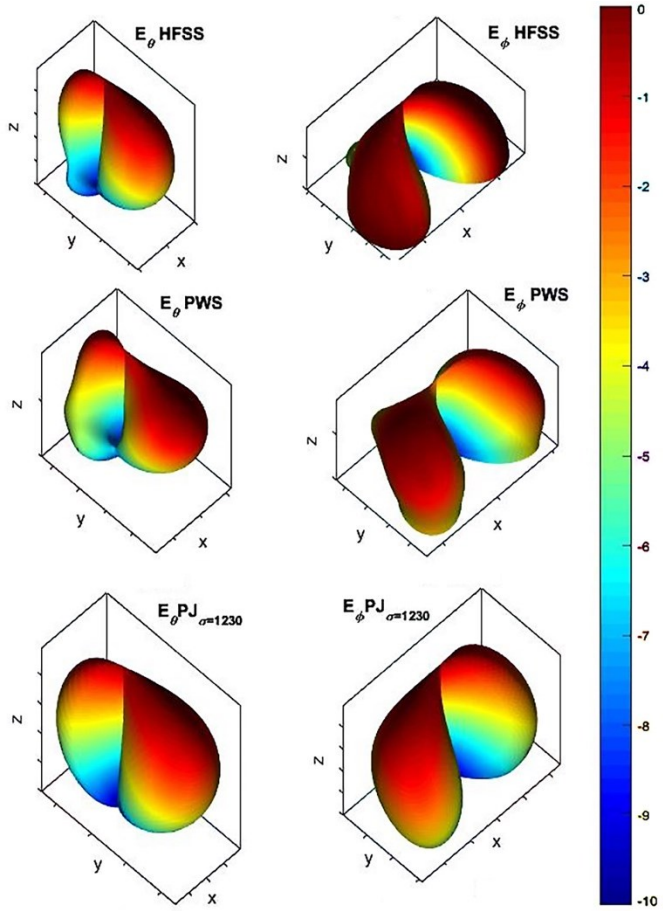

Fig. 2.9. 3D radiation pattern produced by the PJ method compared to those produced by simulation (HFSS) and PWS for the monopole antenna. (All radiation patterns are normalized).

2.3.6. Comparison

The final comparison can be done based on Tables I, II and III. The accuracy for the J only methods is greater than that of the cases where two types of sources exist at the same time. Similar results have been reported in [9]. Considering this fact and that in the J only method the complexity of the problem is much lower than in the others, we can conclude that this approach is the best method for the near-field to far-field transformation. However, for diagnostic purposes the JMB method is superior to the others. Since this method not only provides the back-projected electric

and magnetic fields on the fictitious layer but also produces more accurate results. Therefore, it is the best candidate for diagnostic purposes. It is worth to compare the proposed MOM based methods to the usual MOM, in which the presence of a ground plane is neglected. For this purpose, it is better to have a look at the L-curve to be sure that the method converges.

Fig. 2.11 shows this curve for both the conventional and ground filtered MOM methods. It is clear that for conventional MOM the solution does not converge properly. As such, it is tough to detect the cutting threshold in the T-SVD regularization method.

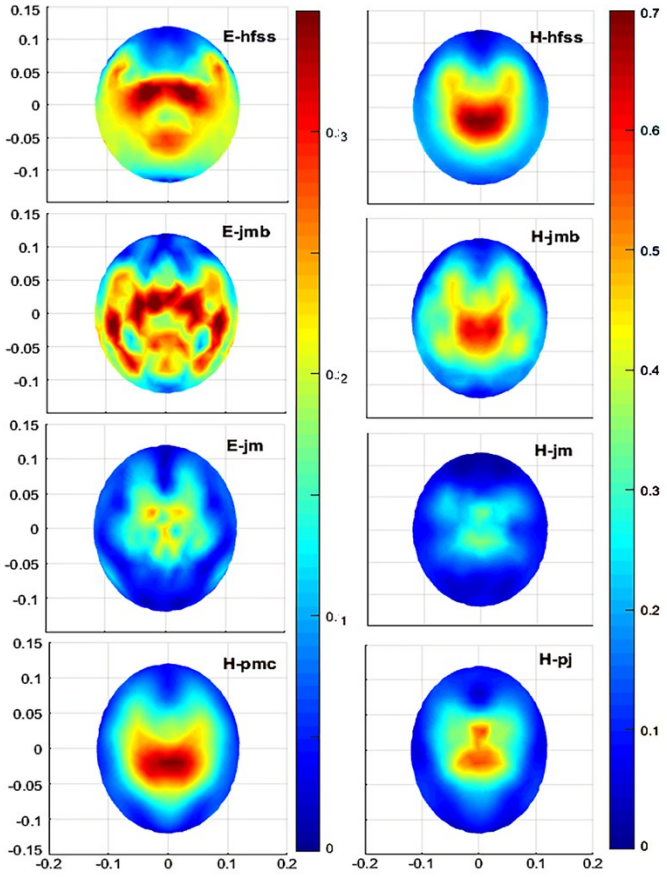

Fig. 2.10. Reconstructed E and H currents on the fictitious layer. Color-map on the right-hand side is for H fields and the one on the left is for *E* Fields.

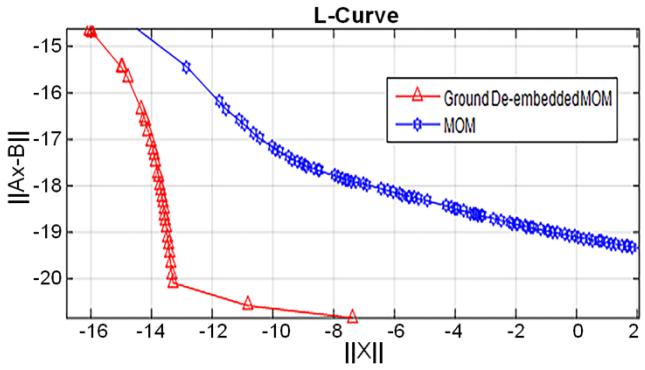

Fig. 2.11. *L*-curve for regularization.

2.4. Conclusion

In this chapter, four different types of reconstruction methods were introduced to address the special type of measurement in which there exists a ground beneath a probe array. Simulation and measurement results showed that for the near-field to far-field transformation, the first scenario (only electric currents on the fictitious layer) is the best method. The provided results of the monopole and slot antennas showed that the far-field accuracy, defined by an angular threshold in degrees of $\boldsymbol{E_\theta}$ and $\boldsymbol{E_\phi}$, has significantly increased from 7° and 18° to 40° and 54° in the first example and from 17° and 27° to 40° and 83° in the second one, respectively. However, it was shown that for diagnosis purposes, the JMB method, which provides both J and M information, is a better option.

Chapter 3

First Order Correction and Equivalent Source Reconstruction Assessment for Practical Multi-plane Magnetic Near-Field Measurements

In this work, a source reconstruction model (SRM) is proposed for correcting and transforming multi-planar magnetic near-field measurements. The correction algorithm provides a way to correct for linear amplitude and phase mismatch error between individual scans as practically this type of error is the dominant one for benchtop scanners. In this work also, various SRM models are compared in terms of reconstructed fields and far-field accuracy looking into their application in planar magnetic measurement. The algorithm and assessment is verified using various simulated and measured test cases.

3.1. Introduction

Near-field (NF) measurement is used for two major applications 1) diagnosis and 2) antenna-parameters calculation. Regarding the diagnosis purposes, the goal of measurements is to reconstruct fields on (or close to) the surface of the device under test (DUT). These reconstructed fields can be used to visualize details of the DUT like manufacturing flaws or unexpected resonant structures. In the case of antenna parameters calculations, the main goal of the measurement is to calculate the far-field (FF) radiation pattern of the DUT in free-space from which other quantities such as directivity, gain, and total radiation power may be derived [45]. Traditionally, near-field measurements have been performed inside anechoic chambers using mechanically swept probes meaning large test system with long measurement times were required. However, a new class of

fast benchtop scanners [1], [28], [29] equipped with fully electronically scanned planar probe arrays have made it easy to perform real-time NF measurement on intentional and non-intentional radiating DUTs inside lab environment and to determine their FF

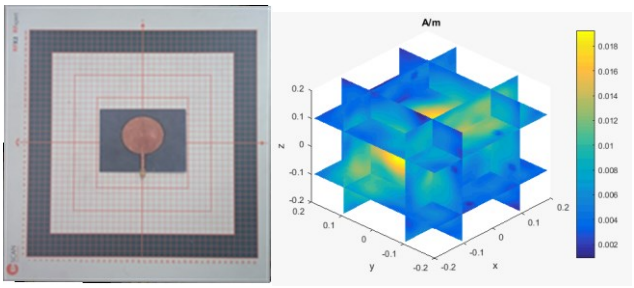

(a) (b)

Fig. 3.1. a) RFX2 Benchtop array scanner, b) 6 planar measurements by rotating the DUT.

radiation pattern. For instance, the scanner in Fig. 3.1(a) enables acquisition of two orthogonal components of the magnetic NF data over a 40×40 cm^2 aperture in less than a second [1]. Benchtop scanners, as with any other planar NF system, measure only a part of the field radiated by the DUT resulting in a limited angular coverage of its radiation pattern. This truncation can be tolerated for certain type of directive DUTs such as high gain antennas with (low beam-width) but is normally not acceptable for low-directive DUTs. This method can also be used to measure high-gain antennas.

This limited angular coverage can be overcome by combining together multiple planar scans. This method can even be used to measure low-directive DUTs with planar scanners. One arrangement multiple scans can be a six-sided box where a single planar aperture acts as a side of the box [8], [21]. Since all 6 sides are treated differently, there is no need to connect them on the

edges. As benchtop scanners use electronically scanned H-field arrays, a single side of the box can be scanned in less than a second. Some time is taken to rotate the DUT before another scan happens but all surfaces can be measured in less than a minute. As direct consequence of device rotation, consistent magnitude and phase error between individual scans is one of the dominant sources of errors. This error might originate, due to the movement, from instrumentation error, cable response change due to cable bending or-input impedance changes of the radiator because of nearby scatterers. In this chapter, it is shown how processing several individual planar data sets can enable both i) accurate calculation full-sphere far-field patterns and ii) accurate correction of the linear amplitude and phase mismatch between individual data sets. A comprehensive assessment of various SRM models will also be proposed looking into practical magnetic near-field setups involving benchtop near-field scanners.

Generally, near-field to far-field transformation and diagnosis methods fall into two major categories of direct and indirect methods. In the direct category, the measured fields are decomposed into a spectrum of outgoing traveling waves that can be directly interpreted or converted to a far-field radiation pattern [4], [5], [30], [46], [47]. In the case of NF planar measurement, the measured fields are expanded into a spectrum of plane-waves (PWS [4], [5], [30], [46], [48]) for obtaining the far-field by using the steepest descent method [47]. This method also allows for calculation of fields on other planar surfaces by forward and backward shifting the plane with some limitations related to the management of evanescent waves in the close vicinity of the DUT [4], [49]. The second category of the near-field to far-field transformation and diagnosis (indirect methods) relies on source reconstruction methods (SRM) consisting of two steps. In the first step, measured electric/magnetic fields are back-projected to equivalent electric (J) and/or magnetic (M) currents distributed on a fictitious surface In the second step, far-field

radiation patterns are calculated from these equivalent currents using free-space's radiation integrals [8], [9], [29], [32], [50], [51]. In [9], the back-projected field's accuracy is shown to be improved by using extra boundary conditions between the tangential electric and magnetic field to enforce a zero radiated field inside the fictitious surface [9], [37]). This improves the accuracy on the back projected equivalent current's and is consistent with equivalence theorem, relating these currents to the field radiated by the DUT on the fictitious surface [38], [45] ($\boldsymbol{M} = -\boldsymbol{n} \times (\boldsymbol{E} - 0)$, $J = \boldsymbol{n} \times (\boldsymbol{H} - 0)$). However, the accuracy improvement comes at the price of increased computational resources because two related equivalent currents (J&M) plus an extra boundary condition are being used. As compared to the direct field expansion method, SRM-based ones exhibit the distinctive feature of a model-based parameter estimation problem [8]. This means the allowable equivalent currents resulting from back-projected near-fields (and, later on, radiated fields) are constrained by the chosen set of basis functions and their radiations on the fictitious surface. Two key parameters defining this set are 1) the type of basis function used to discretize and 2) the shape and size of the fictitious surface.

In the case of closed measurement surfaces, a special category of Huygens theorem based methods have been used [19], [46], [52], [53]. According to field equivalence principle, exterior fields to a surface can be calculated based on the knowledge of the tangential fields on the surface [38], [45]. On the boundary, one needs the knowledge of tangential electric and magnetic fields or just one of them plus a boundary condition to short the other **(**J+PMC/M+PEC). Authors in [46] describe how this principle can be used for near-field to far-fields transformation using the knowledge of E and H. They also assume E and H are related by plane-wave relation. Using this assumption, only one component of electric/magnetic field needs to be measured which holds in

the far-field region of the DUT. In [19] electro-optic effect is used to measure tangential electric fields on cube surrounding the DUT. It is also assumed electric field (magnetic current) exists on the surface of the cube along with PEC to short the electric fields. After solving for electric currents on the cube, the far-field pattern can be calculated using both calculated electric current and measured magnetic currents.

Over all the aforementioned works, the DUT near-fields were acquired on a closed surface (like a closed cube) using traditional mechanical sweeping probes inside anechoic chambers. However, in the case of benchtop scanners because there is no movement for the measurement a single face, the positioning error is much less. The only movement is done between faces and so this positioning error becomes the largest source of error. Also, if each of the planar scan apertures are larger than the face of the resulting box then there is a level of redundancy in each scan, and we will have a "redundant-cube" (Fig. 3.1(b)). In the case of benchtop scanners this happens when the separation of the DUT from the scanner surface is less than the length of the scanner, when rotating the DUT. Redundant-cube can be defined as cube whose surface edge lengths are larger than the distance between individual surfaces. In this work, a new correction algorithm is proposed for the redundant cube setup that is the common case for the bench top scanners. It should be mentioned that the choice of SRM is sensitive to the setup, distance, and field type of the measurements. In [10], the J&M plus boundary (JMB) method was reported as the superior method in terms of electric field reconstruction when electric field measurement was used on a far sphere with a radius of 17.7λ. However, the presented assessment of magnetic measurement based SRM models in this chapter shows that the accuracy of JMB method is better for magnetic field reconstruction but worse for the electric field, in the region close to the fictitious surface.

In section 3.2, the problem description will be explained followed by the main SRM model

used in this chapter. In section 3.3 two additional SRM models will be defined for the sake of comparison followed by the MOM discretization details used in this work. In section 3.3 the linear error correction algorithm will be described. In section 3.4 several different test cases will be discussed in terms of 1) far-field transformation 2) error correction 3) field reconstruction 4) RFXpert 2 [1] scanner measurement. Finally, section 3.4 concludes the chapter.

3.2. SRM Theory

3.2.1. Problem description

In this work, it is assumed tangential magnetic fields are measured on multiple planar structures individually (6 sides of a redundant-cube). Still the method used in this chapter can be easily generalized to multiple arbitrary surface (spherical, cylindrical,). It is also not restricted to magnetic fields and can be easily generalized to electric field measurement as well. In the case of measurements done by benchtop scanners, the scanner is fixed and the DUT rotates. For simplicity, the DUT is assumed to be virtually fixed and located at the origin of its coordinate system in Fig. 3.2(b). For the sake of a first order correction of measurement errors, it is assumed the measured fields on a side might be off by a certain amplitude and phase with respect to the other ones, i.e,

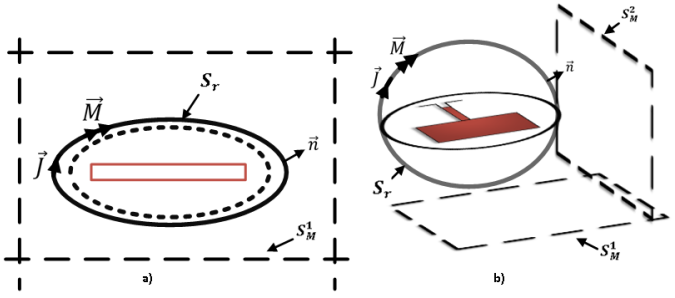

Fig. 3.2. a) Multiple planar measurements a) Multiple planar measurement equivalent problem, b) Equivalent Setup.

$$\boldsymbol{H}_m^i = (1 + \delta_i)\boldsymbol{H}_r^i,\ \delta_i \in C \tag{61}$$

here $\boldsymbol{H}_m^i$ is the tangential measured fields on the i^{th} measurement, $\boldsymbol{H}_r$ is the tangential magnetic field radiated by the DUT and δ_i is the i^{th} complex error factor which applies to all points of a face. Since δ_i is a complex number it can introduce both amplitude and phase errors. The goal of the algorithm is to 1) find the full-sphere far-field radiation pattern of the DUT and 2) reconstruct fields at arbitrary planes/locations outside the fictitious surface for diagnosis purposes.

3.2.2. Main Equivalent Problem

As depicted in Fig. 3.2, the equivalent problem can be described as a complete set of fictitious electrical currents ($\boldsymbol{J}_r$) radiating in free-space. The currents should radiate the same fields as the measured ones on the measurement planes ($\boldsymbol{S}_M^i$). Since there is no boundary condition present in the system, electric and magnetic fields can be calculated using the free-space radiation equations assuming $e^{i\omega t}$ time dependence.

$$\boldsymbol{E}(\boldsymbol{r}) = -\eta_0 \mathbf{L}(\boldsymbol{J};\boldsymbol{r}) + \mathbf{K}(\boldsymbol{M};\boldsymbol{r}) \tag{62}$$
$$\boldsymbol{H}(\boldsymbol{r}) = -\frac{1}{\eta_0}\mathbf{L}(\boldsymbol{M};\boldsymbol{r}) - \mathbf{K}(\boldsymbol{J};\boldsymbol{r}) \tag{63}$$

where

$$\mathbf{L}(\boldsymbol{J};\boldsymbol{r}) = jk_0 \int_{r'} [\boldsymbol{J}(\boldsymbol{r}') + \frac{1}{k_0^2}\nabla\nabla'_s.\boldsymbol{J}(\boldsymbol{r}')]g(\boldsymbol{r},\boldsymbol{r}')ds' \tag{64}$$
$$\mathbf{K}(\boldsymbol{M};\boldsymbol{r}) = \int_{r'} \boldsymbol{M}(\boldsymbol{r}') \times \nabla g(\boldsymbol{r},\boldsymbol{r}')ds' \tag{65}$$
$$g(r,r') = \frac{e^{-jk_0|r-r'|}}{4\pi|\boldsymbol{r}-\boldsymbol{r}'|} \tag{66}$$

where $\eta_0 = \sqrt{\frac{\mu_0}{\epsilon_0}}$, $k_0 = \sqrt{\mu_0 \times \epsilon_0}$ and ∇'_s is the surface divergence factor.

The system of integral equation the relating sources to the measured fields is as follows:

$$\begin{cases} -\boldsymbol{n} \times \boldsymbol{K}(\boldsymbol{J_r}; \boldsymbol{r}_{m1}) = \boldsymbol{n} \times (1 + \delta_1)\boldsymbol{H}_r^1 \\ -\boldsymbol{n} \times \boldsymbol{K}(\boldsymbol{J_r}; \boldsymbol{r}_{m2}) = \boldsymbol{n} \times (1 + \delta_2)\boldsymbol{H}_r^2 \\ \quad \ldots \end{cases} \quad (67)$$

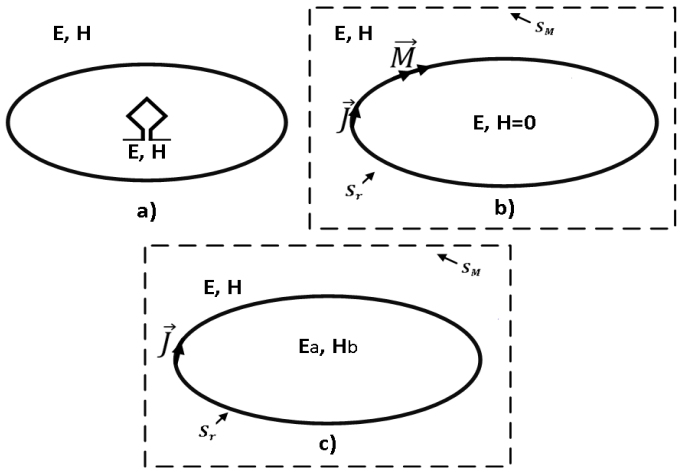

Fig. 3.3. Equivalent problems a) original problem, b) zero-inside, c) some inside.

In the last step, the far-field radiation pattern can be calculated using well known far-field integrals [38], [45]. The reconstructed fields at the desired locations can also be calculated using (62-63). This basic way of field reconstruction significantly simplifies the problem as there is no need to 1) include two types of current and 2) worry about fields being zero inside the fictitious surface. According to the field equivalence theorem we know that, given two sets of electromagnetic fields (a, b) and a closed surface, we can construct a new setup whose fields match *b* inside the surface and *a* outside. Provided that the currents on the surface are calculated using

$$\boldsymbol{J} = \boldsymbol{n} \times (\boldsymbol{H}^a - \boldsymbol{H}^b),\ \boldsymbol{M} = -\boldsymbol{n} \times (\boldsymbol{E}^a - \boldsymbol{E}^b) \tag{68}$$

Fig. 3.3. depicts three equivalent scenarios.

Fig. 3.3. (a) shows the original scenario where the antenna is radiating in free space.

Fig. 3.3. (b) has been traditionally used for field reconstruction [8], [9]. As it can be seen in the figure, for this assumption it is crucial that the fields go to zero inside the fictitious layer. In this work the model in Fig. 3.3(c), which was originally introduced in [9], is applied. Since all the models reconstruct the same fields on the closed measurement surface, according to the uniqueness theorem they radiate the same fields outside the fictitious surface. But the currents on the fictitious layer and the fields inside it are different among different models. Later in the results section it will be seen how, by using (62-63), it can be verified that the reconstructed fields (outside the surface) are not dependent on the type of model being used. That being said, this chapter shows that generally it is most efficient to use the simplest model where there is only 1 type of the source on the surface and there exists no boundary condition inside it. Before describing the discretization and solving methods, it is worth mentioning two other popular SRM models used in [8], [9] for the sake of comparison.

3.2.3. Additional SRM Models (for comparison only)

The main SRM model introduced in the previous section (3.2.2.) will be compared with the two major SRM models in the literature. They use both electric and magnetic currents on the fictitious surface. As depicted in Fig. 3.2(a) the difference in the models is that one has no boundary conditions inside the fictitious surface and the second one uses an extra boundary

condition inside the fictitious surface. It forces the fields inside the fictitious layer to go to zero which in turn improves the accuracy of the reconstructed currents [9]. Although the reconstructed currents are considered more accurate the radiated fields will be the same.

Model 1 (J&M No boundary condition)

The system of the integral equations for the first model is as follows:

$$\begin{cases} \boldsymbol{n} \times (-\frac{\mathbf{1}}{\eta_0} \boldsymbol{L}(\boldsymbol{M_r}; \boldsymbol{r}_{m1}) - \boldsymbol{K}(\boldsymbol{J_r}; \boldsymbol{r}_{m1})) = \boldsymbol{n} \times \boldsymbol{H}_r^1 \\ \boldsymbol{n} \times (-\frac{\mathbf{1}}{\eta_0} \boldsymbol{L}(\boldsymbol{M_r}; \boldsymbol{r}_{m2}) - \boldsymbol{K}(\boldsymbol{J_r}; \boldsymbol{r}_{m2})) = \boldsymbol{n} \times \boldsymbol{H}_r^2 \\ \dots \end{cases} \tag{69}$$

where $\boldsymbol{J_r}, \boldsymbol{M_r}$ are unknowns to be found. Note that the major difference between this model and the proposed model is that the equations of (67) are not dependent on M_r.

Model 2 (J&M + Love boundary condition)

In the second SRM method, an additional boundary condition is used to improve accuracy. The problems in Fig. 3.3(a) is equivalent to Fig. 3.3(b) provided that [38],

$$\boldsymbol{M} = -\boldsymbol{n} \times \boldsymbol{E}, \ \boldsymbol{J} = \boldsymbol{n} \times \boldsymbol{H}. \tag{70}$$

This way, the reconstructed currents can be interpreted as the constructed fields. Equation (70) holds only if the fields inside the fictitious surface are zero. In the previous SRM model (J&M no boundary condition), this condition was not explicitly forced, so (70) does not necessarily hold. To solve this problem one can force zero tangential fields on the fictitious surface go to zero in which case, an integral equation of type II must be dealt with. That will degrade the accuracy of the problem so to avoid this issue, the jump condition can be used [9], [37].

Using the jump condition, the new boundary condition is applied immediately inside (a

mesh element away) the fictitious surface. As a result, the system of boundary conditions for this problem will be

$$\begin{cases} \boldsymbol{n} \times (-\frac{\mathbf{1}}{\eta_0} \boldsymbol{L}(\boldsymbol{M_r}; \boldsymbol{r}_{m1}) - \boldsymbol{K}(\boldsymbol{J_r}; \boldsymbol{r}_{m1})) = \boldsymbol{n} \times \boldsymbol{H}_r^1 \\ \boldsymbol{n} \times (-\frac{\mathbf{1}}{\eta_0} \boldsymbol{L}(\boldsymbol{M_r}; \boldsymbol{r}_{m2}) - \boldsymbol{K}(\boldsymbol{J_r}; \boldsymbol{r}_{m2})) = \boldsymbol{n} \times \boldsymbol{H}_r^2 \\ \dots \\ \lim\limits_{r \to S_r -} n \times (-\eta_0 \mathbf{L}(\boldsymbol{J_r}; \boldsymbol{r}_b) + \mathbf{K}(\boldsymbol{M_r}; \boldsymbol{r}_b) = \mathbf{0} \end{cases} \tag{71}$$

3.2.4. MOM discretization

As depicted in Fig. 3.2, a surface of fictitious currents encloses the major radiator and parasitic elements present in the setup. The surface is discretized using triangular meshes. The size of the meshes should be fine enough so they form a complete set for the reconstructed currents. Each mesh edge presented on the surface defines a RWG basis function used to discretize both the electric and magnetic currents [25], [26], [39], [54]. RWG basis form a complete set of basis functions in terms of both current and charge ([40]) which guarantee the continuity of normal currents on the edges. This feature makes this type of basis function realistic because the current distribution on the fictitious surface is smooth as is always found in the free-space fields (current) distribution. It is also a computationally efficient choice using code that does not have to worry about line charges on the mesh edges. The electric and magnetic currents are discretized as follows

$$\boldsymbol{J}_{S_r}(\boldsymbol{r}') = \sum_{e(i) \in S_r} C_i \boldsymbol{f}_i(\boldsymbol{r}'), \; \boldsymbol{M}_{Sr}(\boldsymbol{r}') = \eta_0 \sum_{e(i) \in S_r} C_i \boldsymbol{f}_i(\boldsymbol{r}') \tag{72}$$

where $\boldsymbol{f}_i(\boldsymbol{r}')$ is RWG basis function distribution [39] and η_0 is a normalization factor to have a balanced interaction matrix [9], [26]. This normalization increases the overall well-posedness and accuracy of the discretized problem. The main integral equation defined in section 3.2.2 and the first SRM model in Section 3.2.3 do not involve boundary conditions whereas the

second model described in section 3.2.3 involves a zero-field boundary condition. This boundary condition (71) is a limit of a boundary conditions. Authors in [9] suggested it should be applied on a surface which is a mesh-element inside the fictitious surface Fig. 3.2(a). The authors also chose not to apply element-wide testing the fields and used point-matching at the center of testing triangles. In this work this same approach is followed except that the fields are element-size tested on the boundary conditions rather than point-matching. Using both point matching (at measure points) and RWG testing (at boundary conditions) has been described in [51]. Regarding the numerical integrations, a combination of singularity extraction and adaptive quadrature has been used [25]. First, the singular part of the integral is analytically [25], [42], [44] calculated and then the rest is left to a 6-point adaptive quadrature [25], [41]. The final matrix for the main SRM will be as follows

$$\begin{bmatrix} \boldsymbol{K}_{r,m1} \\ \boldsymbol{K}_{r,m2} \\ \dots \end{bmatrix} [C_r] = \begin{bmatrix} (1+\delta_1)H_{m1} \\ (1+\delta_2)H_{m2} \\ \dots \end{bmatrix} \tag{73}$$

In regularization step, both direct and in-direct methods can be used. For the most part of this work Tikhonov regularization method has been used [27], but it has been compared to least square (LSQR) method as a comparison of direct versus indirect methods comparison.

3.3. Linear Error Correction

During a 6-sided measurement scan, amplitude and phase error might happen between individual sides. It would be nice to be able to correct for the kind of error that might happen consistently for individual scans. This type of error can originate from instrument error such as amplitude and phase error in the signal generator or can be caused by cable response change due to bending or positioning error. It can also be generated from radiator's input impedance change

due to different near-by reflections on different sides. In this work, as indicated in (61), we assume the errors are due to linear measurement error, but this approach can be generalized to any linear error and constitutes a first order correction for non-linear errors. To find correction factors (δ_i) in (71), a successive approximation scheme will be used. In the first iteration, all δ_i are assumed to be zero. As such the matrix system will be regularized and first approximation for the problem is found (C_r^0). Due to the error between individual scans, the norm of the error, there is minimum for the reconstruction's error norm.

$$norm(e^0) = ||\boldsymbol{Z} \times \boldsymbol{C}_r^0 - \boldsymbol{b}^0|| = \begin{bmatrix} \boldsymbol{e}_1^0 \\ \boldsymbol{e}_2^0 \\ \dots \end{bmatrix} \tag{74}$$

where $\boldsymbol{Z}=\begin{bmatrix} \boldsymbol{K}_{r,m1} \\ \boldsymbol{K}_{r,m2} \\ \dots \end{bmatrix}$ and $b^0 = \begin{bmatrix} \boldsymbol{b}_1^0(H_{m1}) \\ \boldsymbol{b}_2^0(H_{m2}) \\ \dots \end{bmatrix}$.

At this step, the first approximation for the norm of the system can be calculated. The complex values of the δ are chosen to minimize the norm of the system ($\|e^0\|$). Since the norm in (74) is a norm-2, the problem of minimizing is a quadratic problem. Therefore the δ_i can be found by having

$$\frac{\partial ||\boldsymbol{e}^0(\delta)||}{\partial \delta_i} = 0 \tag{75}$$

$$\mathrm{e}^0(\delta) = ||\boldsymbol{Z} \times C_r^0 - (1+\delta)b^0|| = \begin{bmatrix} \boldsymbol{e}_1^0 - \delta_1 \boldsymbol{b}_1^0 \\ \boldsymbol{e}_2^0 - \delta_2 \boldsymbol{b}_2^0 \\ \dots \end{bmatrix} \tag{76}$$

After applying (39), using (49) we can find

$$\delta_i = \frac{\boldsymbol{b}_i^{0^*}.\boldsymbol{e}_i^0}{\boldsymbol{b}_i^{0^*}.\boldsymbol{b}_i^0}, \tag{77}$$

where e_i and b_i are i^{th} sub-vectors of vectors e^0 and b^0 corresponding to the i^{th} measurement. The * sign represents conjugate transpose operator.

Once the ε_js are calculated, the right-hand side of the equation can be updated as

$$\boldsymbol{b}_j^{i+1} = (1 + \delta_j^i \boldsymbol{b}_j^i) \tag{78}$$

After the right-hand side is calculated, the next iteration begins. The cycle continues after a convergence criterion is met. The convergence criteria can be defined on the norm change of the right-hand side.

$$error = \frac{||\boldsymbol{b}^i - \boldsymbol{b}^{i-1}||}{||\boldsymbol{b}^i||} \tag{79}$$

The steps of the algorithm can be defined as follows:

1. The main interaction matrix is built and the SVD is calculated (if using direct method),
2. First estimation of the back-projected currents is calculated (on the fictitious layer) using the right-hand side assuming $\boldsymbol{\delta_i}$=0,
3. $\boldsymbol{\delta_i}$ are calculated using (77),
4. Right-hand side is updated using (78)
5. Convergence criteria us checked using (79),
6. If not converged go back to step 2.

3.4. Results

3.4.1. Overview

To validate the proposed methods 4 measurement scenarios will be considered and discussed in four parts. In the first part, two test cases will address the comparison of the SRMs error-less results in terms of near-field to far-field transformation accuracy by comparison to those provided by HFSS full-wave simulator. The two test antennas are a three-element Yagi array and a 45-degree tilted half wavelength dipole. In the second part the error correction algorithm will be discussed using the 45-degree half wavelength dipole in HFSS full-wave simulator. In the third part, the SRMs will be compared in terms of near-field reconstruction accuracy using the 45-degree tilted half wavelength dipole simulated in side HFSS and an analytical infinitesimal dipole. Finally, in the last part, a CP-patch antenna will be measured using the RFX2 *(EMSCAN)* benchtop scanner and the far-field results will be compared to that of the chamber ones. Moreover, the main reason behind antenna choices are their practicality for EMSCAN type of scanners.

3.4.2. Far-field Tests

3.4.2.1.Three-element Yagi Array

In the first test-case, a three-element Yagi dipole array is discussed at 2.4 GHz |

(

Fig. 3.4(a)). The array is simulated within a full-wave simulator and calculated magnetic near-fields are extracted to be used as synthetic data by SRM algorithms (

Fig. 3.4(b)). The near-field measurement's aperture size is 18×18cm^2, aperture to DUT separation is 8cm and the sample spacing is 2 cm. The three dipoles' lengths are 6.021 cm, 5.621 cm and 5.296 cm. The dipole spacing and diameters are 2.498 cm and 0.10 cm, respectively. The fictitious surface to reconstruct currents is an ellipsoid with semi-axis (1.5cm, 4.5cm, 4.5cm) in x, y and z directions. The transformed far-field results of the array can be found in

Fig. 3.4(c). The reason $E_\phi$component of the pattern is missing from the 2D cuts is that it is comparably negligible. As it can be seen, all SRM methods are accurate in terms of the transformed far-field patterns. Moreover, in Table IV, the directivity and radiated power are reported to be extremely accurate. It is worth to have a look at the matrix sizes and normalized calculation time to have an idea about computational resources the models require. Normalized calculation time is calculated assuming O(m×n) distribution where m and n are the number of rows and the number of columns of the matrix.

Table IV

RESULTS FOR THREE-ELEMENT YAGI ARRAY

Method	Radiated Power (dbm)	Directivity (dbi)	Matrix Size	Normalized calculation time
HFSS	9.2	8.99	-	-
J (proposed)	9.18	8.89	1200×3528	1
J&M	9.19	8.91	1200×7056	2

J&M*BC	9.17	8.87	4728×7056	7.88

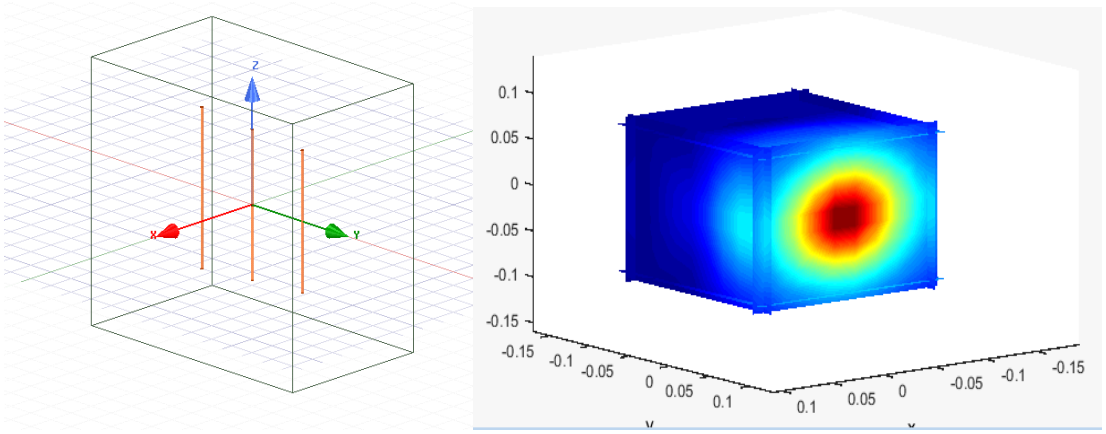

(a) (b)

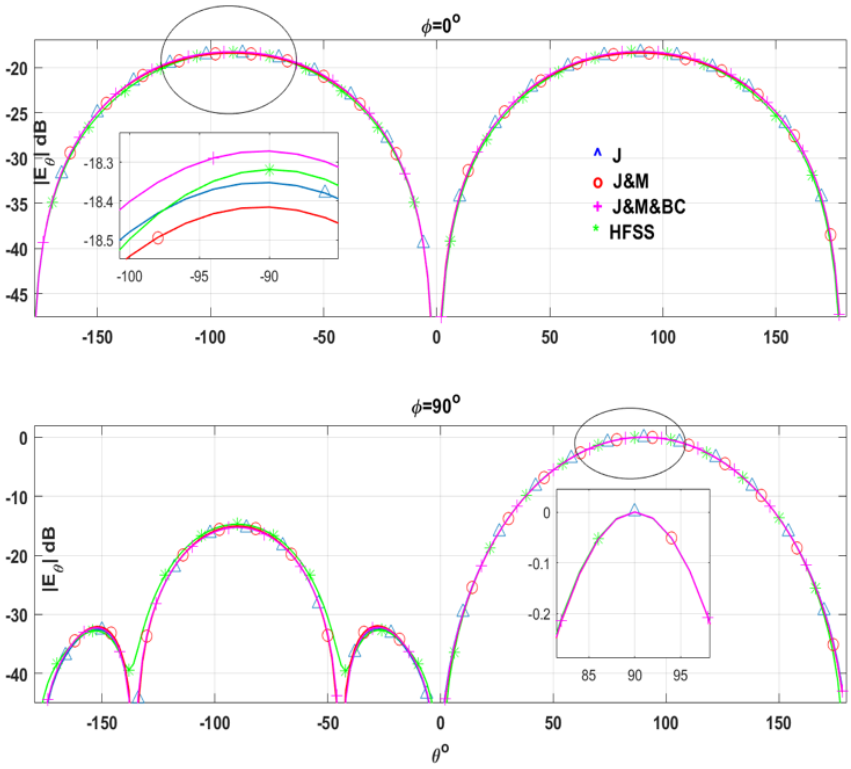

(c)

Fig. 3.4. 3-elements Yagi Array, a) Setup b) Extracted Near-Fields (tangential magnetic fields complex magnitude) c) Normalized 2D Far-Field radiation pattern cuts

Based on data in Table IV, it is obvious that accuracy of the models used is in the same order, but the computational resources they need can be very different.

To consider robustness of the algorithm, here the effect of Gaussian noise has been studied. Independent random amplitude and phase noise has been injected with normal distribution and standard deviation of 10% amplitude and 10 degrees phase. The total error ($|\boldsymbol{H}_{noisy}-\boldsymbol{H}|/|\boldsymbol{H}|$) histogram can be found in Fig. 3.5(b) which shows 10%-15% error has been injected to 20% of

the dataset. The Noisy data has been used for NF to FF transformation using both direct (Tikhonov) and indirect (LSQR) methods. The results of the comparison can be found in Fig. 3.5(a) that shows negligible impact due to the injected noise.

3.4.2.2. 45-degree tilted half wavelength dipole

The second test case, a 45-degree tilted dipole at 2.4 GHz will be discussed in this section. The dipole is 5.51 cm long with diameter of 0.18 cm. The measurement window is 40×40 cm^2 with sampling distance of 1cm. The aperture to DUT separation is 12.5 cm. This dipole is simulated to provide NF data for a 6-sided scan representing a RFX2 probe array. Fig. 3.6(b) shows the measured total tangential magnetic field while the calculated far-field radiation pattern of the antenna can be found in Fig. 3.6(c).

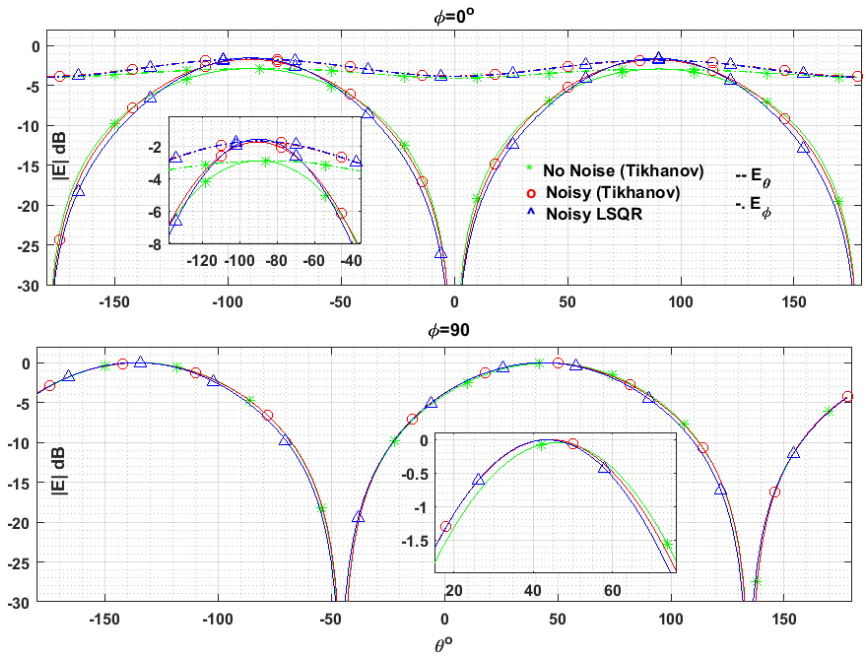

(a)

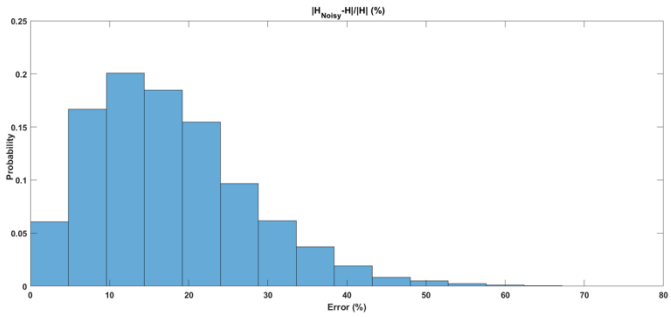

(b)

Fig. 3.5. 3-elements Yagi Array, Normalized 2D Far-Field radiation pattern cuts from noisy data, b) Error Histogram

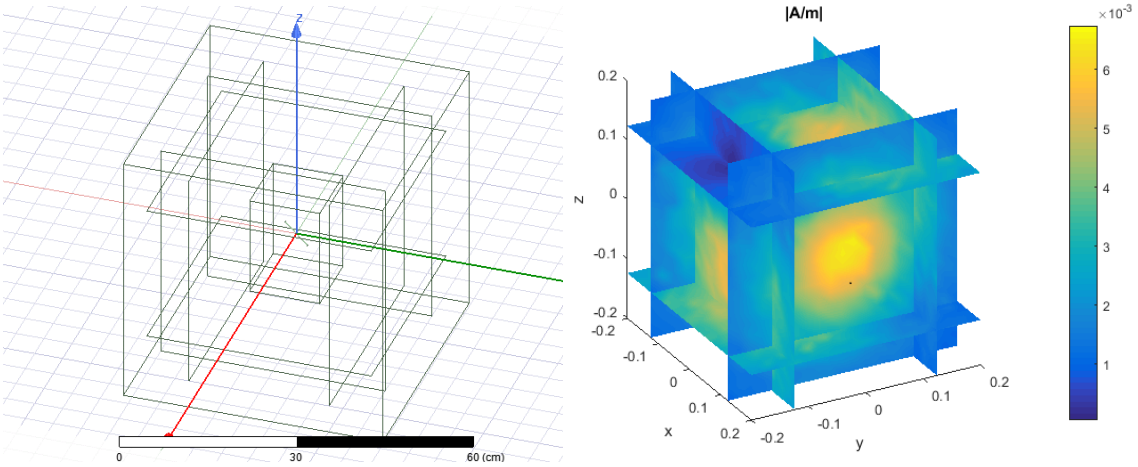

(a) (b)

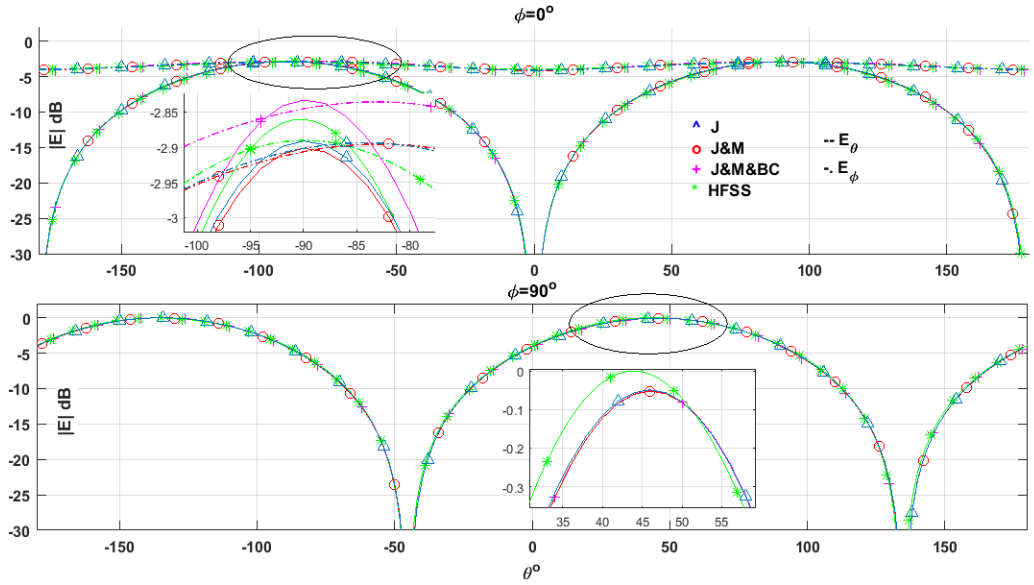

(c)

Fig. 3.6. 45-degrees tilted half wavelength dipole, a) Setup b) synthetic measured data obtained from a full-wave simulation, Near-Fields (tangential magnetic fields complex magnitude) c) 2D normalized far-field radiation pattern cuts.

TABLE V

RESULTS FOR 45-DEGREE TILTED HALF WAVELENGTH DIPOLE

Method	Radiated Power (dbm)	Directivity (dbi)	Matrix Size	Normalized calculation time
HFSS	-0.13	2.23	-	-
J (proposed)	-0.15	2.25	5292x3528	1
J&M	-0.15	2.26	5292x7056	2
J&M*BC	-0.16	2.29	8820x7056	3.33

As it is illustrated in the graphs, once again all the models are very accurate in terms of near-field to far-field transformation. The other antenna parameters along with matrix sizes can be found in Table V. Again, looking into the calculated values, it is seen, all the models are consistently accurate in terms of near-field to far-field transformation and that the J-proposed method is the fastest. As a general comment, the accuracy of FF reconstruction is better for 6-sided transformation vs the single sided one. The main reason is the algorithm has access to more information which is radiation of the AUT over all directions.

3.4.3. Linear Error Correction

To study the effectiveness of the error correction algorithm between the individual scans the 45-degree tilted half wavelength dipole of the previous section is reused. This antenna is a

typical omnidirectional antenna, and that is the main reason of choosing such test-case. Thus, the linear error between individual scans will be more troublesome. For instance, two error cases are studied here which are instances of the error described in (61). In the first one, individual scans are multiplied by random injected error factors $-0.25 < Real(\delta_i), Imag(\delta_i) < 0.25$. The error terms for the 6 faces of case 1 are (-0.06+0.14j, -0.22-0.21 j, -0.14+0.07 j, 0.10+0.06 j, -0.02+0.02 j, -0.09+0.11 j).). In second case random error factors of $-0.45 < Real(\delta_i), Imag(\delta_i) < 0.45$ are injected along with random injected rotational errors between -5 and +5 degrees. The error terms for the 6 faces of case 2 are (-0.37-0.24j, 0.37-0.31j, 0.29+0.03j, 0.44-0.37j, -0.05-0.35j, 0.41-0.44j). Also, the injected rotational error angles are 2.5, 2.43, -3.2, 1.5, -4.6 and 2 degrees. First, the far-fields are calculated using the proposed method with the noisy data. Then the correction algorithm described in part 3.3 is used to correct for the injected error.

Fig. 3.7(a) shows the radiation pattern for the noisy data, the corrected ones and the ideal patterns calculated within a full-wave simulator. As it can be seen in the figure, the algorithm has corrected the radiation pattern very accurately. An interesting fact in the Fig. 3.7(b) is that as the iterations increase, not only the solution norm decreases, but also the problem shows better convergence both for the direct Tikhonov's L curve and iterative LSQR methods. Moreover, Table VI, shows the antenna parameters for the noisy, corrected and the ideal solution. The directivity has been fully corrected and radiated power has been corrected to some extent for low the noise case. The reason radiated power has not been fully corrected can be found in Fig. 3.7(c) which shows correction ratios before and after corrections. The correction algorithm adjusts the amplitude and phase of each of the 6 faces so that they are all in a similar error state relative to the AUT. However, it cannot find the absolute error relative to expected position relative to the AUT.

The reduced relative error provides for accurate relative measurements like directivity but the remaining absolute error means absolute terms like Radiated Power can still have significant error. This error could be reduced by providing extra information as which face was measured with less errors and forcing relative error corrections to be referenced to this single face.

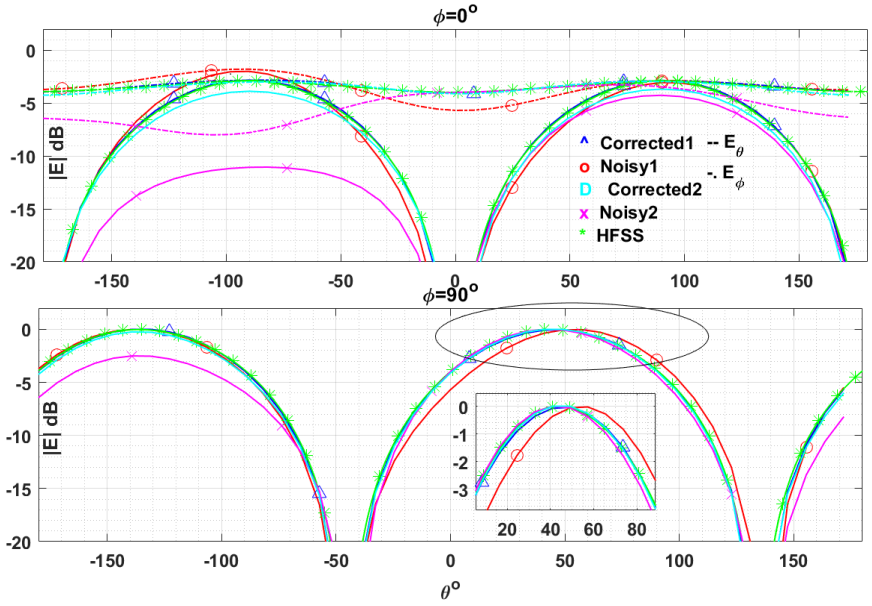

(a)

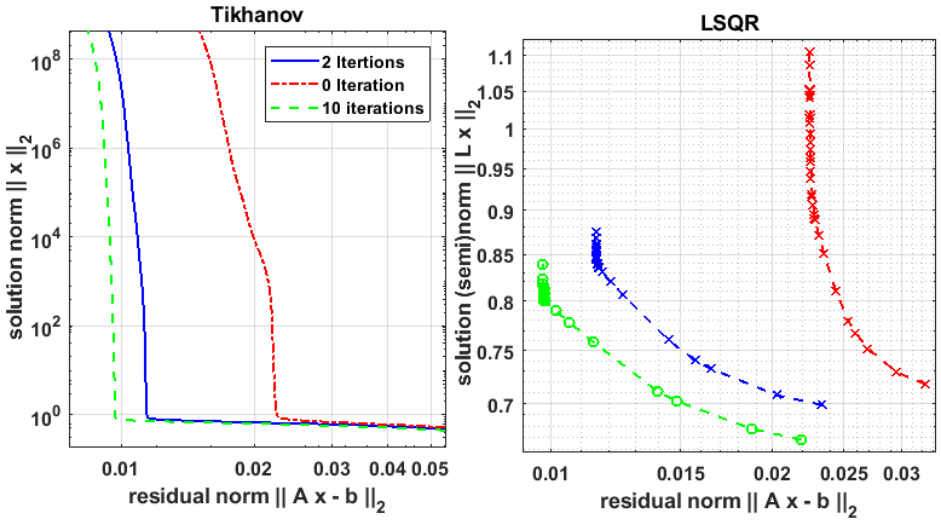

(b)

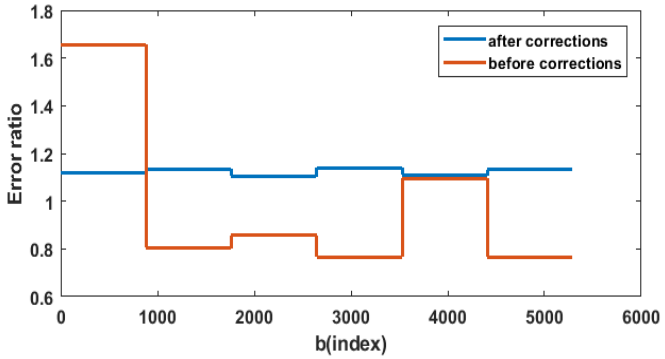

(c)

Fig. 3.7. Noisy field's MOM reconstruction a) far-field radiation pattern b) convergence L-curves for the first test-case c) right-hand side error's absolute value before and after corrections for second Noisy case.

Table VI

RESULTS FOR NOISY, CORRECTED AND THE IDEAL SOLUTION

Method	Radiated Power (dbm)	Directivity (dbi)	Iteration	Max Error Bound
Simulation	-0.13	2.23	-	-
Noisy 1	0.33	3.03	0	-
Corrected 1	-0.25	2.25	10	0.25
Noisy 2	-2.7	5.17	0	-
Corrected 2	-1.59	2.26	15	0.45

3.4.4. Field Reconstruction

The other major applications of SRMs are near-field reconstructions. To compare the accuracy and computational efficiency of different SRMs the half-wave dipole used in the previous sections is simulated using MOM full-wave solver. First, magnetic fields (extracted out of the full-wave simulation at measurement planes) are back-projected into equivalent currents consisting of

i) J,

ii) M,

iii) J&M,

iv) J&M+boundary condition.

Then, reconstructed fields are calculated using (62). To study the effect of SNR, the comparison is done using two SNR values of 40 dB and 20 dB. For this purposes, white noise was added to the original synthetic data acquired from simulation. The original reconstruction error (before noise addition) at measurement surface is -177 dB but drops to about -40 dB and -20 dB in the mentioned SNR, respectively.

The fictitious surface used for the back-projections is an ellipsoid with semi-axis $(0.12\,\lambda, 0.36\,\lambda, 0.36\,\lambda)$ for $\lambda = 12.5\,cm$, as shown in Fig. 3.8 (a). The results can be found in Fig. 3.8 where the magnitude of the reconstructed fields along a line normal to the dipole (the x axis of Fig. 3.8(a)) is plotted versus distance normalized to wavelength. The figure illustrates that as long as the reconstruction surface is complete (able to reconstruct measured fields),

reconstruction accuracy at r > 0.5λ is fairly consistent regardless of the type of current being used. The major difference between the models is the current on the fictitious surface and the fields inside the fictitious surface which are not important in the pattern extraction. In Fig. 3.8(b) is can be seen all SRMs except JMB, the fields have *not* gone to zero inside the fictitious surface. Therefore, interpreting the reconstructed currents as the reconstructed fields using equation (70) will introduce an error. In the region close to the fictitious surface it can be seen that the accuracy of JMB method is the best for magnetic field but the worse for electric field reconstructions.

As a second test, analytical fields for an infinitesimal dipole ($a_x + a_y$ oriented at origin) are used for field reconstruction. Fields are sampled on a plane at 1 λ away from the dipole and then back-projected to an ellipsoid of electrical currents only. Then the electric and magnetic fields on a line normal to the dipole (the x axis) are reconstructed and compared with the analytical ones. The results of the reconstruction can be found in Fig. 3.9. It shows the accuracy of the proposed algorithm is very good when going back to 0.3λ from the dipole but begin to diverge at distances closer than this.

3.4.5. Measurements

To finalize the results part, a measurement test case will be studied. The circular polarized patch antenna's near-fields are measured using an array of magnetic probes (EMSCAN's RFX2 scanner) at 2.4 GHz. In the experimental setup, the antenna is located at the center of a cubic frame. The cube is then rotated, and its 6 sides are successively scanned one at a time. To make sure all the 6 scans are phase coherent, a power divider has been used to provide an external consistent phase reference to the scanner.

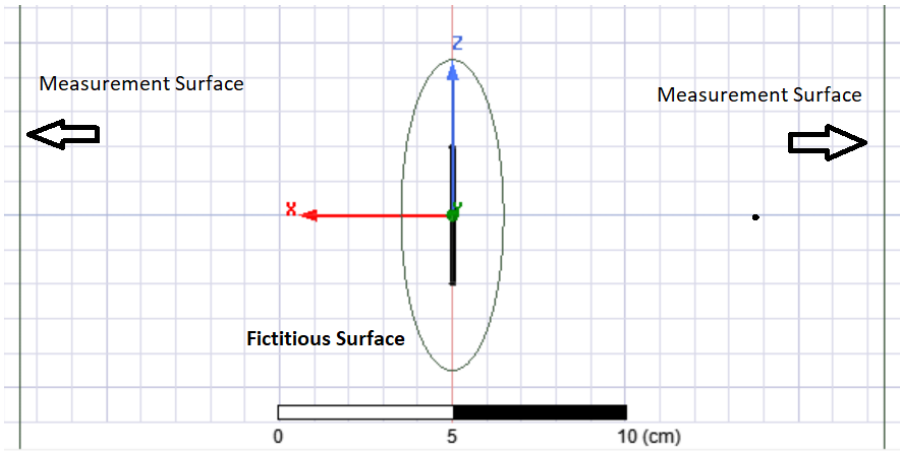
Measurement Surface
Measurement Surface
z
x
Fictitious Surface
0
5
10 (cm)

(a)

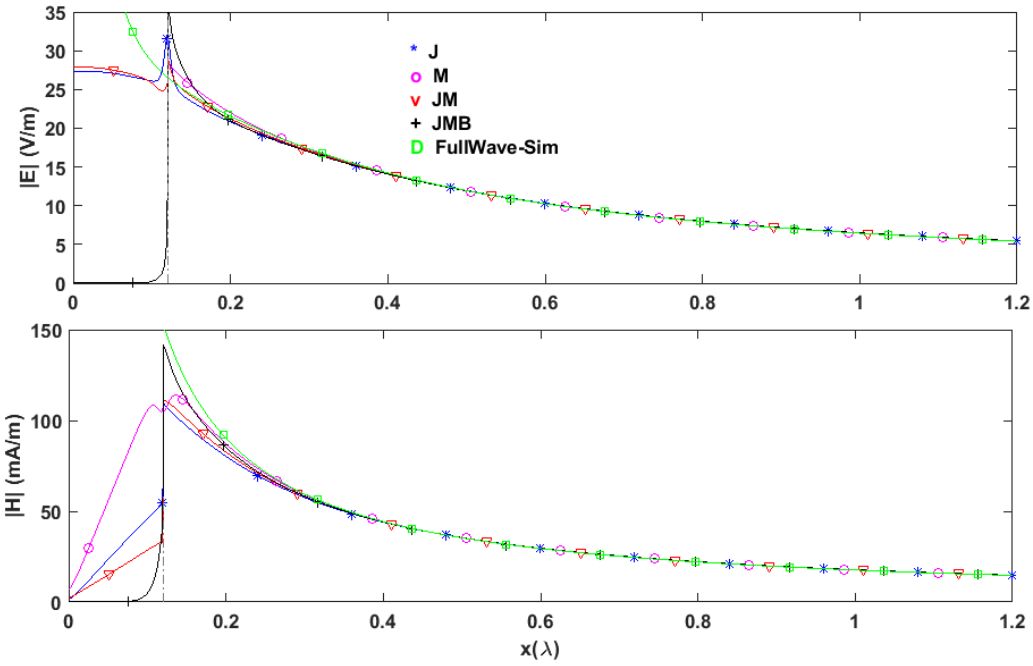
J
M
JM
JMB
FullWave-Sim
|E| (V/m)
|H| (mA/m)
x(λ)

(b)

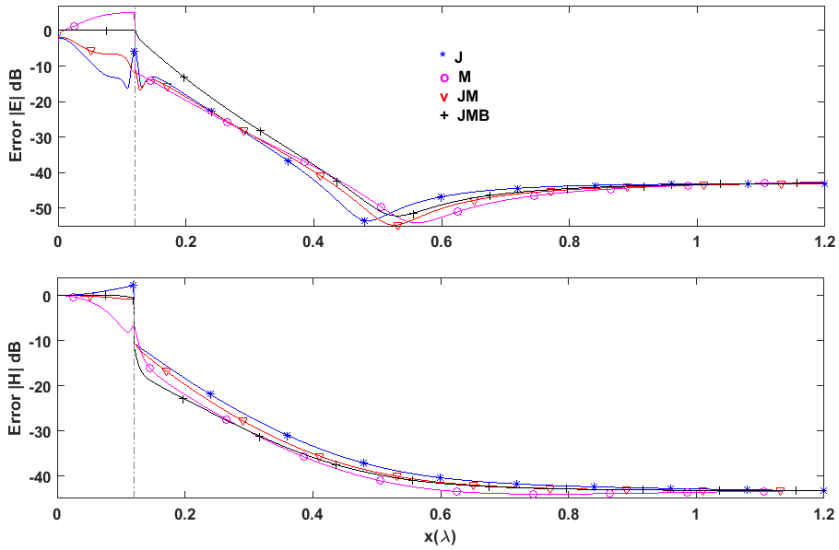

(c)

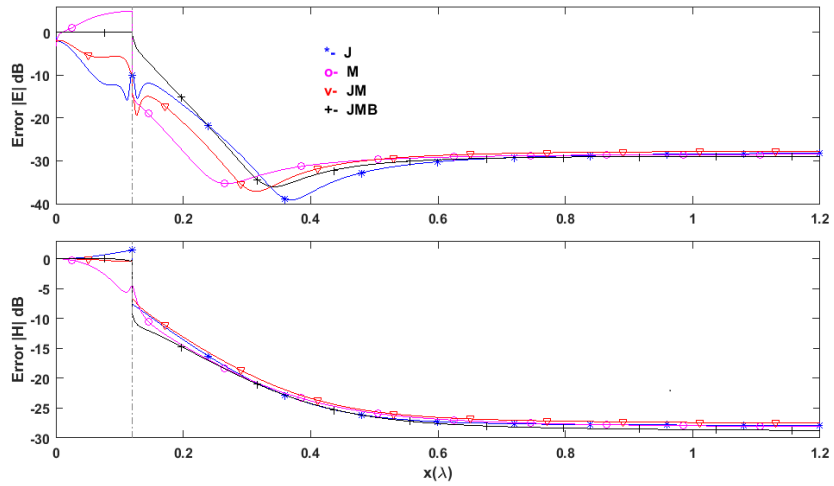

(d)

Fig. 3.8. Half-wave dipole's current and field reconstruction a) setup, b) back-projected currents on the x axis (SNR=40dB), c) back-projection error on x-axis (SNR=40dB), d) back-projection error on x-axis (SNR=20dB)

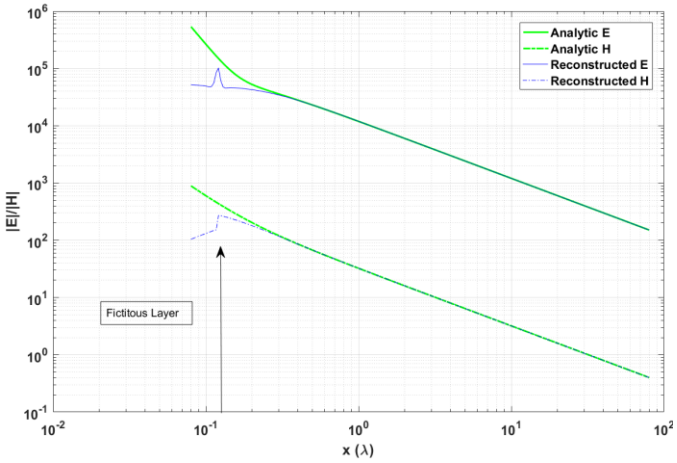

Fig. 3.9. Reconstructed fields for an analytical infinitesimal dipole

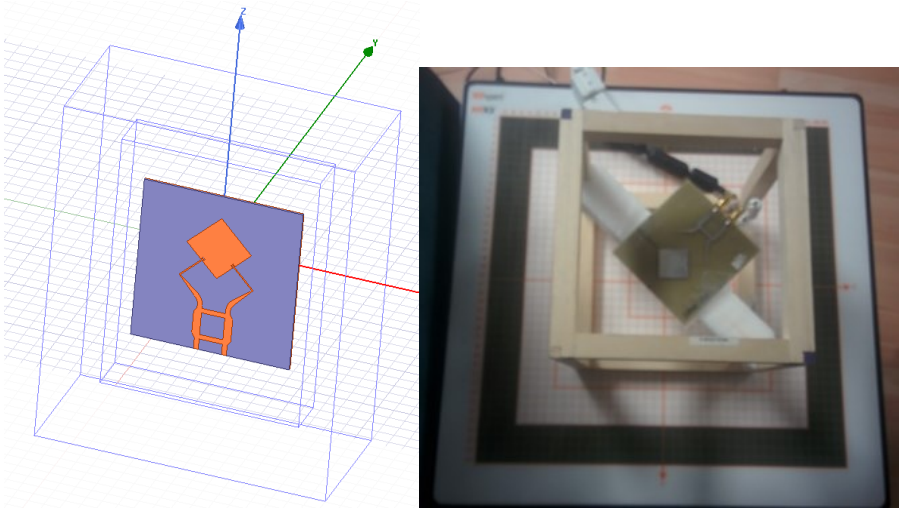

(a) (b)

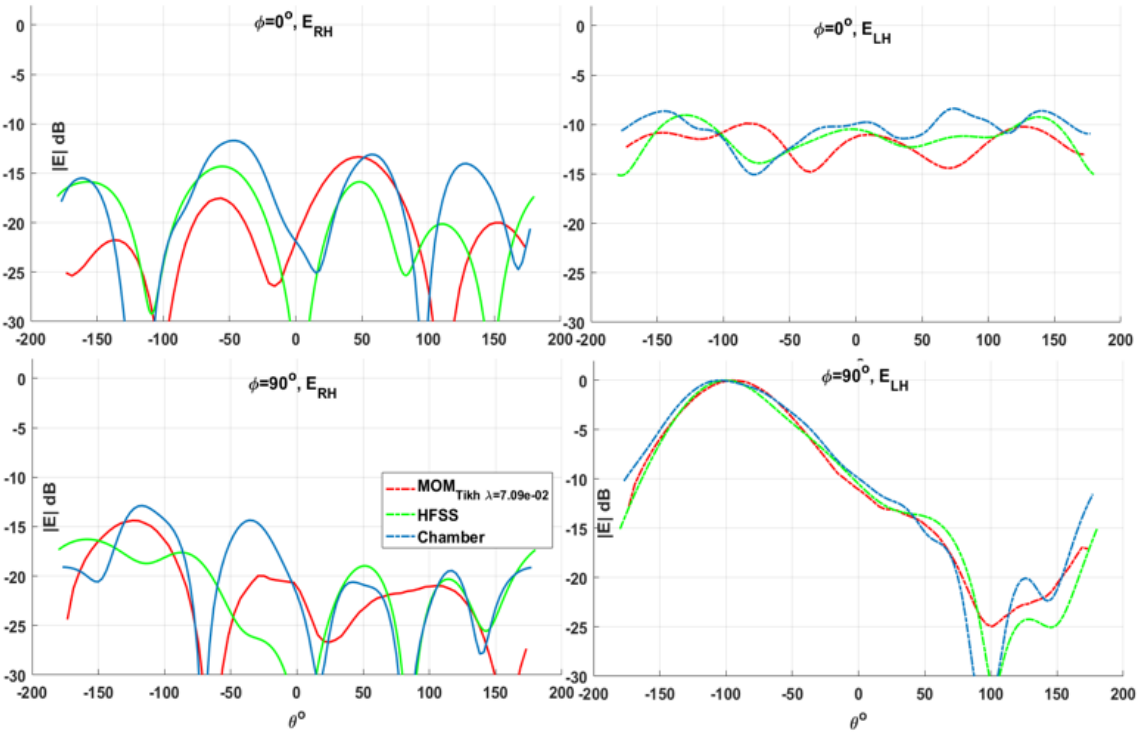

(c)

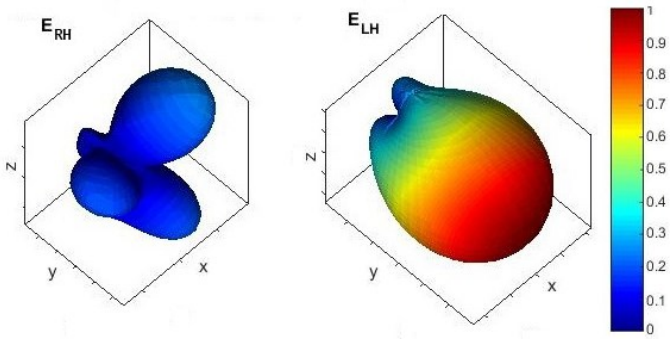

(d)

Fig. 3.10. LHCP patch antenna a) model b) measurement setup c) 2D normalized radiation pattern d) 3D radiation pattern (Normalised linear amplitude)

The scanner aperture is 40cmx40cm and sampling distance is 1cm. The semi-axis of the ellipsoid fictitious surface are (7 cm, 1.5 cm, 7.5 cm). The patch's model and the measurement setup can be found in Fig. 3.10(a) and Fig. 3.10(b). The measurement done on the RFX2 has ground plane effects from the scanner that are beyond the scope of this chapter. To minimize any impacts in these measurement results the choice of the setup were chosen to minimize loading and mutual reflections. Fig. 3.10(c) shows the result of near-field to far-field transformation. It also enables a comparison with radiation patterns measured in an anechoic chamber and those stemming from the simulation model. The measured directivity calculated using the proposed method, full-wave simulation and anechoic chamber are 7.3, 7.3 and 6.63 dbi, respectively. It can be seen that if the directivity has been calculated very accurately

3.5. Conclusion

In this work a method of near-field transformation has been proposed to correct the linear errors between individual scans as a common source of error in the multi planar measurements. A comprehensive study on SRM has been done subject to the magnetic measurements on redundant cube. The results demonstrate that all methods are consistently accurate in terms of near-field to far-field transformation. However, JMB is the superior magnetic field reconstruction method for the near-field reconstructions.

Chapter 4

Planar Green's Function based MoM Used in Absorber Effect Estimation

In this work, a method of moment (MoM) based algorithm is proposed to predict absorber effects due to the presence of an absorber on top of a device under test (DUT). To achieve this goal, first, radiated near-fields of the DUT is measured and back-projected to the equivalent reconstructed sources. In the second step, dyadic Green's function for planarly stratified media is used for field prediction. Reconstructed equivalent currents are discretized using triangular RWG basis functions which guarantee current continuity. The proposed algorithm, as well as accuracy of the dyadic Green's function, is validated using accurate full-wave simulations. The results of the field prediction will be valuable for choosing right absorbing material with desirable performance which complies with EMC/EMI standards.

4.1. Introduction

With the rapid advance in wireless technology and increasing demand for low power and compact circuits, Electromagnetic Interference (EMI) concerns are raised more than ever [55]. A common problem is noise coupling between unwanted emissions from digital ICs with analog circuitry. This in turn causes reduced receiver sensitivity and performance degradation [56], [57]. Many of the typical elements on mobile devise as CPUs, interconnects, displays, etc. produce noise

This work was technically and financially supported by EMSCAN Corporation under NSERC-AITF Industrial Research Chair program.

A. Kiaee, R.R. Alavi, R. Mirzavand, and P. Mousavi are with Departments of Mechanical Engineering, Electrical Engineering at the University of Alberta, Edmonton (e-mails: kiaee@ualberta.ca). A. Kiaee, R. Patton, and B. Alavikia are with EMSCAN Corporation Calgary, Alberta, Canada (Ruska.patton@emscan.com; babak.alavikia@emscan.com).

in the frequency range of RF circuitry [56], [58]. Debugging and mitigating these emissions is of more importance recently [56], [59], [60]. Regarding the diagnosis case, since printed circuit boards (PCB) have many details, it is usually very difficult to perform electromagnetic full-wave simulations on them. On the other hand, one can use electromagnetic inverse algorithms to reconstruct currents close to PCBs or radiated fields from it for diagnostic purposes. For that it is sufficient to measure near-fields radiated by DUT. Recently researchers have tried to use the inverse of the problem to diagnosis radiation issues [56], [57], [61], [62]. Authors in [56] used Method of Moments (MoM) and the reciprocity principle to reconstruct currents on the antenna ground-plane for EMI debugging purposes. In that work magnetic fields close to the device under test (DUT) are measured and back-projected to currents on the antenna ground plane, which are later used to calculate radio frequency interference. Knowing an estimation of near-fields and currents on DUTs can be useful at design time. Considering this can enable the design of analog circuitry with proper electromagnetic capability (EMC) [63]. When using MoM, one has several discretization choices as the type and basis function of currents on the fictitious surface, as well as the size and geometry of the surface. However it has been shown that the fields radiated by the DUT is consistent regardless of the choices of discretization parameters approximately after one wavelength away from the DUT [9], [10]. The former assumption is provided that the set of current on the fictitious surface form a complete set to describe near-fields of the DUT. One can increase accuracy of reconstructed fields close to DUT by measuring very near-fields radiated by it.

Regarding the emission mitigating case, electromagnetic absorbers have been a reliable solution for mitigating unwanted emissions and undesirable interferences [59], [60], [64]–[67]. Absorbers reflect, transmit and absorb electromagnetic power passed to them. Modeling and studying effects of absorbers for EMC/EMI applications is important. This knowledge is essential

for choosing proper absorbers for specific applications. Recent work shows it is essential to be able to analyze fields reflected and transmitted by absorbers when they are placed in the near-field region of electromagnetic sources [59], [60], [68], [69]. Researchers in [70] have used Schelkunoff's method to approximate fields and shielding effectiveness of a single layer planar absorber placed in near-field region of an electric dipole. Even though this method is fast, its accuracy is limited and degrades as the distance between the dipole and the absorber decreases. Researchers in [59] have also used full-wave solvers to accurately analyze the interaction of single layer planar absorbers with electric and magnetic dipoles in near-field. This method is very accurate but requires a full-wave solver and a lot of computational time.

This work uses dyadic Green's functions for planarly stratified media to accurately analyze electromagnetic fields reflected, transmitted and inside multi-layer planar absorbers. In addition to single layer absorbers described in previously discussed works, multi-layer absorbers have the advantage of very low reflection in a board frequency range [71]. Being able to analytically evaluate field propagations in this type of absorbers can be useful in applications demanding broad-band low reflection absorbers. This work also proposes a new algorithm to estimate reflected and transmitted fields radiated of DUT from the surface of a multi-layer planar absorber without knowing its structure details. In this method, near-fields of DUT (no absorber) is measured and back projected to a surface of fictitious currents using the free-space kernel. In the second step, reflected and transmitted fields by the absorber are calculated using dyadic Green function kernel.

The structure of this chapter is as follows: Section 4.2 describes calculation of dyadic Green function for multi-layer media. The Green function allows calculation of transverse electric or magnetic fields radiated by transversely oriented infinitesimal electric or magnetic dipoles. Section

4.3 describes source reconstruction model (SRM). In that section, it describes how measured magnetic fields in close vicinity of a DUT can be back-projected to equivalent sources. The equivalent sources are discretized using RWG basis functions and radiate the same fields as the measured ones. Section 4.4 describes the estimation model. This section describes how the dyadic Green function calculated in Section 4.2 and reconstructed sources in Section 4.3 can be used to estimate reflected and transmitted fields by a multi-layer absorber. Section 4.5 illustrates the results of the theory described in Sections 4.2 to 4.5. First the dyadic Green function is verified using full-wave simulations for both electric and magnetic dipoles. A source reconstruction and estimation model are described afterwards. Finally, Section 4.5 presents the final conclusions.

4.2. Dyadic green's function

Fig. 4.1. shows the stack-up for the problem of multi-layer planar absorbers being placed in near-field region of an electric or magnetic dipole. The dipole is placed in free-space in front of a stack of planar absorbers, and the goal of this section is to derive a dyadic Green function relating dipole moments to transverse field over all layers. Due to the type of MOM discretization described in Section 4.3, it is assumed the dipole orientation is transverse to the stack of absorbers a special case in Figure 4.1. Also, again due to type of discretization chosen in Section 4.3, it is assumed all observation points are above source points or $z - z' > 0$.

$$\boldsymbol{J}(\boldsymbol{r}') = Il\,\delta(\boldsymbol{r}' - \boldsymbol{r}_0')\boldsymbol{a}_J \tag{80}$$

$$\boldsymbol{M}(\boldsymbol{r}') = Il\,\delta(\boldsymbol{r}' - \boldsymbol{r}_0')\boldsymbol{a}_M \tag{81}$$

$$\boldsymbol{a}_J.\boldsymbol{a}_z = 0, \boldsymbol{a}_M.\boldsymbol{a}_z = 0 \tag{82}$$

Analysis of wave propagation in planarly stratified media basically relies on Sommerfeld integrals and transmission line theory [72]. Using Sommerfeld integrals, fields radiated by horizontal dipoles can be decomposed into TE and TM modes which are represented by z components of H and E fields respectively. Assuming e^{jwt} time dependence and by using Sommerfeld's identity, normal components of electric and magnetic fields for x-directed dipoles can be calculated as [72]:

$$E_z^J = -\frac{jIl}{8\pi\epsilon_0}\frac{x-x'}{\rho}\int dk_\rho\, k_\rho^2 H_1^2\left(k_\rho\,\rho\right) TL_{tm}(z-z') \tag{83}$$

$$H_z^J = -\frac{jIl}{8\pi}\frac{y-y'}{\rho}\int dk_\rho \frac{k_\rho^2}{k_z} H_1^2\left(k_\rho\,\rho\right) TL_{te}(z-z') \tag{84}$$

$$E_z^M = \frac{-jIl}{8\pi}\frac{y-y'}{\rho}\int dk_\rho \frac{k_\rho^2}{k_{1z}} H_1^2\left(k_\rho\right) TL_{tm}(z-z') \tag{85}$$

$$H_z^M = \frac{jIl}{8\pi\omega\mu_0}\int dk_\rho\, k_\rho^2 H_1^2\left(k_\rho\,\rho\right) TL_{te}(z-z') \tag{86}$$

where $H_1^2$is Hankel function of second kind and ρ is transverse distance between source and observation point. The extents of all the integrals is from minus infinity to plus infinity.

Normal components of E and H follow a similar trend for y-directed dipoles. For that, one just replaces x with y and y with -x. Once the normal components of electric and magnetic fields are calculated, they can be used to calculate transverse components [72].

$$\boldsymbol{E}_t\left(k_\rho,\boldsymbol{r}\right) = \frac{1}{k_\rho^2}\left[\nabla_s\frac{\partial E_z}{\partial z} + j\omega\mu\, a_z \times \nabla_s H_z\right] \tag{87}$$

$$\boldsymbol{H}_t\left(k_\rho,\boldsymbol{r}\right) = \frac{1}{k_\rho^2}\left[\nabla_s\frac{\partial H_z}{\partial z} - j\omega\mu\, a_z \times \nabla_s E_z\right] \tag{88}$$

Using (83-88) 8 dyads of the dyadic Green functions can be calculated. The Green functions relate transverse dipole moments to transverse electric or magnetic fields in planarly stratified media.

$$\boldsymbol{E}_t^J \text{ or } \boldsymbol{H}_t^J = \begin{bmatrix} G_{xx}^J & G_{xy}^J \\ G_{yx}^J & G_{yy}^J \end{bmatrix} \begin{bmatrix} J_x \\ J_y \end{bmatrix} \tag{89}$$

$$\boldsymbol{E}_t^M \text{ or } \boldsymbol{H}_t^M = \begin{bmatrix} G_{xx}^M & G_{xy}^M \\ G_{yx}^M & G_{yy}^M \end{bmatrix} \begin{bmatrix} M_x \\ M_y \end{bmatrix} \tag{90}$$

TL functions in (83-86) and eventually in dyads of (89-90) show the transmission line dependency and are dependent on the layer the observation point relies in. Assuming the observation point is in Layer N, the transmission line function part will be as follows:

$$TL_{te\backslash tm}(z) = A(e^{-jk_{z_N}z''} + \tilde{R}_{tm\backslash te}\, e^{jk_{z_N}(z''-2L_N)}) \tag{91}$$

where $z'' = z - z_0^N$, z_0^N is the starting height of the Nth layer. $\tilde{R}_{tm\backslash te}$ is total reflection coefficient between layers N and N+1 [72], and L_N is the length of the Nth layer.

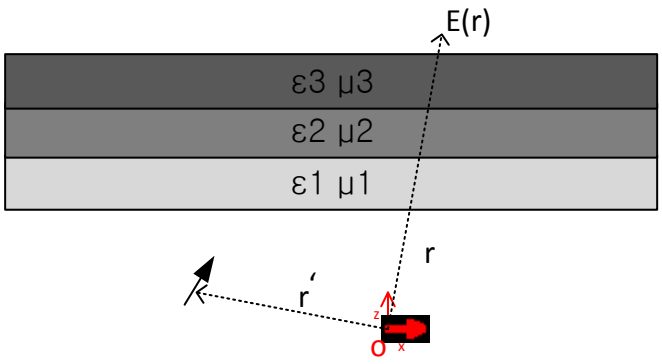

Fig. 4.1. Absorber Stack-up

In (92) A is the equivalent initial voltage of the Nth layer of the stack. This value is 1 for the first layer (ϵ_0, μ_0) where the dipole is located. Since transverse E and H are continuous along the interfaces, a coefficient can be calculated recursively using the following equation starting from layer 1.

$$TL^{N}_{te\backslash tm}(z_{end\ of\ Layer\ N}) = TL^{N+1}_{te\backslash tm}(z_{start\ of\ layer\ N+1}) \tag{92}$$

The last element to calculate is the total reflection coefficient between two consecutive layers. For the simple two-layer case, the transmission and reflection coefficients can be calculated as follows [72]:

$$R^{TE} = \frac{\mu_2 k_{1z} - \mu_1 k_{2z}}{\mu_2 k_{1z} + \mu_1 k_{2z}} \tag{93}$$

$$T^{TE} = \frac{2\mu_2 k_{1z}}{\mu_2 k_{1z} + \mu_1 k_{2z}} \tag{94}$$

$$R^{TM} = \frac{\epsilon_1 k_{1z} - \epsilon_2 k_{2z}}{\epsilon_1 k_{1z} + \epsilon_2 k_{2z}} \tag{95}$$

$$T^{TM} = \frac{2\epsilon_2 k_{1z}}{\epsilon_1 k_{1z} + \epsilon_2 k_{2z}} \tag{96}$$

For a multi-layer media, total reflection coefficient can be calculated in a recursive manner using the following equation [72] starting from the last layer:

$$\tilde{R}_{12} = R_{12} + \frac{T_{12}R_{23}T_{21}e^{2jk_{2z}L_2}}{1-R_{21}R_{23}e^{2jk_{2z}L_2}} \tag{97}$$

where 1, 2, 3 refer to three consecutive layers and L_2 refers to the length of the second layer.

Notice that for a fixed $z - z'$ the integrals in (83-86) and eventually in (87-88) only depend on ρ. Also, since the integral part is identical for x and y directed dipoles, it can be concluded that for the calculation of the final 8 dyads in (89-90), only 4 Sommerfeld integrals must be calculated.

4.3. Source reconstruction model in free-space

4.3.1. Problem Statement

As depicted in Fig. 4.2,it is assumed magnetic fields radiated by a DUT is measured on a planar surface. The goal of the first step of the algorithm is to reconstruct sources on a planar surface of both electric (J) and magnetic (M) currents. The fictitious surface should be planarly discretized using triangular RWG basis functions. The area of the surface should be large enough that it can radiate the same currents as the ones measured on the observation plane. The choice of flat surface is made because it allows for fast interpolation of dyadic Green function to predict fields transmitted by absorbers. Also, since the surface is flat, it is essential to have both electric and magnetic sources on them for the sake of completeness.

4.3.2. Theory

One can use proper integral equations to relate the sources on the fictitious surface to the measured fields on the measurement plane. Since there are both J and M present on the surface, the following equations can be used to relate fields and the currents [10], [25], [26], [38]:

$$\boldsymbol{E}(\boldsymbol{r}) = -\eta_0 \mathbf{L}(\boldsymbol{J};\boldsymbol{r}) + \mathbf{K}(\boldsymbol{M};\boldsymbol{r}) \tag{98}$$

$$\boldsymbol{H}(\boldsymbol{r}) = -\frac{1}{\eta_0}\mathbf{L}(\boldsymbol{M};\boldsymbol{r}) - \mathbf{K}(\boldsymbol{J};\boldsymbol{r}) \tag{99}$$

where

$$\mathbf{L}(\boldsymbol{J};\boldsymbol{r}) = jk_0 \int_{r'} [\boldsymbol{J}(\boldsymbol{r}') + \frac{1}{k_0^2}\nabla\nabla'_s.\boldsymbol{J}(\boldsymbol{r}')]g(\boldsymbol{r},\boldsymbol{r}')ds' \tag{100}$$

$$\mathbf{K}(\boldsymbol{M};\boldsymbol{r}) = \int_{r'} \boldsymbol{M}(\boldsymbol{r}') \times \nabla g(\boldsymbol{r},\boldsymbol{r}')ds' \tag{101}$$

$$g(r,r') = \frac{e^{-jk_0|\boldsymbol{r}-\boldsymbol{r}'|}}{4\pi|\boldsymbol{r}-\boldsymbol{r}'|} \tag{102}$$

where $\eta_0 = \sqrt{\frac{\mu_0}{\epsilon_0}}$, $k_0 = \sqrt{\mu_0 \times \epsilon_0}$ and ∇'_s is the surface divergence factor.

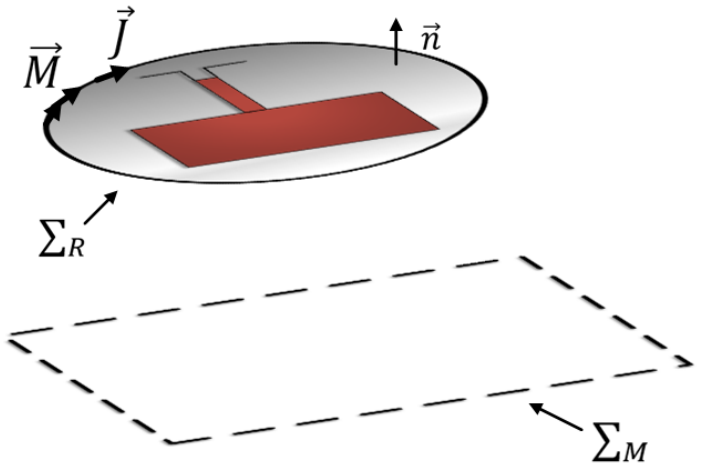

Fig. 4.2. Source Reconstruction Setup

Using (80-82), one can form the main system of integral equations of the problem. This equation states that the fields radiated by both electrical and magnetic currents should rebuild the measured fields.

$$\boldsymbol{n} \times \left(-\frac{1}{\eta_0} \mathbf{L}(\boldsymbol{M}; \boldsymbol{r}_{\boldsymbol{\Sigma m}}) - \mathbf{K}(\boldsymbol{J}; \boldsymbol{r}_{\boldsymbol{\Sigma m}}) \right) = \boldsymbol{n} \times \boldsymbol{H}_{\boldsymbol{measured}} \tag{103}$$

where Σ_m indicates the measurement surface and $H_{measured}$ is the measured field, excluding the normal component.

In this work RWG basis functions [39] are chosen to discretize both the electric and magnetic currents on the basis functions. The choice of RWG basis function guarantees current normal continuity across the edges, which means there will not be any line charges to be dealt with. The current discretization is as follows (the geometric details can be found in Fig. 4.3.):

$$\boldsymbol{J}_{\Sigma R}(\boldsymbol{r}') = \sum_{tri(i)\in\Sigma R} C_i \boldsymbol{f}_i(\boldsymbol{r}') \tag{104}$$

$$\boldsymbol{M}_{\Sigma R}(\boldsymbol{r}') = \eta_0 \sum_{tri(i)\in\Sigma R} C_i \boldsymbol{f}_i(\boldsymbol{r}') \tag{105}$$

where $\boldsymbol{f}_i(r') = \begin{Bmatrix} \frac{l_n}{A_n^+}(\boldsymbol{r}' - \boldsymbol{r_0}), r' \; in \; T_n^+ \\ -\frac{l_n}{A_n^-}(\boldsymbol{r}' - \boldsymbol{r_0}), r' \; in \; T_n^- \\ 0 \; otherwise \end{Bmatrix}$

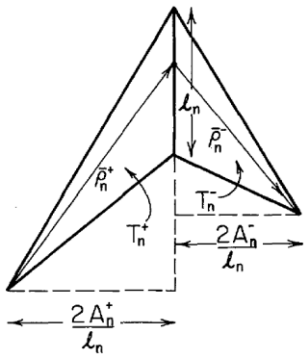

Fig. 4.3. RWG Basis function definition [39]

As it can be seen in (105), magnetic currents are assumed to be η_0 multiplied by RWG basis functions. This choice causes elements of the interaction matrix have similar magnitudes it also increases the conditionality of the final matrix.

In this work adaptive 3/6 points adaptive quadrature has been used to calculate the integrations [25]. In this method, first the integral is estimated using the nodes on the center of the edges. The same integral is then estimated by using all available six points. The estimated integrals can be calculated as follows [25]:

$$I_0 = \frac{A}{3}[f(\boldsymbol{r}_{p1}) + f(\boldsymbol{r}_{p2}) + f(\boldsymbol{r}_{p3})] \tag{106}$$

$$I_1 = \frac{I_0}{3} + \frac{2\times A}{9}[f(\boldsymbol{r}_{p4}) + f(\boldsymbol{r}_{p5}) + f(\boldsymbol{r}_{p6})] \tag{107}$$

where f represents the integrant function and A is the area of the triangle.

If the error between the two estimations is below the error threshold, I_1 is reported as the result of the integration. If not, the triangle breaks into 3 smaller triangles according to Fig. 4.4 and each triangle is now treated like the original triangle. This process repeats recursively until the convergence criteria is met. Note that in the way the triangles split, the calculated nodes are reused in the next round. This scheme increases the efficiency of the algorithm significantly. If the measurement surface is very close to the DUT, due to the singular nature of the integrands, the integrals may not converge as fast. In this particular case singularity extraction methods can be used [25], [26], [42], [44].

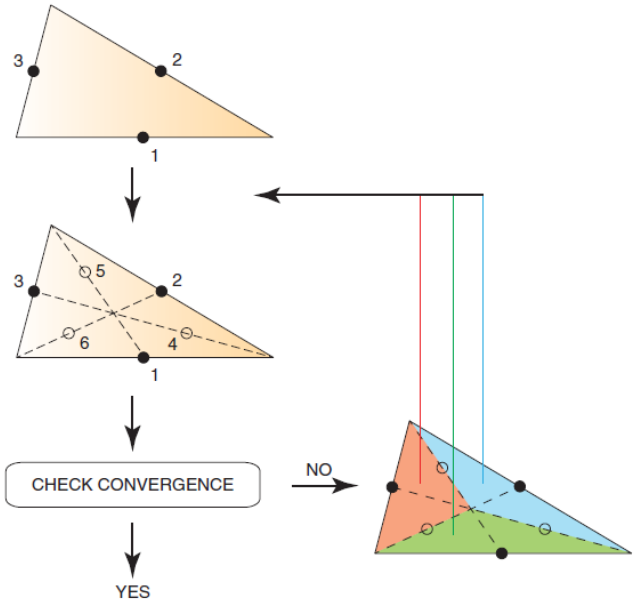

Fig. 4.4. 3/6 Adaptive Quadrature Method [25]

In this method the main kernel decomposes in two parts.

$$g(r,r') = \frac{1}{4\pi|\boldsymbol{r}-\boldsymbol{r'}|} + \left(\frac{e^{-jk_0|r-r'|}}{4\pi|\boldsymbol{r}-\boldsymbol{r'}|} - \frac{1}{4\pi|\boldsymbol{r}-\boldsymbol{r'}|}\right) \tag{108}$$

The first part is the singular part and can be integrated analytically. The second part is the non-singular part and can be calculated using the adaptive quadrature method.

After the matrix is built, the total algebraic system of equations will be as follows:

$$\left[\boldsymbol{Z_J^{freespace}} \quad \boldsymbol{Z_M^{freespace}}\right] \times \begin{bmatrix} C_J \\ C_M \end{bmatrix} = [H_{measured}] \tag{109}$$

Z_J and Z_m matrices represent the interaction of electric current and magnetic current with the measured fields. $C_J$and C_M also represent the coefficient of the RWG basis functions for electric and magnetic currents respectively. After solving (74) by using proper regularization techniques [27] the unknown coefficients ($C_J$and C_M) can be calculated.

4.4. Field Estimation Model in layered media

In section 4.3 it was shown how fields radiated by a DUT can be back-projected into a flat fictitious surface consisting of J and M currents discretized by triangular RWG basis functions. To estimate the reflected and transmitted fields, it is sufficient to replace free-space Green function in (102-103) with the dyadic Green function calculated in Section 4.2. A new interaction matrix is now built using the multi-layer Green function which estimates effects of the absorber. Given the area of interest for estimation of fields, the new matrix elements can be calculated as:

$$Z_{mn}^{Layered} = \int \quad \bar{\bar{G}}^J(\boldsymbol{r}_m, r').J_{RWG}^n(r')dr' \tag{110}$$

Where Z_{mn}shows the element of the interaction matrix representing radiations of the currents on the nth RWG basis function to the mth observation point. The area of integration is on the domain of the nth RWG basis function.

The interaction matrix for magnetic currents follows the same formula as in (103) except using $\bar{\bar{G}}^M$ as the kernel. As for the case in free-space Green function, 3/6-point adaptive quadrature can be used to calculate the matrix elements. So, the final equation can be set as follows:

$$\left[\boldsymbol{Z}_{\boldsymbol{J}}^{layered} \quad \boldsymbol{Z}_{M}^{layered}\right] \times \begin{bmatrix} C_J \\ C_M \end{bmatrix} = [E/H_{estimated}] \tag{111}$$

The RGW coefficients ($C_J \; and \; C_M$) are calculated from the previous step which allows for estimation of fields in forward problem. There is one problem in (111), in that it is time consuming. As for calculation of each element of the interaction matrix, at least 6×2 Sommerfeld integrals must be calculated. That makes the matrix building step take a very long time. As it was mentioned in Section 4.2, if the source and observation points remain in two constant z surfaces, the Sommerfeld integrals only depend on ρ . This condition is met due to the choice of discretization. Thus, before using the adaptive quadrature techniques for calculating matrix element, the range of ρ is detected looking into mesh and observation points. Then all four Sommerfeld integrals required for calculation of Green functions are evaluated within the range in a chosen basis point. Later in the matrix building step, values in other points can be calculated using the pre-calculated ones. Using this method significantly accelerates the matrix building stage.

4.5. Results

4.5.1. Dyadic Green function verification

In this part accuracy of dyadic Green functions method in absorbers application is verified through accurate full-wave simulations. To verify the method, small x-directed electric and magnetic dipoles (small loop) are modeled and simulated using finite element method by HFSS commercial solver. Fig. 4.5(a, b) depicts the details of the model for electric and magnetic dipoles. They both consist of very thin wire stripes excited by current sources. For the electric dipole, the width and the length of the stripe are $\frac{\lambda}{2500}$ and $\frac{\lambda}{40}$ respectively, and it is excited by a 1A current

source placed in the middle of the wire. The magnetic dipole consists of 4 stripes which form a loop in ZY plane. The length and the width of the stripes are $\frac{\lambda}{8000}$ and $\frac{\lambda}{80}$ respectively. To excite the magnetic loop 4 1A current sources are used, one at each center of the edge. This choice of excitation is essential to guarantee current symmetry and uniformity along the loop.

The frequency of simulation is 5GHz and the type of absorber selected for testing is 3-layer carbon foam ECCOSORB AN-77 [71]. Fig. 4.6. shows real and imaginary parts of the individual layers of the absorber. As it can be seen, for matching purposes, the loss increases along the absorber from the front layer towards the back layer. This gradient scheme can be tailored to provide low reflection and high loss at the same time over a wide bandwidth. The total simulation setup is depicted in Fig. 4.5(c) where the x-directed J/M dipole is located at origin 25mm ($0.41\ \lambda$) below the first layer of the absorber stack. Absorber dimensions are $34cm \times 34cm$ ($5.6\ \lambda \times 5.6\ \lambda$) wide and is of $3 \times 19mm$ ($3 \times 0.31\ \lambda$) of height. To verify the accuracy of dyadic Green function, transverse components of magnetic fields are calculated along

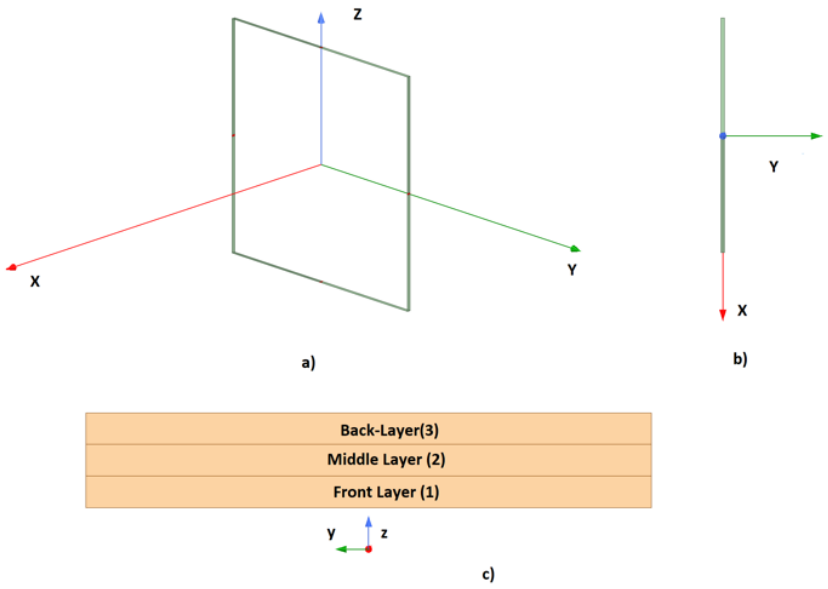

Fig. 4.5. Simulation model for a) magnetic dipole, b) electric dipole and absorber stack

the z-axis through all layers of absorber (at y=5mm, x=0). Before performing the absorber test, to validate the full-wave model as well as the Green function, in the first step it is assumed all three layers are composed of air ($\epsilon_r = 1$). As a result, in this case results can be compared to analytical solutions calculated from (100-101). In the next step, material properties of the 3 layers will be changed to those of AN-77. Fig. 4.7 shows the results of the simulations 1) J/M dipoles in free-space, 2) J/M dipoles in front of a stack of absorbers. The monitor line used for verification is $1mm < z < 112.5mm, x = 0, y = 5mm$, which passed through all layers of absorber. Since H_y for magnetic dipole and H_x for electrical dipoles are identical to 0 on the simulation line, they are omitted from plotting. It should be pointed out that for calculation of Somerfield integrals in the (83-86) "adaptive Gauss-Kronrod pair (15th and 7th order formulas)" quadrature method has been used [73]. Using this all integrals converged with the relative error tolerance of 1e-6. Also,

for the sake of convergence, only in the calculation of dyadic Green function, a virtual tangent loss of 1e-5 has been added to free-space permittivity ($\epsilon_{air} = (1 - j10^{-5})\epsilon_0$).

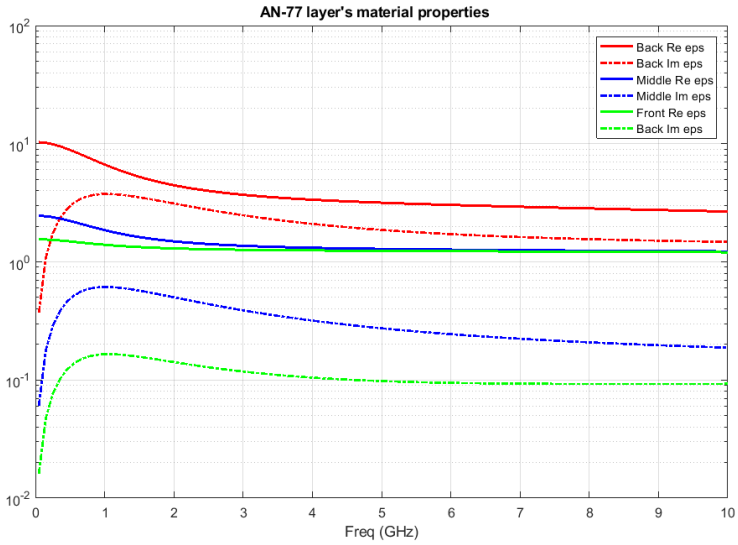

Fig. 4.6. real and imaginary parts of permittivity of AN-77's layers

Looking at Fig. 4.7 shows in free space case, fields calculated by dyadic Green function and that of the FEM are in a very good agreement. This shows the finite element models is a good representative of infinitesimal dipole sources. It is also a simple sanity test for the dyadic Green function method. Also, when the absorber is present, again the FEM method and analytical dyadic Green function method are in a very good agreement, which shows the accuracy of the method. Furthermore, Fig. 4.7 shows fields in the first region have not changed, which is an indication for low reflectivity of the absorber. It can also be seen that most of the amplitude drop is happening

in layer 3 by changing the thickness of which one can tune attenuation of the absorber. To quantitatively show total accuracy of the method, the following sense of error has been plotted in Fig. 4.7(c).

$$error = \frac{\left\| \boldsymbol{H}_t^{analytical} - \boldsymbol{H}_t^{FEM} \right\|}{\left\| \boldsymbol{H}_t^{FEM} \right\|} \tag{112}$$

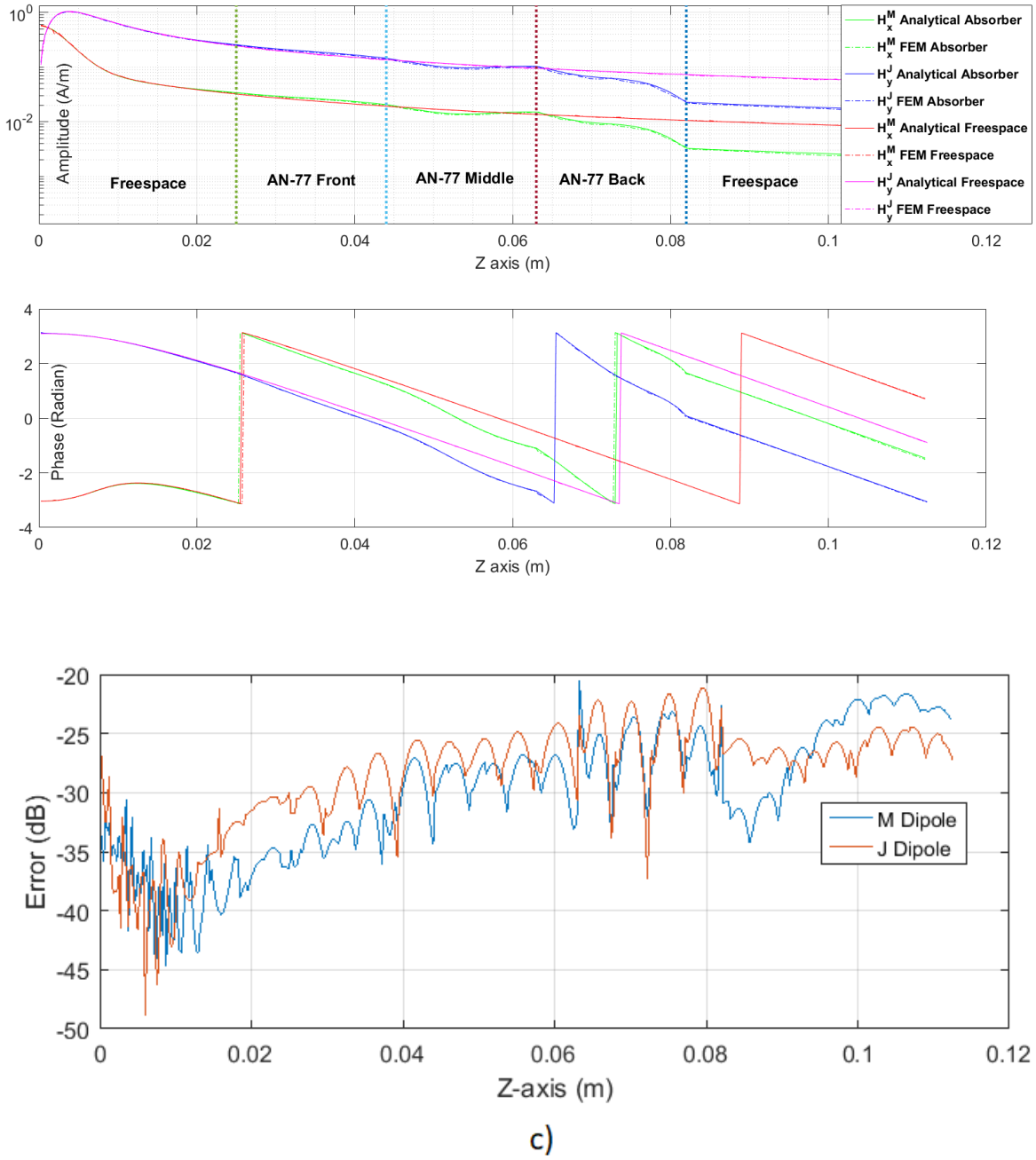

Fig. 4.7. Major Transverse magnetic field components in absorber along z-axis at x=0 and y=5mm. a) amplitude, b) phase, c) Total Fields Error

To study the effect of finiteness of the stack, it is useful to compare fields in the middle of the back layer of the absorber. Fig. 4.8(a, c) depicts fields calculated dyadic Green function whereas Fig. 4.8 depicts the full-wave simulated ones. By comparing these figures or looking at the error ones in Fig. 4.8 (e, f), it can be seen that the edge effects are present only in a small region around the absorber. According to Fig. 4.8 in areas $\frac{\lambda}{4}$, $\frac{\lambda}{2.5}$ and $\frac{\lambda}{1.7}$ away from the edges of the absorber, the edge distortion are less than 10, 15 and 20 dB respectively for both electric and magnetic dipoles.

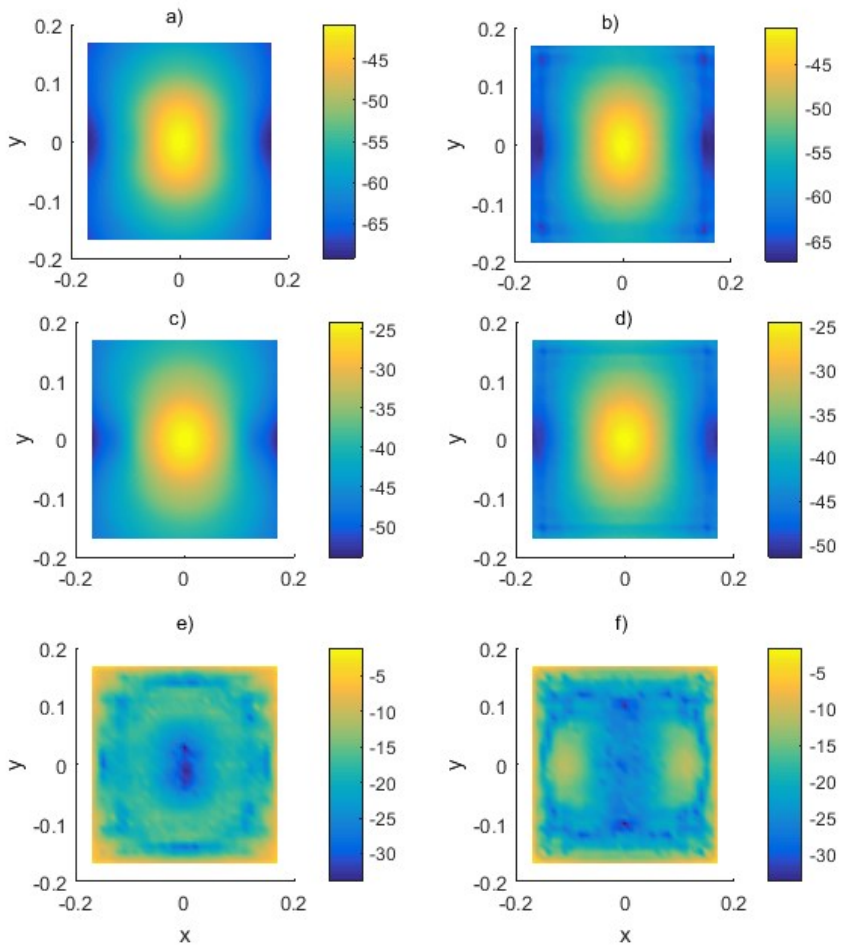

Fig. 4.8. Transverse magnetic field amplitude (dBA/m) in the middle of the last layer of absorber for a) Magnetic dipole analytical (dBA/m), b) Magnetic dipole FEM (dBA/m), c) Electric dipole analytical (dBA/m) d) Electric dipole FEM (dBA/m), e) Magnetic dipole error (dB), f) Electric dipole error(dB).

4.5.2. Radiating PCB track:

In this section, effects of AN-77 absorber is estimated when it is put in front of a radiating PCB track. Fig. 4.9 depicts the selected setup. The substrate for the PCB track is FR4 ($\epsilon_r =$

$4.4(1 - 1j\ 0.02)$) whose size is 2.9, 3.8, 0.157 cm. The PCB track size is 192×0.5 mm and is excited in the middle by a lumped port.

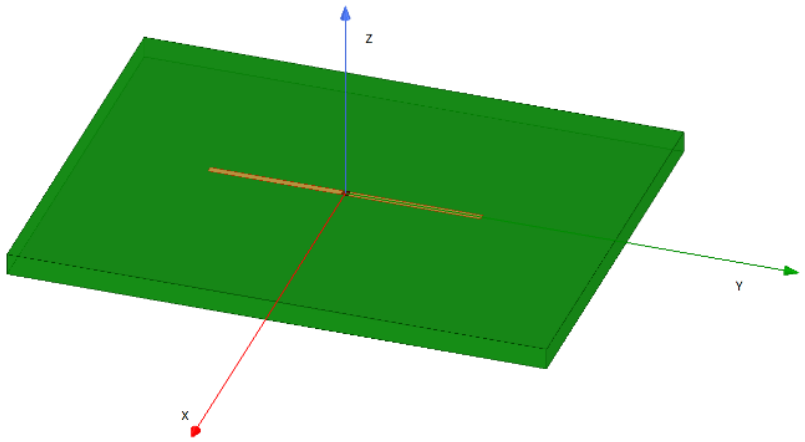

Fig. 4.9. Radiating PCB track setup

In the first step, the structure in Fig. 4.9 is simulated by FEM method using HFSS commercial full-wave solver. Then the magnetic near-fields of the structure is exported out of the solver to be used as the measured data for the algorithm. The measured near-field aperture is $30cm \times 30cm$ at z=5cm and the separation is 1cm. The second step is to back-project the measured fields to a fictitious surface of J&M currents. The surface is chosen to be $12cm \times 12cm$ at Z=5mm discretized by triangular meshes whose average edge length is 0.6cm.

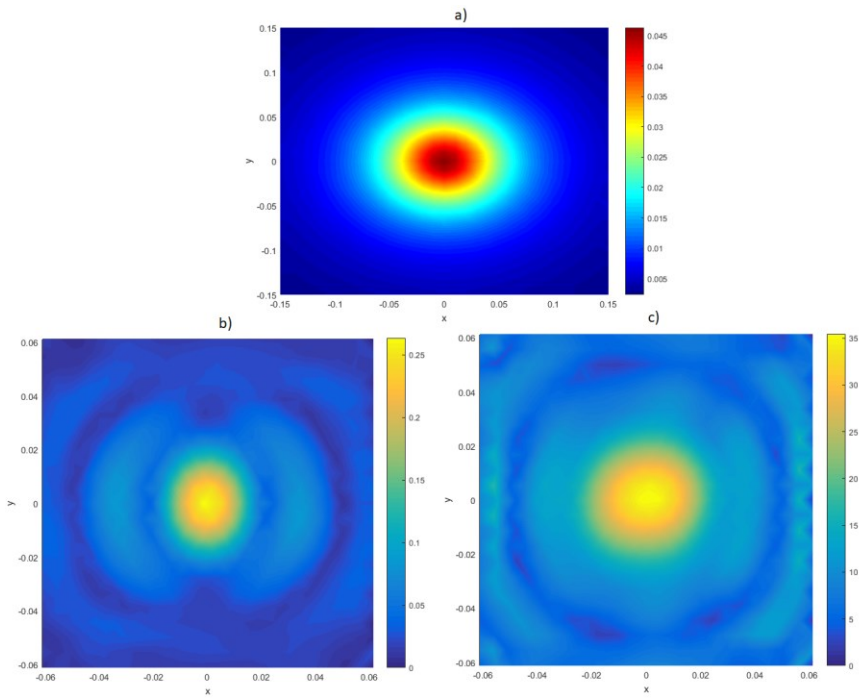

Fig. 4.10. a) Transverse measured magnetic field amplitude (A/m) at z=5cm, b) reconstructed J amplitude (A/m), reconstructed M amplitude (V/m)

Fig. 4.10. (a) shows the near-field exported from the full-wave simulation model at z=5cm which is used as the measured fields. Fig. 4.10. (b,c) show the reconstructed sources on the z=5mm fictitious surface which shows the track is radiating dipole like fields. To do a quick check on the validity of the back-projection, a test is performed. Using the reconstructed J&M, near-fields of the DUT can be calculated using (103) and compared to those of the full-wave simulated ones. Fig. 4.11 shows the comparison between field reconstructions along z-axis (y=5mm, x=0) using the knowledge of transverse magnetic fields on the monitor plane. As it can be seen, fields have been accurately reconstructed up to 2cm above the DUT which shows the SRM is working as desired.

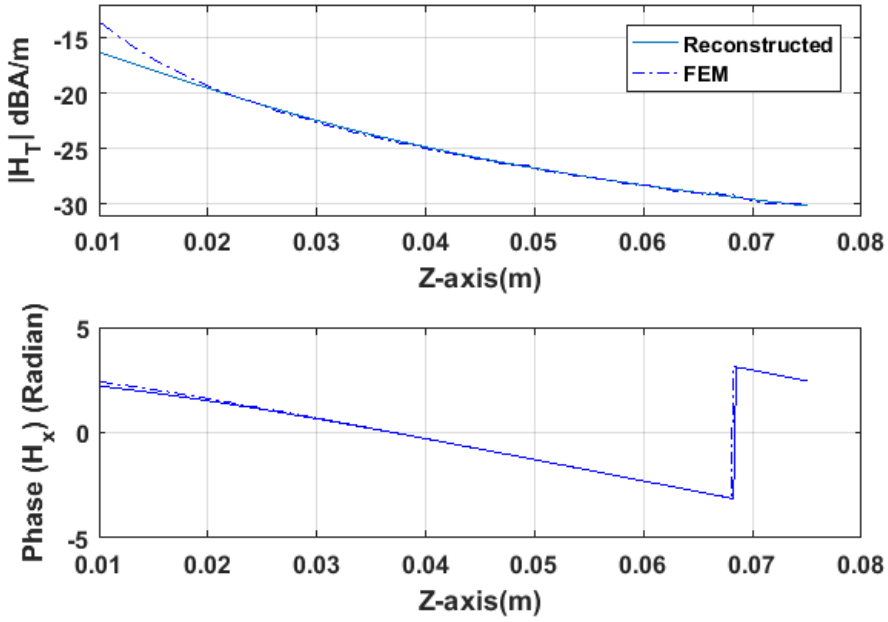

Fig. 4.11. Reconstructed and full-wave simulated fields on z-axis, y=5mm, x=0

In the next step, the setup is changed by placing 3-layer AN-77 ($30cm \times 27cm \times (3 \times 19mm)$) in front of the PCB starting at z=2.5cm., The goal is to estimate fields passed through the absorber. To achieve this, as described in Section IV, the same current distribution from previous step is kept but the kernel changes to planar dyadic Green function. Since evaluating dyadic Green function matrix is time consuming, the main 4 integrals described in Section II can be recalculated using $\rho = \frac{\lambda}{100}$ steps.

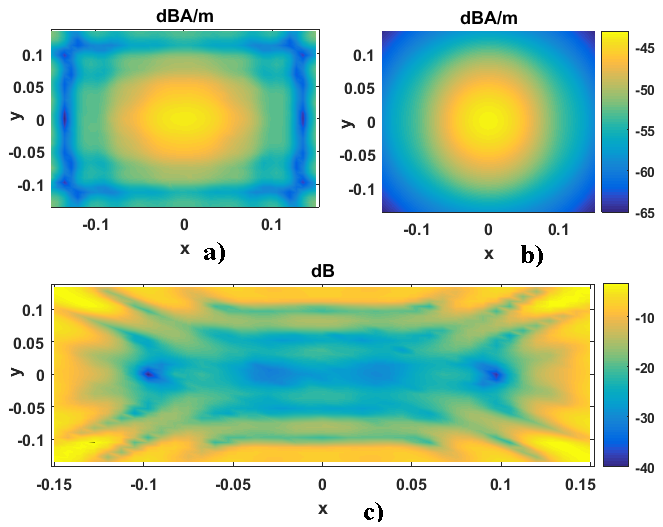

Fig. 4.12. Transverse magnetic field amplitude at z=10.5cm above the absorber stack, a) full-wave (FEM), b) Estimated, c) error

Fig. 4.12(a, b) shows the result of the field estimation. As it is clear in Fig. 4.12(c), the high power area in the middle of the absorber are estimated with less than 20 dB of error. The estimation's accuracy drops close to the edges where the edge effects take over. It is also useful to have a one-dimensional comparison of the field accuracy. For this, estimated fields are compared with the full-wave simulated ones on a line in parallel to the PCB track at z=10.5cm which is 2.3 cm above the absorber. Fig. 4.13 shows magnetic field distribution along Y axis at z=10.5cm, x=0. As it can be seen in Fig. 4.13(a, b) both amplitude and phase of the fields have been estimated with a very good accuracy. Fig. 4.13(c) shows the total error in fields' estimation is better than 20 dB 3cm away from the edges.

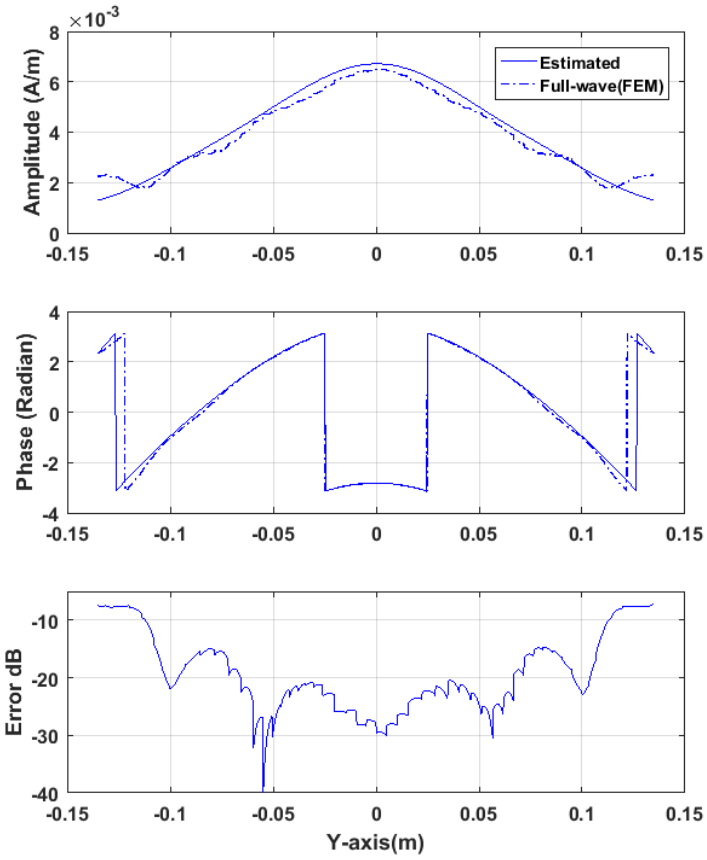

Fig. 4.13. Field distribution above the absorber parallel to the PCB track. A) Amplitude, b) phase, c) error

4.6. Conclusion

In this work it was first shown that dyadic Green's functions are powerful tools for analysing planarly stratified absorbers. It was also shown that the finiteness of the absorbers does not introduce significant error (<10dB) at least $\frac{\lambda}{2}$ away from the edge of the absorbers.

A novel algorithm was also proposed to estimate absorber effects on a DUT only using the knowledge of transverse near-fields of the DUT measured on free-space. It was first shown that accurate field reconstruction can be done using the knowledge of the transverse magnetic fields

radiated by the DUT. It was also shown that accurate estimation of fields can be made by replacing free-space Green's function with dyadic Green's function of the absorber stack.

Chapter 5

Conclusion and future directions

Conclusion

In this thesis 3 major issues about EMSCAN scanners were addressed.

1) Ground de-embedding algorithm, introduced in Chapter 2, is a novel algorithm which improves accuracy of near-field to far-field transformation performed with RFX scanners. In this algorithm the scanned near-fields was back-projected onto 2 separate fictitious surfaces. This technique was shown to be useful in differentiating radiation contributions of DUT and the ground plane. In addition, 4 SRM models were introduced for de-embedding. Simulation and measured results showed that for the near-field to far-field transformation, the first scenario (only electric currents on the fictitious layer) is the best method. The results of the monopole and slot antennas showed that the far-field accuracy, defined by an angular threshold in degrees of $E\theta$ and $E\phi$, has significantly increased from 7° and 18° to 40° and 54° in the first example and from 17° and 27° to 40° and 83° in the second one, respectively. However, it was shown that for diagnosis purposes, the JMB method, which provides both J and M information, is a better option.

2) A 6-sided algorithm introduced in Chapter 3, a novel algorithm which enables users to combine 6 individual scans on a cube to achieve full sphere radiation pattern. The algorithm can

fix the dominant source of error introduced in this type of measurement. Also, a comprehensive study on SRM was done subject to the magnetic measurements on redundant cube. The results demonstrated that all methods are consistently accurate in terms of near-field to far-field transformation. However, JMB is the superior magnetic field reconstruction method for the near-field reconstructions.

3) The absorber effects prediction algorithm introduced in Chapter 5, a novel algorithm for EMC/EMI applications. In this part, it is first shown that Green's functions for layered media are very effective and powerful tools for planar multi-layered absorber analysis. Moreover, a novel algorithm was proposed to estimate effects introduced by these types of absorbers. In this method the radiated near-fields of the DUT were measured in free-space and back-projected to an equivalent source. Next, dyadic Green's functions are used for estimating effects of the absorber on radiations of the DUT.

Future Directions:

As a future work for chapter 2, it is suggested to work on ground de-embedding in 6-sided algorithm. In the proposed work, one must try to suggest a technique which can address multiple measurements for ground de-embedding. The challenge for this work is that the loading of the ground plane is different depending on the orientation of the ground plane on DUT in each measurement. To achieve this goal, the basic SRM model needs to be relaxed with more degrees of freedom. The additional parameters allow for modeling the different loading effects on each side. The choice of the parameters will be very tricky. The reason is if the parameters are too flexible, the problem eventually breaks into 6 individual ones which would require stitching of the final solutions. At the same time, if the parameters are not flexible enough, the whole system of equations will be impossible to solve and leads to contradiction. One choice of parameters for this purpose could be a limited number of far-field spherical modes.

As a future work for chapter 3, it is suggested to try to model other sources of error in 6-sided algorithm translational misalignment and try to solve for those types of error. To achieve this goal, it is essential to model impacts of such errors on the MOM matrix and its right-hand side. As such model for the translational and rotational errors will be non-linear, the problem can be changed to how the matrix and the right-hand side will change with very small variation of the error parameters. If this small variation can be calculated as a function of basic error sources (translation, rotation, …), the perturbation theory can be used in an iterative scheme to find the

optimum results. In the iterative scheme, the algorithm tries to find a small vector of variation so that the total norm of the solution goes minimum. After a number of iterations, the system stabilizes and corrected.

As a future work for chapter 4, it is suggested to try to extend the proposed method to finite size absorbers. To achieve this goal, one needs to either try to calculate the dyadic Green's function for a finite size slab or alternatively try to post correct for absorber finiteness. The first approach is a very advanced one and requires in dept knowledge of Green's function which is out of the scope of this thsis. For the second approach, the patch antenna's cavity model can be used to approximate edge effects. In this approach, M and J currents on the edge of the slab are estimated and these models are further used for field correction inside the slab of the absorber,

Bibliography

[1] "EM-SCAN RFX2 Datasheet." [Online]. Available: https://www.gnss.co.jp/wp-content/uploads/2017/07/RFX2_Datasheet_v9.pdf.

[2] S. Ponnapalli, T. K. Sarkar, and P. Petre, "Near-field to far-field transformation using an equivalent current approach," in *Antennas and Propagation Society Symposium 1991 Digest*, IEEE, 1991, pp. 1458–1461.

[3] J. J. H. Wang, "An examination of the theory and practices of planar near-field measurement," *IEEE Trans. Antennas Propag.*, vol. 36, no. 6, pp. 746–753, Jun. 1988.

[4] D. B. M. K. Z. R. C. A. Y. Vives-Gilabert and A. L. B. Mazari, "Plane wave spectrum theory applied to nearfield measurements for electromagnetic compatibility investigations," *Sci. Meas. Technol. IET*, vol. 1, no. 4, pp. 216–223, 2007.

[5] E. B. Joy and D. T. Paris, "Spatial Sampling and Filtering in Near-Field Measurements," *IEEE Trans. Antennas Propag.*, vol. 20, no. 3, pp. 253–261, 1972.

[6] P. Petre and T. K. Sarkar, "Differences between modal expansion and intergral equation methods for planar near-field to far-field transformation," *Prog. Electromagn. Res.*, vol. 12, pp. 37–56, 1996.

[7] P. Petre and T. K. Sarkar, "A planar near-field to far-field transformation using an equivalent magnetic current approach," *Antennas Propag. Soc. Int. Symp. 1992. AP-S. 1992 Dig. Held Conjuction with URSI Radio Sci. Meet. Nucl. EMP Meet. IEEE*, vol. 40, no. 11, pp. 1534–1537, 1992.

[8] Y. A. Lopéz, F. L. H. Andrés, M. R. Pino, and T. K. Sarkar, "An improved super-resolution source reconstruction method," *IEEE Trans. Instrum. Meas.*, vol. 58, no. 11, pp. 3855–3866, Nov. 2009.

[9] J. L. A. Quijano and G. Vecchi, "Improved-accuracy source reconstruction on arbitrary 3-D surfaces," *IEEE Antennas Wirel. Propag. Lett.*, vol. 8, pp. 1046–1049, 2009.

[10] J. L. Araque Quijano and G. Vecchi, "Near- and very near-field accuracy in 3-D source reconstruction," *IEEE Antennas Wirel. Propag. Lett.*, vol. 9, pp. 634–637, 2010.

[11] J. R. Regué, M. Ribó, J. M. Garrell, and A. Martín, "A genetic algorithm based method for source identification and far-field radiated emissions prediction from near-field measurements for PCB characterization," *IEEE Trans. Electromagn. Compat.*, vol. 43, no. 4, pp. 520–530, 2001.

[12] F. Las-Heras and T. K. Sarkar, "A direct optimization approach for source reconstruction and NF-FF transformation using amplitude-only data," *IEEE Trans. Antennas Propag.*, vol. 50, no. 4, pp. 500–510, 2002.

[13] J. J. Laurin, J. F. Zürcher, and F. E. Gardiol, "Near-field diagnostics of small printed antennas using the equivalent magnetic current approach," *IEEE Trans. Antennas Propag.*,

vol. 49, no. 5, pp. 814–828, May 2001.

[14] P. A. Barrière, J. J. Laurin, and Y. Goussard, “Mapping of equivalent currents on high-speed digital printed circuit boards based on near-field measurements,” *IEEE Trans. Electromagn. Compat.*, vol. 51, no. 3 PART 2, pp. 649–658, Aug. 2009.

[15] J. Colinas, Y. Goussard, and J. J. Laurin, “Application of the Tikhonov regularization technique to the equivalent magnetic currents near-field technique,” *IEEE Trans. Antennas Propag.*, vol. 52, no. 11, pp. 3122–3132, Nov. 2004.

[16] B. Omrane, J. J. Laurin, and Y. Goussard, “Subwavelength-resolution microwave tomography using wire grid models and enhanced regularization techniques,” *IEEE Trans. Microw. Theory Tech.*, vol. 54, no. 4, pp. 1438–1450, Jun. 2006.

[17] B. Omrane, Y. Goussard, and J.-J. Laurin, “Constrained Inverse Near-Field Scattering Using High Resolution Wire Grid Models,” *IEEE Trans. Antennas Propag.*, vol. 59, no. 10, pp. 3710–3718, Oct. 2011.

[18] Y. Alvarez, F. Las-Heras, and M. R. Pino, “Probe distortion correction in near field - Far field transformations based on equivalent sources characterization,” *Eur. Sp. Agency, (Special Publ. ESA SP*, vol. 626 SP, no. October, pp. 2–6, 2006.

[19] K. Sarabandi, J. Choi, A. Sabet, and K. Sabet, “Pattern and Gain Characterization Using Nonintrusive Very-Near-Field Electro-Optical Measurements over Arbitrary Closed Surfaces,” *IEEE Trans. Antennas Propag.*, vol. 65, no. 2, pp. 489–497, Feb. 2017.

[20] J. C. Bolomey, H. Memarzadeh-Tehran, and J. J. Laurin, “Optimization of optically and

electrically modulated scattering probes for field measurements," *IEEE Trans. Instrum. Meas.*, vol. 63, no. 1, pp. 154–165, Jan. 2014.

[21] H. Memarzadeh-Tehran, A. Diaz-Bolado, J. J. Laurin, and R. Kashyap, "Bandwidth improvement in a resonant optical MST-probe applicable to near-field imaging," *IEEE Antennas Wirel. Propag. Lett.*, vol. 10, pp. 411–414, 2011.

[22] H. Memarzadeh-Tehran, J. J. Laurin, and R. Kashyap, "Optically modulated probe for precision near-field measurements," *IEEE Trans. Instrum. Meas.*, vol. 59, no. 10, pp. 2755–2762, Oct. 2010.

[23] H. Memarzadeh, M. Lamarche, J. J. Laurin, and R. Kashyap, "A technique to improve the dynamic range and linearity of a near-field imager based on the modulated scatterer approach," *IEEE Antennas Propag. Soc. AP-S Int. Symp.*, no. I, pp. 3–6, 2009.

[24] H. Memarzadeh, J.-J. Laurin, and R. Kashyap, "Microwave Imaging System Incorporating an Array of Optically Modulated Probes for Rapid and Low-Perturbation Near-Field Measurements," *AMTA 32th Annu. Meet. Symp.*, 2010.

[25] Ö. Ergül and L. Güre, *The Multilevel Fast Multipole Algorithm (MLFMA) Computational Problems*. IEEE Press, 2014.

[26] R. Carter, "The Method of Moments in Electromagnetics, by W.C. Gibson," *Contemp. Phys.*, vol. 51, no. 2, pp. 183–184, 2010.

[27] P. C. Hansen, "Regularization Tools Matlab Package for Analysis and Solution of Descrete Ill-Posed Problems," vol. 6, no. March, pp. 1–35, 1998.

[28] K. Payandehjoo and R. Patton, “De-embeding the effect of a printed array of probes on planar very-near-field measurements,” in *2014 IEEE Conference on Antenna Measurements and Applications, CAMA 2014*, 2014, pp. 1–4.

[29] R. R. Alavi, A. Kiaee, R. Mirzavand, and P. Mousavi, “Locally corrected Nyström technique and its relationship with RWG method of moment for current reconstruction using very-near-field measurements,” in *2017 11th European Conference on Antennas and Propagation, EUCAP 2017*, 2017, pp. 319–323.

[30] J. J. H. Wang, “An Examination of the Theory and Practices of Planar Near-field Measurement,” *IEEE Trans. Antennas Propag.*, vol. 36, no. 6, pp. 746–753, Jun. 1988.

[31] R. Mittra and A. Rushdi, “A Numerically Efficient Approach for Computing the Geometrical Optics Field Reflected from a Specified Surface,” *IEEE Antennas and Propagation Society Newsletter*, vol. 21, no. 1. p. 11, 1979.

[32] Y. A. Lopez, F. Las-Heras Andres, M. R. Pino, and T. K. Sarkar, “An Improved Super-Resolution Source Reconstruction Method,” *IEEE Trans. Instrum. Meas.*, vol. 58, no. 11, pp. 3855–3866, Nov. 2009.

[33] Y. Álvarez, F. Las-Heras, and M. R. Pino, “The sources reconstruction method for amplitude-only field measurements,” *IEEE Trans. Antennas Propag.*, vol. 58, no. 8, pp. 2776–2781, Aug. 2010.

[34] C. H. Schmidt and T. F. Eibert, “Multilevel plane wave based near-field far-field transformation for electrically large antennas in free-space or above material halfspace,”

IEEE Trans. Antennas Propag., vol. 57, no. 5, pp. 1382–1390, May 2009.

[35] J. L. Araque Quijano, L. Scialacqua, J. Zackrisson, L. J. Foged, M. Sabbadini, and G. Vecchi, "Suppression of undesired radiated fields based on equivalent currents reconstruction from measured data," *IEEE Antennas Wirel. Propag. Lett.*, vol. 10, pp. 314–317, 2011.

[36] P. Yla-Oijala and M. Taskinen, "Well-conditioned Muller formulation for electromagnetic scattering by dielectric objects," *IEEE Trans. Antennas Propag.*, vol. 53, no. 10, pp. 3316–3323, 2005.

[37] G. C. Hsiao and R. E. Kleinman, "Mathematical foundations for error estimation in numerical solutions of integral equations in electromagnetics," *IEEE Trans. Antennas Propag.*, vol. 45, no. 3, pp. 316–328, 1997.

[38] R. F. Harrington, *Time-Harmonic Electromagnetic Fields*. Wiley-IEEE Press, 2001.

[39] S. M. Rao, D. R. Wilton, and A. W. Glisson, "Electromagnetic Scattering by Surfaces of Arbitrarily Shape," *IEEE Trans. Antennas Propag.*, vol. 30, no. 5, pp. 409–418, 1982.

[40] and• I. K. Leven Gurel, Kubilay Sertet, "On the choice of basis functions to model surface electric current densities in computational electromagnetics," *Radio Sci.*, vol. 34, no. 6, pp. 1373–1387, 1999.

[41] R. E. Hodges and Y. Rahmat-Samii, "The evaluation of MFIE Integrals," *Microw. Opt. Technol. Lett.*, vol. 14, no. 1, pp. 9–14, 1997.

[42] R. D. Graglia, "On the numerical integration of the linear shape functions times the 3-D

Green's function or its gradient on a plane triangle," *IEEE Trans. Antennas Propag.*, vol. 41, no. 10, pp. 1448–1455, 1993.

[43] L. Gurel and O. Ergul, "Singularity of the Magnetic-Field Integral Equation and its Extraction," *Antennas Wirel. Propag. Lett.*, vol. 4, no. 1, pp. 229–232, 2005.

[44] P. Ylä-Oijala and M. Taskinen, "Calculation of CFIE impedance matrix elements with RWG and n × RWG functions," *IEEE Trans. Antennas Propag.*, vol. 51, no. 8, pp. 1837–1846, 2003.

[45] C. Balanis, *Antenna Theory: Analysis and Design*. Wiley-Interscience; 3 edition, 2009.

[46] S. Gregson, J. McCormick, and C. Parini, *Principles of Planar Near-Field Antenna Measurements*, vol. 53. Institution of Engineering and Technology, 2007.

[47] P. C. Clemmow, *The plane wave spectrum representation of electromagnetic fields*. .

[48] A. Yaghjian, "An overview of near-field antenna measurements," *IEEE Trans. Antennas Propag.*, vol. 34, no. 1, pp. 30–45, Jan. 1986.

[49] J. Laviada-Martinez, Y. Alvarez Lopez, and F. Las-Heras, "EFFICIENT DETERMINATION OF THE NEAR-FIELD IN THE VICINITY OF AN ANTENNA FOR THE ESTIMATION OF ITS SAFETY PERIMETER," *Prog. Electromagn. Res.*, vol. 103, pp. 371–391, 2010.

[50] Peter Petre and T. K. Sarkar, "A planar near-field to far-field transformation using an equivalent magnetic current approach," *Antennas Propag. Soc. Int. Symp. 1992. AP-S. 1992 Dig. Held Conjuction with URSI Radio Sci. Meet. Nucl. EMP Meet. IEEE*, vol. 1, pp. 1534–

1537, 2015.

[51] A. Kiaee, R. R. Alavi, R. Mirzavand, and P. Mousavi, "Numerical and Experimental Assessment of Source Reconstruction for Very Near-Field Measurements With an Array of H -Field Probes," *IEEE Trans. Antennas Propag.*, vol. 66, no. 3, pp. 1311–1320, Mar. 2018.

[52] M. Sorensen, O. Franek, G. F. Pedersen, A. Radchenko, K. Kam, and D. Pommerenke, "Estimate on the uncertainty of predicting radiated emission from near-field scan caused by insufficient or inaccurate near-field data: Evaluation of the needed step size, phase accuracy and the need for all surfaces in the Huygens' box," in *International Symposium on Electromagnetic Compatibility - EMC EUROPE*, 2012, pp. 1–6.

[53] X. Hou, C. Parini, and S. Gregson, "Planar near-field measurement on an omni-directional UWB antenna," in *2007 International workshop on Antenna Technology: Small and Smart Antennas Metamaterials and Applications*, 2007, pp. 380–383.

[54] M. Li, M. A. Francavilla, F. Vipiana, G. Vecchi, and R. Chen, "Nested equivalent source approximation for the modeling of multiscale structures," *IEEE Trans. Antennas Propag.*, vol. 62, no. 7, pp. 3664–3678, 2014.

[55] Y. Qi *et al.*, "5G Over-the-Air Measurement Challenges: Overview," *IEEE Trans. Electromagn. Compat.*, vol. 59, no. 6, pp. 1661–1670, Dec. 2017.

[56] Q. Huang *et al.*, "MoM-Based Ground Current Reconstruction in RFI Application," *IEEE Trans. Electromagn. Compat.*, vol. 60, no. 4, pp. 1121–1128, Aug. 2018.

[57] C. Hwang and Q. Huang, "IC placement optimization for RF interference based on dipole

moment sources and reciprocity," in *2017 Asia-Pacific International Symposium on Electromagnetic Compatibility (APEMC)*, 2017, pp. 331–333.

[58] H. Zeng, E. Cao, C. Shu, and B. Luo, "Effectively resolving de-sense issues in practical wireless system design: An EMC engineer's approach," in *2017 IEEE International Symposium on Electromagnetic Compatibility & Signal/Power Integrity (EMCSI)*, 2017, pp. 458–463.

[59] S. Piersanti *et al.*, "Near-Field Shielding Performances of EMI Noise Suppression Absorbers," *IEEE Trans. Electromagn. Compat.*, vol. 59, no. 2, pp. 654–661, Apr. 2017.

[60] S. Piersanti *et al.*, "Near-Field Shielding Performances of Absorbing Materials for Integrated Circuits (IC) Applications. Part II: Crossing Excitation," *IEEE Trans. Electromagn. Compat.*, vol. 60, no. 1, pp. 196–201, Feb. 2018.

[61] H. Wang, V. Khilkevich, Y.-J. Zhang, and J. Fan, "Estimating Radio-Frequency Interference to an Antenna Due to Near-Field Coupling Using Decomposition Method Based on Reciprocity," *IEEE Trans. Electromagn. Compat.*, vol. 55, no. 6, pp. 1125–1131, Dec. 2013.

[62] Z. Yu, J. A. Mix, S. Sajuyigbe, K. P. Slattery, and J. Fan, "An improved dipole-moment model based on near-field scanning for characterizing near-field coupling and far-field radiation from an IC," *IEEE Trans. Electromagn. Compat.*, vol. 55, no. 1, pp. 97–108, 2013.

[63] Y.-H. Bi, Y. Qi, J. Fan, and W. Yu, "A Planar Low-Profile Meander Antenna (PLMA) Design for Wireless Terminal Achieving Between Intrasystem EMC and Isolation in

Multiantenna Systems," *IEEE Trans. Electromagn. Compat.*, vol. 59, no. 3, pp. 980–987, Jun. 2017.

[64] X. Jiao *et al.*, "EMI mitigation with lossy material at 10 GHz," in *2014 IEEE International Symposium on Electromagnetic Compatibility (EMC)*, 2014, pp. 150–154.

[65] F. de Paulis, C. Rizza, A. Ciattoni, E. Palange, and A. Orlandi, "Dynamically reconfigurable metamaterials for shielding and absorption in the GHz range," in *2015 IEEE International Symposium on Electromagnetic Compatibility (EMC)*, 2015, pp. 1047–1052.

[66] F. de Paulis, M. H. Nisanci, A. Orlandi, M. Y. Koledintseva, and J. L. Drewniak, "Design of Homogeneous and Composite Materials From Shielding Effectiveness Specifications," *IEEE Trans. Electromagn. Compat.*, vol. 56, no. 2, pp. 343–351, Apr. 2014.

[67] D. Micheli *et al.*, "Broadband Electromagnetic Absorbers Using Carbon Nanostructure-Based Composites," *IEEE Trans. Microw. Theory Tech.*, vol. 59, no. 10, pp. 2633–2646, Oct. 2011.

[68] C. Olivieri *et al.*, "Analysis of Near-Field Emissions From Common-Mode Filters Based on EBG Structures," *IEEE Trans. Electromagn. Compat.*, vol. 59, no. 2, pp. 593–599, Apr. 2017.

[69] L. Gao, X.-C. Wei, Y.-T. Huang, B. Li, and Y.-F. Shu, "Analysis of Near-Field Shielding Effectiveness for the SiP Module," *IEEE Trans. Electromagn. Compat.*, vol. 60, no. 1, pp. 288–291, Feb. 2018.

[70] S. Piersanti *et al.*, "Electric Dipole Equations in Very-Near-Field Conditions for

Electromagnetic Shielding Assessment—Part II: Wave Impedance, Reflection, and Transmission," *IEEE Trans. Electromagn. Compat.*, vol. 59, no. 4, pp. 1203–1210, Aug. 2017.

[71] Emerson, "ECCOSORB AN parallel and perpendicular polarization data." [Online]. Available: www.eccosorb.com. [Accessed: 27-May-2018].

[72] C. Weng Cho, *Waves and Fields in Inhomogenous Media*. IEEE Press, 1999.

[73] L. F. Shampine, "Vectorized adaptive quadrature in MATLAB," *J. Comput. Appl. Math.*, vol. 211, no. 2, pp. 131–140, Feb. 2008.